DEVELOPMENT OF A NEW SPECTROPHOTOMETRIC METHOD FOR FULL CHARACTERIZATION OF TURBIDITY

by

Stephen Mutisya

July 2022

Director of Dissertation: Dr. Jun Qing Lu

Major Department: Physics

# Abstract

Characterization of turbid materials by determining their inherent optical properties has attracted strong research interest due to wide potential applications in fields such as material analysis and biomedical optics. Based on radiative transfer theory, the response of a homogeneous turbid sample to an optical excitation can be accurately described by three optical parameters: the absorption coefficient $\mu_a$, the scattering coefficient $\mu_s$, and the anisotropy factor g. Existing spectrophotometric methods that are often utilized to measure these parameters typically use integrating spheres to acquire the light signals. The integrating sphere approach, however, is difficult to be translated into instruments for users without special training. The goal of this dissertation research project is two-fold: (1) Develop and validate a new spectrophotometric method without integrating spheres to characterize turbidity of optically thick samples by three optical parameters of $\mu_a(\lambda)$, $\mu_s(\lambda)$ and $g(\lambda)$; (2) demonstrate the applicability of the new spectrophotometric method as a label-free assay of cellular apoptosis in suspension samples treated by a chemotherapy drug. An experimental system has been developed to measure signals of the diffuse reflectance $R_d$, the diffuse transmittance $T_d$ and the forward transmittance $T_f$ as functions of wavelength $\lambda$ between 460 and 1000 nm. The optical parameters of turbid samples are then

inversely determined by an in-house developed individual photon Monte Carlo (iMC) simulation software. Validation of the new method has been achieved by comparing the optical parameters inversely determined from the measured signals to those predicted by the Mie theory for polystyrene microsphere samples. In addition, we have applied the validated method to obtain the radiative transfer parameters of MCF7 cell samples treated by doxorubicin drug to induce apoptosis with three different doses and three post-treatment times. By comparing to apoptosis measurement results of MTT assay and fluorescent flow cytometry, we were able to qualitatively demonstrate the potential applications of the new spectrophotometric method as a label-free assay to detect cellular apoptosis in treated samples.

# DEVELOPMENT OF A NEW SPECTROPHOTOMETRIC METHOD FOR FULL CHARACTERIZATION OF TURBIDITY

A Dissertation

Presented to the Faculty of the Department of Physics

East Carolina University

In Partial Fulfillment of the Requirements for the Degree

Doctor of Philosophy in Biomedical Physics

by

Stephen Mutisya

July 2022

DEVELOPMENT OF A NEW SPECTROPHOTOMETRIC METHOD FOR FULL CHARACTERIZATION OF TURBIDITY

By

Stephen Mutisya

APPROVED BY:

Director of Dissertation _____
Jun Qing Lu, Ph.D

Committee Member _____
Xin-Hua Hu, Ph.D.

Committee Member _____
Nathan Hudson, Ph.D

Committee Member _____
Colin Burns, Ph.D

Committee Member _____
Li Yang, Ph.D

Chair of the Department of Physics _____
Jefferson Shinpaugh, Ph.D.

Interim Dean of the Graduate School _____
Kathleen T Cox, PhD

## DEDICATION

This dissertation is dedicated to;

My father and mother for giving me invaluable educational opportunities

My wife Rachel for inspiration and encouragement throughout the duration of this study

## ACKNOWLEDGEMENTS

First, I would like to express my gratitude to my advisors, Dr. Jun Qing Lu and Dr. Xin-Hua Hu for their invaluable advice, tireless guidance, and patience during this dissertation project. I would like to thank committee members, Dr. Nathan Hudson, Dr. Colin Burns, and Dr. Li Yang for their helpful feedback and for dedicating their time towards my dissertation. I am thankful for the support I received from Dr. Peng Tian and Dr. Jiahong Jin in developing the simulation program used in my research. I would like also to thank Dr. Kenneth Jacobs, Mr. Gene Oakley, and Mr. William Holland for their support and assistance in building the equipment used in this research and to Dr. Douglas Weidner for his help in performing cell sorting assay. I also take this opportunity to thank the ECU physics department for financially supporting me during my study. In addition, I would like to express my gratitude to Dr. Michael Dingfelder for his support, academic guidance and advising during the entire period of my studies at ECU. Finally, I would like to thank my family particularly my wife and children. Without their encouragement and understanding, it would have been impossible for me to complete this dissertation research.

## TABLE OF CONTENTS

## LIST OF TABLES

## LIST OF FIGURES

## LIST OF SYMBOLS OR ABBREVIATIONS

| Symbol/Abbreviation | Name |
|---|---|
| $\lambda$ | wavelength |
| $\mu_a$ | absorption coefficient |
| $\mu_s$ | scattering coefficient |
| $\mu_t$ | attenuation coefficient |
| g | anisotropy factor |
| $p(\theta, \varphi)$ | scattering phase function |
| p (s, s') | scattering phase function |
| $\theta$ | polar angle |
| $\varphi$ | azimuthal angle |
| $R_d$ | diffuse reflectance |
| $T_d$ | diffuse transmittance |
| $T_f$ | forward transmittance |
| $T_c$ | collimated transmittance |
| *d* | sample thickness |
| *ds* | diameter of scattering particle |
| $d_L$ | diameter of BK7 Lens |
| A | absorbance |
| $I_o$ | incidence light intensity |
| $I_c$ | collimated transmitted light intensity |
| RT | radiative transfer theory |
| $n_i$ | imaginary part of a complex refractive index |
| $n_r$ | real part of a complex refractive index |
| $\alpha$ | scattering size parameter |
| $\sigma_s$ | scattering cross-section |
| $\sigma_a$ | absorption cross-section |
| $\sigma_e$ | extinction cross-section |
| $\rho$ | number density |

| | |
|---|---|
| L (**r**, **s**) | radiance |
| D | drug dose |
| $D_i$ (i=1,2,3,4) | photodetectors |
| $D_c$ | cell debris |
| V | viable cells |
| EA | early apoptotic |
| LA | late apoptotic |
| c | calibration factor for sample incidence light |
| LIB | lock-in board |
| LIA | lock-in amplifier |
| G | lock-in board gain |
| S | photodetector sensitivity |
| F | sensitivity-gain factor |
| iMC | individual Monte Carlo |

# CHAPTER 1 Introduction

Many natural and artificial materials are turbid which require quantitative modeling of light scattering for analysis of light-matter interaction and determination of their optical properties. Investigation of light scattering in turbid materials and development of methods to characterize these materials are critically important in basic research, which also have wide applications in material analysis and clinical studies. Most applications depend on the ability to accurately determine optical properties of those materials. For instance, therapeutic applications of light such as photodynamic therapy and laser surgery requires information on absorption of the light while diagnostic applications such as tissue imaging and blood flow measurements depend on the knowledge on scattering properties of different tissues [7]. The absorption of light is related to the chemical composition of the turbid media while the scattering depends on the morphological properties or inhomogeneities of the refractive index in media on the scales close to wavelength such as cellular structures [8]. To characterize the absorption and scattering of light in turbid materials such as cell suspensions, we need to develop powerful tools for characterization of turbid materials including cells and tissues.

The widely accepted radiative transfer (RT) theory provides an accurate framework for quantitative characterization of light absorption and scattering in turbid materials [9]. The optical properties are obtained by solving the RT equation which describes how light energy propagates in a turbid media and supplemented by the Fresnel equation that defines boundary condition between two media with mismatching refractive indices. Based on the RT theory, the response of a homogeneous turbid sample to an optical excitation can be fully described by an absorption coefficient $\mu_a$, a scattering coefficient $\mu_s$, and a single-scattering phase function $p(\theta, \varphi)$ with $\theta$ and $\varphi$ as polar and azimuthal angles of scattered light. In most cases, $p(\theta, \varphi)$ can be treated as an axial

symmetric function and further simplified by a single-parameter function fully characterized by an anisotropy factor g =<cosθ>. With these approximations, the optical properties of homogenous turbid sample can be expressed by a set of 3 optical parameters of $\mu_a$, $\mu_s$ and g, which in general are functions of wavelength λ.

Several previously reported spectrophotometric methods use the RT equation or diffusion approximation with the boundary conditions described by the Fresnel equations in a wide spectral region to obtain the 3 optical parameters [10-14]. Most of these methods use integrating spheres for light signal measurements where a turbid solid sample sandwiched between two glass slides is held between two integrating spheres. The use of integrating spheres method to measure light signals offer numerous advantages such as the ability to reduce complexity for modeling and/or numerical simulation time and ability to accurately measure divergent beams. However, the use of integrating spheres presents some significant challenges such as sample assembling, maintaining highly-diffusive reflective internal surfaces, installation of sphere accessories on spectrophotometers, sample-detector angles and distances inflexibility and sphere internal reflectance losses [10, 14]. Moreover, for the measurement of these optical parameters, the existing methods need to measure collimated transmittance $T_c(\lambda)$ and calculate the attenuation coefficient $\mu_t$ of a sample of thickness *d* from the Beer-Lambert law. This approach requires no or minimal contribution of forwardly scattered light to $T_c$ and this can only be achieved by using samples of small optical thickness of $\mu_t d \sim\leq 5$ and a spatial filtering system to reduce forward scattering contribution to $T_c$ [10]. Thus, one need to prepare samples of small *d* for materials of large $\mu_t$, which makes it difficult to measure *d* accurately leading to $\mu_t$ measurement errors. In addition, to obtain $\mu_t$ from $T_c$ and *d* from the Beer-Lambert law, two or more turbid samples of different thickness may be needed to increase $\mu_t$ measurement accuracy by ensuring a linear relation

between ln($T_c$) and d. This approach makes measurements of cell samples very challenging because of the difficulties of preparing multiple identical turbid samples that are of cell suspensions. A new spectrophotometric system has been recently developed and validated in our research group which acquires measured light signals from a turbid sample without using integration spheres[15]. However, this method still has to use Tc signal to obtain $\mu_t$ which is then used to calculate single scattering albedo *a*. This method although a major departure from the existing methods, still suffers the same limitations for using $T_c$ light signal to obtain $\mu_t$.

The goal of this dissertation research is two-fold: To develop a new spectrophotometric method for determination of optical parameters based on the RT theory without using integrating spheres or $T_C$ light signals and apply the method as a label-free assay to investigate cellular apoptosis. The new method requires development of an experimental system that can accurately be used to acquire measured light signals from a sample and an accurate numerical model to obtain calculated signals by simulating the sample-detector configuration of the system. To validate the new method, we have experimentally obtained the optical parameters of microsphere suspension samples and performed result comparison to modeling by the Mie model based on classical electrodynamic theory. Results show that the optical parameters obtained by the two methods are closely matched. The new method has been then applied to investigate its ability on detection of apoptotic cells as an alternative approach for label-free assay of cellular apoptosis based on the cells' morphological changes. The MTT cell viability assay and fluorescent flow cytometry (FCM) apoptosis staging assay have also been carried out to compare with those by the new method. We have demonstrated that even though the new spectrophotometric method can still be improved, in its current form it can still predict apoptosis with almost the same accuracy as the existing assays such as FCM.

Numerous apoptosis staging assays have been developed in the past to study cells undergoing apoptosis after treatment with a chemotherapy drug[16]. Although these methods offer different advantages, they also suffer from some shortcomings. For instance, clonogenic assay is one of the most accurate viability assays, but it takes several weeks before getting results depending on cell line. The MTT assay can be automated to rapidly obtain results, but this assay can be used to classify viable cells only and the same time it requires one to establish standard calibration curve for absorbance for each cell line. Lastly, while the FCM can rapidly sort treated cells into 4 apoptosis stages unlike other existing methods, its application is limited due to the high cost of the cytometer equipment and the fluorochromes used to stain the cells. In this dissertation, we developed a new spectrophotometric method which is easy to assemble and fast in obtaining the data needed to study apoptosis of MCF7 cells treated with chemotherapy drug doxorubicin. This method allows the full analysis of cells optical properties by measuring three light signals of diffuse reflectance $R_d(\lambda)$, diffuse transmittance $T_d(\lambda)$ and forward transmittance $T_f(\lambda)$ from only one cell suspension sample and three single photodetectors. One notable difference with this new approach is the measurement of $T_f(\lambda)$ instead of $T_c(\lambda)$ as with the existing methods. This new methodology addresses most of the challenges associated with the existing spectrophotometric methods related to the use of integrating spheres for measuring light signals and the limitations of using $T_c$ light signal to obtain $\mu_t$. The measured light signals are then compared with the results from Monte Carlo simulations to obtain the optical parameters of $\mu_a(\lambda)$, $\mu_s(\lambda)$, and $g(\lambda)$ for $\lambda$ between 440 nm and 1000 nm in steps of 20 nm. As earlier mentioned, we validated this new method by obtaining the optical parameters of polystyrene microsphere suspensions and then comparing them to published results and those obtained by Mie theory calculations. The validated turbidity spectrophotometry system was then used to investigate apoptosis of treated MCF7 by

correlating the optical properties of the cells to the morphological changes associated with apoptosis. In addition to the control or untreated cell sample, we investigated three sets of cell samples consisting of cells treated with three different drug doses and with each of the sample post treated for specific duration or post treatment time. At the same time, we used conventional assays such as MTT and FCM to determine cell survival ratios and stage apoptosis of cells treated with same drug doses and post treatment times. By comparing the optical parameters of treated cells obtained with the new method to their corresponding cell viability results obtained by the existing viability assays, we were able to correlate the optical parameters of cell suspension sample to the corresponding apoptosis phase. The results of this study demonstrate that this new approach has the potential to study apoptosis of treated cells as an alternative to the existing methods such as FCM. It is fast and requires no prior cells preparations like staining.

This dissertation is organized into the following 5 chapters in addition to this introduction chapter. Chapter 2 provides the background information on existing spectrophotometric methods used to measure scattering light signals. In addition, this chapter highlights the conventional methods used to detect apoptosis and their limitations. Theoretical frameworks of light scattering and absorption by single particles as well as modeling light propagation in a turbid media is described in chapter 3. The new spectrophotometric system development and validation with microsphere measurements is described in chapter 4 including the diffuse light signal measurements and modelling with Monte Carlo code to obtain the optical signals. In chapter 5, all measurements of treated and untreated cells with the existing methods and the new spectrophotometric method will be presented in detail. Finally in chapter 6, we summarize and discuss the experimental results of this dissertation particularly the comparison of spectrophotometric results with those obtained by other conventional methods. This chapter will

also describe the significance of this study as well as offering a baseline for improving the results in future measurements or research studies.

# CHAPTER 2 Background

In this chapter, we will review existing methods of spectrophotometry for light signal measurement and sample characterization, and techniques related to cell apoptosis research. This will include an overview of spectrophometer's configuration and description of two widely used techniques for measurement of light scattering signals. In addition, we will describe the maintance of MCF7 cell-line in a cell cuture as well as the morphological changes associated with apoptosis as a mode of cell death. Chemotherapy drug-induced cell apoptosis will also be discussed including the biochemical process triggering and driving apoptosis.

## 2.1 Conventional spectrophotometric methods

When light interacts with a turbid sample such as cell suspensions, it is partially absorbed and partially scattered through depending on the optical properties of the sample. The elastically scattered light signals provide morphological information mainly on the scatterers inside the sample while light absorption reveals the chemical composition of the scatterers and hosting medium of the sample [17]. When the measured light signals are compared with calculated signals with appropriate light transport models, the inherent optical parameters of the sample can be obtained and used for analysis of sample conditions such as cell viability in the case of a suspension sample of treated cells. Several optical techniques have been developed and applied widely to measure scattered light signals to determine the optical properties of the sample [18].

Generally, spectrophotometric methods for study of sample turbidity measure scattered light intensity signals from a sample as a function of wavelength and inversely determine the optical properties of the sample by applying an optical model to obtain calculated signals and compare to the measured data iteratively until they fit. These methods vary by experimental designs and

optical models used in the inverse calculations. Several previously reported methods use the radiative transfer (RT) equation or a diffusion approximation with the boundary conditions described by the Fresnel equations in a wide spectral region [10-14]. In order to obtain optical parameters of a turbid sample, nearly all the conventional methods need to measure light signals in two steps. First, the collimated transmittance $T_c(\lambda)$ is measured to determine the attenuation coefficient $\mu_t$ from the Beer-Lambert law given by $\mu_t(\lambda) = -\ln[T_c(\lambda)]/d$, where d is the thickness of the sample. Then the signals of $R_d$ and $T_d$ are measured and used to inversely determine the optical parameters of absorption coefficient $\mu_a$, scattering coefficient $\mu_s$ and anisotropy factor g with $\mu_t = \mu_a + \mu_s$.

Conventional spectrophotometry, however, ignores light scattering in the measured signal of $T_c(\lambda)$ and determines only $\mu_t$ or absorbance $A(\lambda)=\log_{10}(1/T_c(\lambda))$. These instruments are easy to use and serve as tool-of-choice in many fields for characterization of non-turbid or absorbing samples over a wide spectral range but do not have capacity to fully characterize turbid samples. Several spectrophotometer designs for turbidity characterization have been developed in the past decades to measure light signals from turbid samples [10, 19]. For most of them, the overall system configuration remains the same even though the design might vary slightly based on different approaches of signal acquisition. They usually consist of a stable light source with continuous and broad range of wavelengths, a monochromator with a dispersive element to obtain a narrow band of selectable center wavelength and light detectors. The light may be modulated at specific frequency using a light chopper to enable phase sensitive detection of very weak signals from noisy background. The monochromatic beam is directed to a sample of interest with an intensity of $I_0$. The scattered or reflected/transmitted light is monitored by light detectors as measured signals for further analysis. Typically, a spatial filtering setup is used to measure the collimated

transmitted light intensity $I_c$ for collimated transmittance defined by $T_c = I_c/I_0$ for reducing the contribution of forward scatter to the detected signal. Fig. 2-1 illustrates the optical configuration for $T_c$ measurement.

If a photomultiplier or photodiode is used as the light detector, it outputs an electric current signal which is then converted into a voltage signal, amplified and digitized in a modern spectrophotometer. Because the light-matter interaction is strongly dependent on the wavelength of the incident light, it's very critical to calibrate the wavelength of output beam for an in-house built monochromator using a validated spectrometer over a wide spectral range. The resolution of a monochromator can be described in terms of its ability to disperse light according to wavelength and in its capability in selecting a wavelength band of desired bandwidth. Thus, the resolution depends on the diffraction grating efficiency and the width of the monochromator entrance and exit slits. The spectral resolution of in-house built monochromator is normally expressed as full-width-half-maximum (FWHM) of the peak in the measured output spectral data by the validated spectrometer [20].

## 2.2 Light scattering signal measurements

### 2.2.1 Light scattering signal measurement by integrating spheres

Most of the existing methods use integrating sphere system for hemispherical $R_d$ and hemispherical $T_d$ signal measurements in addition to the measurement of $T_c$ as shown in Fig. 2-1 [10, 19, 21-23]. Integrating sphere is a hollow spherical optical device internally coated with highly reflective material with small holes used as light entrance and exit ports. Light entering the sphere and reaching the inside surface of very high reflectance undergoes multiple diffuse reflections and a small photodiode installed on one side of the sphere collects a known fraction of the light intensity that entered the sphere [13]. While some methods use just one integrating sphere which

is rotated around the turbid sample to measure each light signal of $R_d$, $T_d$, and $T_c$ at a time, other methods employ two integrating spheres for simultaneous measurements of the three light signals [21, 24]. A schematic for this spectrophotometric technique is as shown in Fig. 2-1 (A)Typical schematic for integrating sphere system for measuring hemispherical scattered light signals (Rd and Td) using one integrating sphere rotated 180$^o$ to measure both light intensities. (B) Schematic for spatial filtering system for measuring collimated transmission $T_c$. A turbid sample is sandwiched between two glass slides and placed at the entrance port of an integrating sphere. Diffuse scattered light from the sample reaching the inner wall of the sphere is uniformly distributed over the entire sphere surface and a known portion of the integrated light measured using a photodiode.

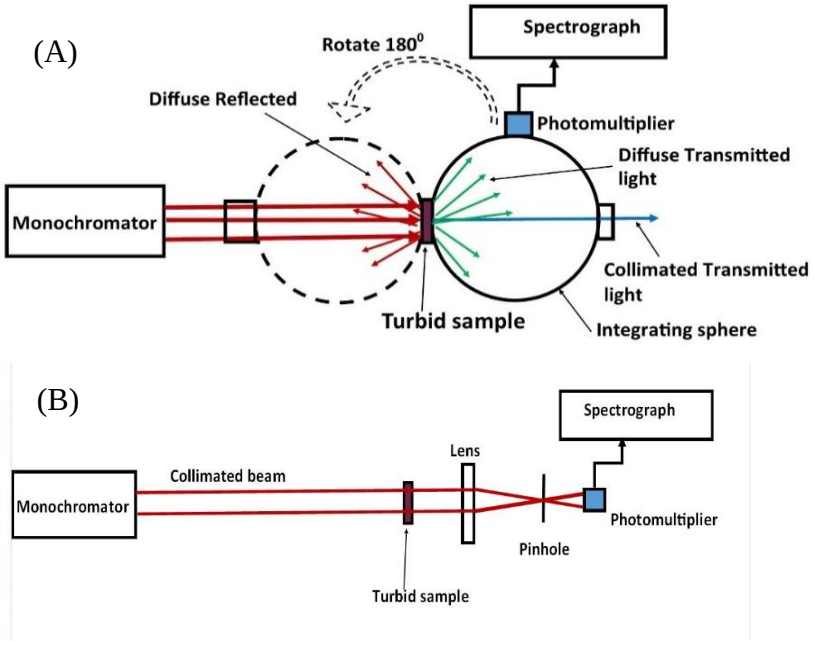


Fig. 2-1 (A)Typical schematic for integrating sphere system for measuring hemispherical scattered light signals (Rd and Td) using one integrating sphere rotated 180$^o$ to measure both light intensities. (B) Schematic for spatial filtering system for measuring collimated transmission $T_c$.

The use of integrating spheres offers an important advantage in the hemispherical measurement of $R_d$ and $T_d$ light from a sample. The hemispherical $R_d$ and $T_d$ signals eliminates detailed angular dependence of the scattered light which can significantly reduce complexity for modeling and

numerical simulation time. In addition, for samples of small attenuation coefficients, only a small portion of the incident beam is scattered. Thus, an integrating sphere can capture most of these weak light signals and averages them for $R_d$ and $T_d$ measurements without the need to align detectors to certain directions of scattered light for increasing the signal-to-noise ratios. However, the use of integrating spheres presents some significant challenges such as sample assembling and preparations, maintaining highly reflective internal surface of a sphere, installation of detector and the high cost of the integrating sphere devices [10, 14].

### 2.2.2 Light scattering signal measurement without using integrating spheres

Some of the existing spectrophotometric methods measure scattered light signals from a sample without using integrating spheres as shown in Fig. 2-2 by employing just single photodiodes which is a major shift from other methods[10, 25, 26].

This new approach of measuring scattered light has eliminated most of the challenges associated with integrating spheres for measuring scattered signals from a sample as described in the previous section 2.2.1. One downside of using single photodiodes for measuring scattered light signals is that they increase the complexity for modeling the signal detection and, in the case of

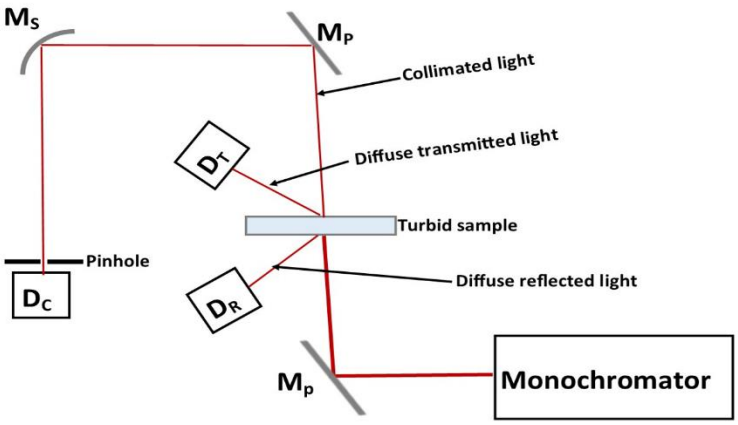


Fig. 2-2. Typical schematic setup of spectrophotometric system for measuring scattered light signals without using integrating spheres. $M_p$, plane mirrors; $M_s$, spherical mirror; $D_R$, $D_T$ and $D_C$ are photodetectors. Collimated light is measured using a spatial filtering system consisting of $M_p$, $M_s$ and Pinhole.

Monte Carlo simulations, numerical simulation time due to reduced signal sampling efficiency. The use of high-performance computing systems such GPU computers could however be used to address the limitation of increased computational cost.

## 2.3 Challenges and limitations of conventional methods

While the existing methods offers accurate technique for measuring scattered light from a turbid sample, they face one major challenge irrespective of whether they employ integrating spheres or single photodiodes. They all require one to obtain $\mu_t$ from measurement of $T_c$ and D using the Beer-Lambert law as described in Sub-section 2.1. This approach requires the contribution of forwardly scattered light to $T_c$ to be minimal and this can only be achieved by using samples of small optical thickness $\tau_s(=\mu_t d)$ in addition to using a spatial filtering system. For samples with small attenuation coefficient such as cell suspensions, either high cell density or thick sample is required to significantly increase the intensity of scattered light signals ($R_d$ and $T_d$) and this might lead to inaccuracies in $T_c$ measurements. To reduce the contribution of forward scattered light to Tc signal, a spatial filtering setup is usually added to the set up as shown in Fig. 2-1(B) and Fig. 2-2 which is an additional accessory. Thus, one needs to prepare samples of small thickness for materials of large $\mu_t$, which makes it difficult to measure d accurately. In addition, very thin samples usually lead to formation of air bubbles within a colloid sample. The presence of air bubbles within the turbid sample often causes extra light scattering due to induced inhomogeneity in the sample hence resulting to erroneous optical properties measurement [27]. In addition, to obtain $\mu_t$ from $T_c$ and d from the Beer-Lambert law as stated above, three or more samples of different thickness are typically needed to increase $\mu_t$ measurement accuracy by ensuring a linear relation between ln ($T_c$) and d. This might be challenging due to difficulties of preparing multiple

identical samples that are of cell suspensions. Thus, to accurately obtain the optical parameters of a thick turbid sample of small attenuation coefficient, there is a critical need to develop a new spectrophotometric method which does not require the measurements of $T_c$ and the use of Beer Lambert law to determine $\mu_t$. Such an approach will eliminate the sample requirements for $T_c$ measurements which is a significant impediment for accurately determining optical parameters for samples of small $\mu_t$. In this study, we will present a new spectrophotometric method to inversely obtain the optical parameters of one thick sample and without using the integrating spheres. This method is not only fast in acquiring the measured signals from a turbid sample, but also addresses most of the challenges associated with the existing methods as described earlier on this section. This new method developed by our group has been recently reported [1, 5].

## 2.4 MCF7 cells and apoptosis induction

### 2.4.1 MCF7 cell line

The MCF7 is a human breast cancer cell line derived from the pleural effusion of breast adenocarcinoma and is the most studied human breast cell line in the world [28]. Previous studies on the cells have shown them to have similar characteristics to that of mammary epithelium and hence a good choice for in vitro model study of breast cancer biology. The cell line is derived from a human primary breast cancer cell that express several variants such as estrogen, androgen, progesterone and glucocorticoid receptors making it very applicable in developing chemotherapeutic drugs and in studying drug resistance [29]. This cell line is also known to be relatively stable from one passage to the next and easy to grow in cell culture media. It is an adherent cell line which makes it easier to subculture without disturbing them unlike suspension cells which need to be centrifuged to subculture and thus slowing their growth. We thus settled on

this cell line for our study due the numerous benefits associated with its biological characteristics as well as its maintenance.

Cell culture makes it possible to grow cells outside the host tissue under controlled artificial conditions making it possible to conduct In-vitro studies on the cells. Unlike when cells are in host tissue, cell culture gives one an ability to manipulate the physio-chemical environment of media in which cells grow and thus having a control of the cell growth and proliferation. Although cell culture requirements may vary significantly for different cell lines, the general culture environment consist of a culture medium containing essential cell nutrients and growth factors, as well as a regulatable physio-chemical environment which can be controlled for conditions such as pH, humidity, osmotic pressure, temperature and gases among other factors [30]. The ideal complete growth medium of MCF7 cells consists of minimum essential medium (MEM) supplemented with 10% fetal bovine serum (FBS) and 0.01 mg/ml human recombinant insulin. Cells are grown in culture flasks with growth surface area of either 25 $cm^2$ ($T_{25}$) or 75 $cm^2$ ($T_{75}$) and maintained in a humidified incubator kept at a temperature of 37 $^0C$ and 5% $CO_2$ concentration. A continuous supply of 5% $C0_2$ in the incubator help maintain the pH of the culture media in the neutral range of 7.2-7.4. Phenol red reagent contained in the MEM is widely used as a pH indicator where it has red color in the 6.5-8.0 pH value range and yellow at acidic values below pH of 6.4. Depending on the cells density in the flask, the growth media is usually changed every three days for optimum results. For optimal growth, the seeding density should be $5\times10^4$ cells/$cm^2$ with respect to the culture flask [3]. If the cells are maintained in the ideal environment described above, their Population Doubling Time (PDT) is approximately 38 h as shown in Fig. 2-3. Subculturing of the cells into new flasks is recommended once they reach about 80% confluency.

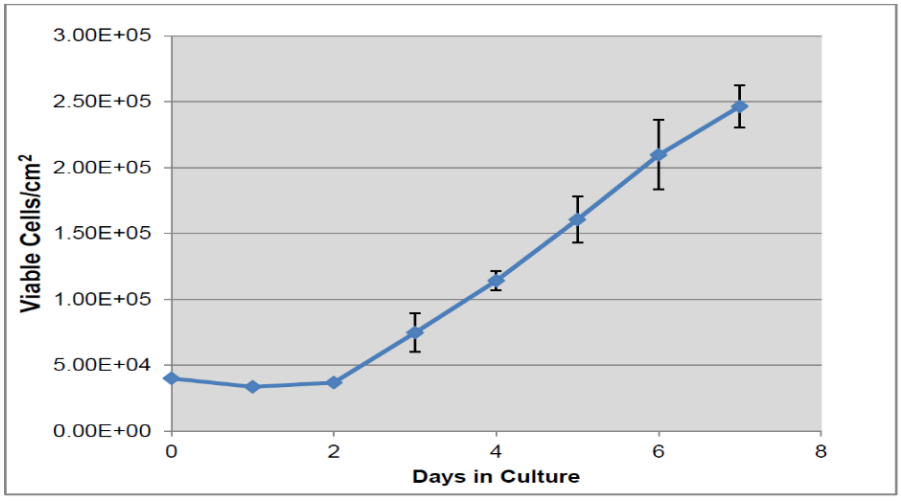


Fig. 2-3. Growth curve for MCF7 cells seeded at $4x10^4$ cells/$cm^2$ in ideal culture environment with Population doubling time (PDT) of about 38 hours. Adapted from [3].

### 2.4.2 Cell death and apoptosis

Cell apoptosis as a mechanism of programmed death plays a vital role in various processes such as maintaining cell populations in tissues, embryonic development, chemical-induced cell death, and proper functioning of immune system [31]. The ability of this process to regulate cell life and death offers an immense therapeutic potential especially in managing human conditions such as neurodegenerative diseases and various types of cancers. There are various physiological and pathological stimuli which can trigger apoptosis like for instance irradiation or cancer chemotherapy drug may lead to cell apoptosis by damaging the cell DNA [31]. The two main apoptotic activation mechanisms are the intrinsic pathway activated by intracellular signals and the extrinsic pathway which is as a result of extracellular agents binding to death receptors on the cell surface [32]. Although both pathways are initiated by different stimuli, they trigger apoptosis the same way by cleaving a caspase-3 protein which in turn leads to DNA fragmentation.

Cells undergoing apoptosis can be classified into either viable (V), early apoptotic (EA) and late apoptotic (LA) before they degrade into debris ($D_c$) at the end of the apoptosis process.

Cells at each stage of apoptosis carry unique biochemical and morphological hallmarks which can be used in staging the apoptotic pathway [33]. Early apoptosis of cells is characterized by the condensation of nuclear chromatin, and the shrinkage of both the nucleus and the overall cell. The late apoptosis is accompanied by nucleus fragmentation, plasma membrane blebbing, and separation of cell fragments into apoptotic bodies as shown in Fig. 2-4. Spectrophotometric measurements together with spectral analysis can be used as an alternative method for staging apoptosis due to the method's high sensitivity in detecting morphological and compositional changes of the cells.

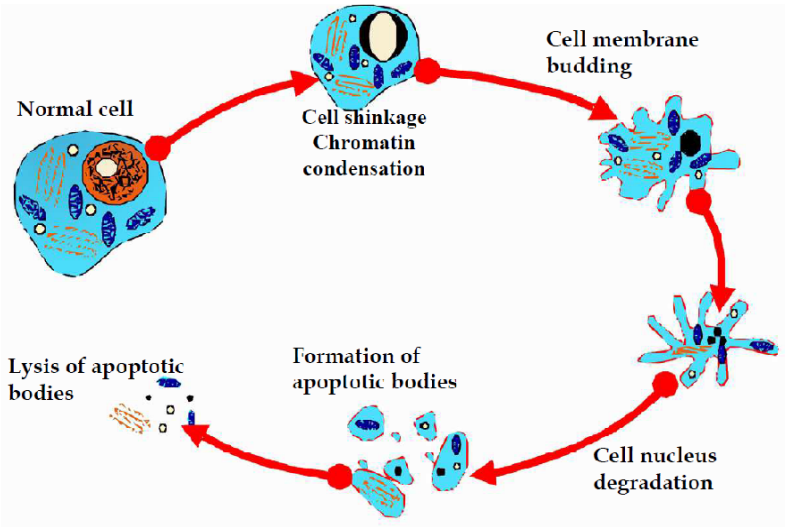


Fig. 2-4. Schematic for the morphological cell changes during apoptosis. Adapted from [4].

In oncological research, the effect of chemotherapy drugs to cancerous cells is studied by treating cells with the appropriate drug and determining the cells viability against drug dose or post-treatment time. Most chemotherapeutic drugs inhibit the growth of malignant cells by activation of the cell's apoptotic pathway. Doxorubicin hydrochloride is a well-known cytostatic anticancer drug widely used in chemotherapy to treat a variety of cancers and it acts by interfering with the synthesis of cellular RNA and DNA, hence arresting the proliferative nature of the

tumorous cells [34]. Thus, this drug acts as an extracellular agent binding to the cell surface death receptors by activating the apoptotic extrinsic pathway as described earlier in this Sub-section.

## 2.5 Existing methods of detecting apoptosis

Several apoptosis staging assays have been developed in the past to study cell apoptosis[16]. These assays are based on detection of one or more of the morphological and biochemical changes associated with the apoptosis process. Some of the apoptotic cell changes as mentioned above includes, chromosomal DNA fragmentation, membrane damage and blebbing, chromatin condensation, overall cell shrinkage, alteration in cell cytotoxicity and proliferation among other immunological changes [35]. Conventional methods which will be highlighted in this section include Clonogenic assay, MTT assay, fluorescent flow cytometry, and spectroscopic methods. Each assay can be useful in certain applications with different advantages and shortcomings.

### 2.5.1 Clonogenic assay

The clonogenic assay is a cell viability test method which has been in use in cell radiation biology studies for several decades [36-38]. It's based on the ability of a single cell to reproduce and form a colony of at least 50 cells. This assay is mainly employed to determine the reproductive viability of cells which have received various apoptotic-inducing treatments such as exposure to cytotoxic chemicals or ionizing radiation against the untreated cells as control. In brief, this assay consists of four distinct steps which include, (i) treatment of cells in tissue culture flasks (ii) plating distinct number of single cells suspension in a petri dish and incubating for a certain period of time depending on cell line (iii) fixing and staining the colonies with appropriate buffer and stain (iv) counting the colonies using either a light microscope or digital counting software [39]. This protocol is summarized in [2] and shown on Fig. 2-5 below. The treatment of the cells can be done before or after plating based on the aim of the study. For comparison of sensitivity and efficiency

of different treatments, cells are plated before treatment. To investigate the repair of damaged cells, the cells are treated before they are plated.

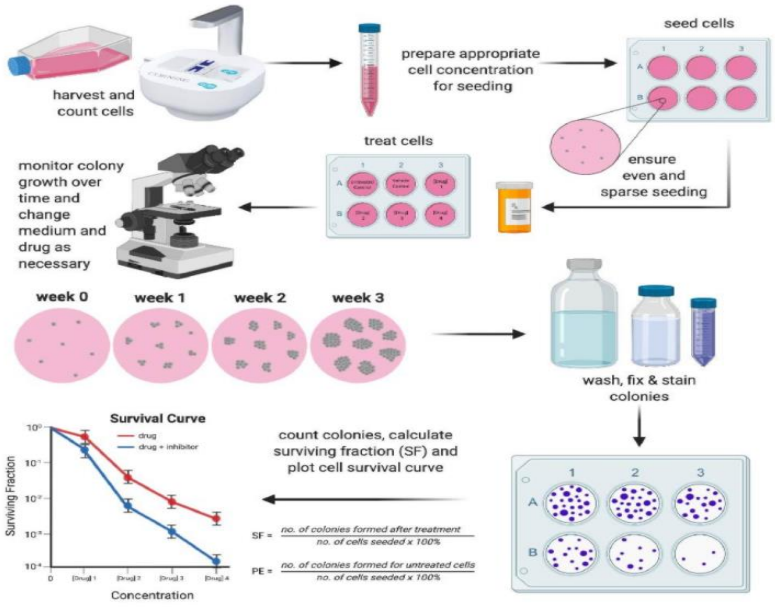


Fig. 2-5. Summary of Clonogenic protocol from cell seeding to obtaining the survival curve. Adapted from [2].

When untreated cells are plated as single cells at low densities, most of them will each grow into a colony over time based on their individual cell viability. The plating efficiency (PE) or the colony forming efficiency is then calculated as the ratio of number of colonies formed to the number of cells plated and it varies from one cell line to another. The PE is then used in the calculation of the surviving fraction (SF) of treated cells. The SF is basically the proportion of treated cells that grows into a colony, expressed in terms of PE and this gives an accurate calculation of the reproductive viability of the cells. In summary, the PE and SF are calculated using the following equations [38];

$$PE = \frac{\#\ of\ \ colonies\ formed}{\#\ of\ \ \ cells\ plated} \times 100\%$$
$$SF = \frac{\#\ of\ \ colonies\ formed\ \ after\ \ treatment}{\#\ of\ \ \ cells\ plated\ \ \times PE} \qquad (2.1)$$

Although this assay is the gold standard of cell death or survival assays based on the direct measurement of cells' colony forming ability, it has significant limitations. The procedure is complex and time consuming and it takes several weeks before getting results depending on cell line. Some tumor cells cannot grow in cell culture and some of them require cell to cell contact to proliferate hence making this method inapplicable. The technique is also limited by the number of carcinostatic agents and cell lines that can be simultaneously tested [40].

### 2.5.2 MTT assay

The MTT assay is an in vitro colorimetric method that measures enzymatic reduction of 3-[4,5-dimethylthiazole-2-yl]-2,5-diphenyltetrazolium bromide (MTT) into an insoluble MTT-formazan product in viable cells for assessing cell metabolic activity. The reduction requires catalyzation by mitochondrial succinate dehydrogenase and depends on mitochondrial respiration, which is lacking in abnormal or dying cells. The MTT assay can thus be used to assess the energy-producing capacity of a cell and has been widely used to indirectly quantify the cell viability [41]. It involves quantitative measurements of viable cells based on mitochondrial metabolic rate. The assay is based on the ability of viable cells to produce a nicotinamide adenine dinucleotide phosphate (NADPH)-dependent cellular oxidoreductase enzyme. This enzyme which is mainly produced in mitochondria reduces MTT, a yellow tetrazolium dye, to purple formazan crystals [42]. Because in most cells the total mitochondrial activity correlate to strong cell viability, the concentration of the formazan crystals in a treated cell sample is likewise proportional to the number of viable cells. A solubilization solution such as acidified propanol is added to the insoluble formazan crystals to dissolve them into purple solution with characteristic absorption between 500 nm and 600 nm. The absorbance of a cell sample is measured by a spectrophotometer specially designed for MTT assay (Multiskan MCC340) at a wavelength in the above range (550

nm for this study). To obtain a reasonably accurate survival curve for a specific cell line, a baseline calibration needs to be first performed to determine the relationship between absorbance and viable cells numbers. For the calibration curve, the net absorbance of the microtiter wells is plotted against the number of cells in the respective wells. The survival ratio S for the treated cells is then calculated as:

$$S = \frac{A_t - A_{nc}}{A_c - A_{nc}} \tag{2.2}$$

where $A$ is absorbance and $t$, $c$ and $nc$ in the subscripts are treated, control and negative control wells respectively.

One of advantage of this assay is that it requires minimal cell manipulation and thus is easily automated because the assay can be performed in 96-well plates with different cells treatment. However, this method presents numerous challenges as described elsewhere[43, 44] which include; (i)The metabolic activity in different cell lines varies, therefore a standard curve needs to be determined for each cell line to test for linearity and to measure the slope of the curve (ii) a small number of proliferating cells can easily be masked by large number of nonproliferating cells affecting viability results (iii) the pH of the cell media affects the MTT-formazan absorbance (iv) apoptosis inducing drug on treated cells can interfere with MTT absorbance measurements

### 2.5.3 Fluorescent flow cytometry

Fluorescent-based assays can be used to offer more information about the state of cells undergoing apoptosis as compared to MTT viability assay. As described in the Sub-section above, the MTT assay assesses the absorbance change of a cell sample and from this a survival ratio of all cells in the sample can be derived. It thus can only detect apoptosis in single cells as either viable or non-viable while fluorescent assay based on flow cytometry (FCM) can classify cells into viable, early apoptotic, necrotic, and late apoptotic/debris. The FCM method can rapidly

acquire scattered and fluorescence light signals from single cells as they pass through a laser beam, which allows detection and analysis of apoptotic conditions of the interrogated cells [45, 46]. In summary, the FCM method for apoptosis assay uses two types of reagents to stain the cells and the stained cells are quantified by the acquired fluorescent signals. One reagent is a fluorescent dye with molecules conjugated with human annexin V proteins that bind to phosphatidylserine (PS) molecules when they are on the outer leaflet of the cytoplasm membrane during early apoptosis stage. In a viable cell, the PS molecules are located on the intracellular side of the membrane but during apoptosis, they translocate to the extracellular side to mark the cell for removal by macrophages through phagocytosis. Apoptotic cells stained by the Annexin V reagent can thus be detected using a flow cytometer at excitation and emission wavelengths of 485 nm and 535 nm respectively. The second fluorescent reagent of propidium iodide (PI) is used as a cell viability agent as it only stains cell nuclei with compromised cytoplasm membranes. The compromised membrane allows the PI molecules to enter the cell and bind to the double stranded DNA inside nucleus by intercalating between the base pairs. This fluorophore can then be detected at excitation and emission wavelengths of 488 nm and 617 nm, offering a quick and reliable method to distinguish between viable, earl apoptotic and late apoptotic cells. The reagent PI only stains cells in late apoptosis stage.

| **Type of cells** | **Annexing V** | **Propidium iodide** |
|---|---|---|
| Normal live cells | - | - |
| Early apoptotic cells | + | - |
| Late apoptotic cells | + | + |
| Cell debris | + | + |
| Necrotic cells | - | + |

Table 2-1. Summary of cell staining by fluorescent reagents used in FCM

In addition to fluorescence measurements, the FCM method can be used to simultaneously measure the relative size and granularity of the cells based on their forward scattering (FSC) and side scattering (SSC) of incident laser light. This method offers numerous advantages such as, multiparameter analysis of cells, single cell analysis , rapid analysis of cells per second, and its ability to distinguish between apoptosis and necrotic cell death [46]. However, this method has some limitations including complexity in cell preparation and high assay cost associated with flow cytometer equipment and staining fluorochromes. In some cases, the excitation and emission spectra between staining fluorochromes and treatment drug may overlap leading to inaccurate results [47].

### 2.5.4 Spectroscopy methods

As discussed above, apoptosis is accompanied by unique physiological and morphological changes of the cell. This leads to the changes in the optical properties of the cells based on the interaction of light with the cells. Wavelength dependence of scattering and absorption coefficients can provide both the physiological and morphological information of the cells undergoing apoptosis. In particular, light scattering properties of cells is dependent on the cells' morphological and biochemical structures. While some use fluorophores, most of the conventional spectroscopic and optical methods for detecting apoptosis in cell cultures depend on light scattering to the morphological changes of the cells. These methods range from direct imaging techniques such as confocal microscopy, flow cytometry, optical coherence tomography (OCT) to more indirect techniques such as elastic scattering spectroscopy (ESS), optical scatter imaging (OSI) which involves fitting experimental data with theoretical models [6, 48-53]. The light scattering by the

cells is based on the basic principles of electromagnetic wave propagation by treating cells as spherical dielectric particles. While cells do not have perfect spherical shapes, their cellular scattering characteristics can be described using various light scattering models [54]. Unlike most apoptosis detection methods which require cell fixation and staining, most spectroscopic techniques can be performed without these cell disruptions. Some spectroscopic methods such as FCM and confocal microscopy, can be used to offer quantitative and qualitative information respectively of apoptotic cells but require cell staining [51].

ESS is one of the commonly used spectroscopic technique to study apoptosis by monitoring the change of light scattering properties because of morphological changes associated with apoptosis. It makes it possible to study the apoptosis of a population of cells without affecting the cells or their environment. Photons interacting will cells normally lead to elastic scattering due to discontinuities of the refractive index in the cells. An homogenous sphere model based on the Mie theory can then be used to obtain quantitative information of the cells based on their scattering spectra [55]. The probability of a cell illuminated by a plane wave to scatter light is dependent on the size parameter ($\alpha$) which relates the wavelength of the light to the size of the cell. The intensity of scattering is depends on multiple parameters such as the diameter of the cell, light wavelength, refractive index of the cell and surrounding media, and the scattering angle of the light [55]. ESS method relies on measuring the wavelength-dependent scattering of the cells at a known scattering angle then solving the inverse problem using models such as Mie theory to obtain the cells size distribution [55]. A detectable scattering spectra difference should be produced between normal and apoptotic cells based on morphology changes. A good number of spectroscopic methods for detecting apoptosis involves extracting size parameter from the cells backscattered spectra because a small change in the effective sizes of the cells produce a significant difference in the

backscattering pattern. A schematic set up for measuring wavelength dependence of backscattered light from cell cultures are as shown in Fig. 2-6. A broadband light from the source is delivered via a fiber optic cable to cell cultures consisting of either adherent or suspension cells. The light interacts with the cells and then the backscattered light collected at certain angle with another optic fiber. The collected light is then analyzed, and appropriate models used to extract morphological information of the cells.

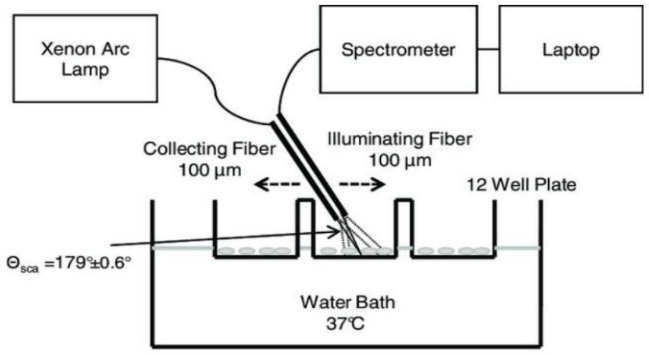


Fig. 2-6. Schematic of the ESS optical setup for backscattering measurements. Adapted from [6].

Optical spectroscopic methods used to detect apoptosis offer numerous advantages compared to other conventional cytochemical methods. Electron microscopy methods are fast and offer high spatial resolution qualitative information on apoptosis. Other techniques such as ESS are non-invasive and can be used to provide real time measurement results without interfering with sample's physiology or introducing potential artifacts [56]. However, these conventional optical spectroscopic techniques have several drawbacks which might limit their applications in studying cell apoptosis. For instance, flow cytometry measurements might be affected by cell clumping, while high energy electron microscopy techniques might affect cell viability after measurements as sometimes this need to be performed under vacuum [57]. The optical properties of the sample determine the average pathlength of the scattered and detected electrons limiting their use to

samples which are highly absorbing and less scattering leading to low signal-to-noise ratio. Lastly, backscattering techniques relying on angular and wavelength resolved measurements may be lengthy to take a full angular range measurements [58].

# CHAPTER 3 Theoretical framework

In this chapter, we discuss the principles used to relate the morphological and optical properties of small single particles such as polystyrene microspheres and cells to their ability to scatter and absorb light. We will first describe light-particle interaction by a wave model and then discuss light transport through a turbid sample by the radiative transfer (RT) theory. In addition, the Monte Carlo simulation method will be described which is used in this dissertation research project to obtain calculated light signals within the framework of RT theory. Lastly, the dependence of the optical parameters on the microscopic interaction cross sections of viable and apoptotic cells will be discussed.

## 3.1 Wave model of light scattering and absorption by single particles

The most accurate model of light transport in turbid media with scales much larger than light wavelength such as cell suspension is given by the RT theory, which can relate optical parameters of the turbid sample to the interaction cross-sections of single particles in suspension samples of sufficiently low particle concentrations. Since the above cross-sections can be determined from a wave model such as Maxwell equations or wave equations, measurement of microsphere suspension samples has been performed for system validation in this dissertation research. We will first introduce a wave model to define various interaction cross-sections and then discuss the Mie theory for modeling light scattering and absorption by a single sphere. Their relations to the three optical parameters, namely, absorption coefficient $\mu_a$, scattering coefficient $\mu_s$, and scattering phase function $p(\mathbf{s}, \mathbf{s}')$ as defined by the RT theory will be presented in the next section for samples of microsphere suspensions.

### 3.1.1 Light scattering and absorption by single particles

Electromagnetic (EM) radiation is a propagating electric and magnetic wavefields at a phase speed of $c=3.0\text{x}10^8$ m/s in vacuum and lower phase speeds of v in a homogeneous and non-absorbing host medium characterized by its refractive index (RI) n=c/v. Light scattering occurs at locations of heterogeneity in spatial distribution of RI which becomes a complex valued function of $n(\mathbf{r})=n_r(\mathbf{r})+in_i(\mathbf{r})$ for a medium that can also absorb light. Where r and i in the subscript represent real and imaginary parts. When an EM wavefield interacts with a molecule, for example, electrons may transit across energy states resulting in light absorption followed by light emission or non-radiative energy dissipation. Elastic scattering of light occurs when the scattered light's wavelength remains the same as the incident light, but propagation direction changed from a direction along a unit vector **s** to another along **s**'.

The intensity and direction of light scattered by a single particle depend on the wavelength of incident light and the complex refractive index distribution inside the particle relative to the host medium of $n_h$ for its RI [59]. The absorption and scattering of light by a particle can be expressed respectively in terms of absorption and scattering cross sections of the particle. To derive these parameters, we first need to understand how light interacts with a dielectric particle.

For simplicity, we consider here a plane electromagnetic wavefield propagating in vacuum as the incident light to a particle as shown in Fig. 3-1) as follows

$$\begin{aligned}\mathbf{E}_i(\mathbf{r},t) &= \mathbf{E}_o \exp(i\mathbf{k}\cdot\mathbf{r} - i\omega t)\\ \mathbf{B}_i(\mathbf{r},t) &= \mathbf{B}_o \exp(i\mathbf{k}\cdot\mathbf{r} - i\omega t)\end{aligned} \tag{3.1}$$

where $\mathbf{E}_i$ and $\mathbf{B}_i$ are incident electric and magnetic fields, $\mathbf{E}_0$ and $\mathbf{B}_0$ are the constant amplitudes, t is time, ω is the angular frequency. In Fig. 3-1, $\mathbf{k}_i$ and $\mathbf{k}_s$ are wave vectors of incident and scattered light wavefields respectively and have the same magnitude given by $|\mathbf{k}_i|=|\mathbf{k}_s|=2\pi/\lambda$ for elastic

scattering. The direction of the scattered light wavefields is characterized by polar angle of θ and azimuthal angle of ϕ.

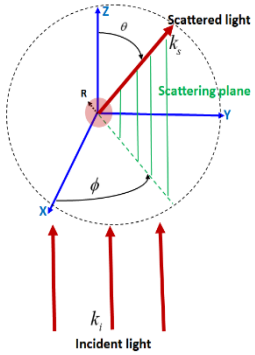


Fig. 3-1. Schematic configuration of light scattering by an arbitrary particle.

When light is incident on a particle, its electromagnetic fields induce oscillating electric and magnetic dipole moments which emit secondary light in all directions as the scatter wavefields of ($\mathbf{E}_s$, $\mathbf{B}_s$). Additionally, some of the incident light's energy is converted to molecular vibrational energy and dissipated as heat to the particle's surrounding media leading to light absorption [60]. The amount of light absorbed, and the spatial distribution of the scattered light depends on the RI distribution within the particle and relative to that of the host medium. RI is the refractive index of the sphere given as $n_s=n_r+in_i$. As an incident beam of light ($\mathbf{E}_i$, $\mathbf{B}_i$) encounters a particle, scattered wavefields ($\mathbf{E}_s$, $\mathbf{B}_s$) can be observed in the far-field from the particle. The superposition of the incident field and the scattered field yields the total wavefields of ($\mathbf{E}_t$, $\mathbf{B}_t$) as shown below [61].

$$\begin{aligned} \mathbf{E}_t &= \mathbf{E}_\mathbf{i} + \mathbf{E}_S \\ \mathbf{B}_t &= \mathbf{B}_i + \mathbf{B}_s \end{aligned} \tag{3.2}$$

The total wavefields must satisfy the Maxwell equations in region of interest and can be written in differential form as follows for dielectric and non-magnetic media,

$$\nabla \cdot \mathbf{D} = 0$$
$$\nabla \cdot \mathbf{B} = 0$$
$$\nabla \times \mathbf{E} = -\frac{\partial \mathbf{B}}{\partial t} \tag{3.3}$$
$$\nabla \times \mathbf{B} = \mu_o \varepsilon \frac{\partial \mathbf{E}}{\partial t}$$

where we have assume that no free charge density or current exists in the region of interest, $\mathbf{D}=\varepsilon(\mathbf{r})\mathbf{E}$ is the electric flux density and $\mathbf{H}=\mathbf{B}/\mu_0$ is the magnetic field strength, $\varepsilon(\mathbf{r})$ and $\mu_0$ are respectively the electric permittivity and magnetic permeability of the dielectric and non-magnetic media where the fields are to be measured.

To study the optical properties of a scattering particle, the unique scattering field produced by the interaction of light with the scattering particle need to be calculated. This problem can be solved by finding the solutions to Maxwell equations for light scattering by a spherical particle. The size of the scattering particle is usually expressed in terms of a dimensionless size parameter $\alpha$ which relates the particle's diameter or size $d_s$ to the wavelength $\lambda$ of the incident light in the host medium as follows

$$\alpha = \frac{\pi d_s}{\lambda} \tag{3.4}$$

Analytical modeling of light scattering by single particles to calculate the scattered wavefield by solving Maxwell equations or wave equations can be achieved with multiple method. Mie theory (after Gustav Mie) is one of the most widely used methods that can yield accurate solutions for single spheres of any size as a scatterer [62]. Other methods have been developed for non-spherical particles with various degree of approximations. For example, the Rayleigh scattering theory applies for light scattering by non-absorbing particles of very small size parameters or $\alpha<<1$. In this case, the phases of the electromagnetic fields do not significantly change across the particle. This means that all induced dipoles within the particle oscillate under a field with nearly

uniform phase and hence produce scattered field with the same phase if we detect the scattered light signals in far-field. Since the scattered field is solved by treating scattering particles as electric dipoles which oscillate with uniform phase equivalent to that of incident light wave and as a result, the particle scattering cross section varies inversely with the fourth power of the incident light wavelength [63]. The elastic scattering cross section of light for these very small particles can be found as follows by the Raleigh theory

$$\sigma_{sca} = \frac{2\pi^5 d^6}{3\lambda^4}\left(\frac{n^2-1}{n^2+1}\right)^2 \tag{3.5}$$

where n is the RI of particle.

### 3.2 The Mie Theory

In this dissertation research, polystyrene microspheres of sizes ~1-11 μm will be used as scattering particles for system validation, and MCF7 cells of sizes ~20-25 μm for the system application. The light wavelengths to be used will be in the range 460-1000 nm. From these values, the scattering size parameter α (πd/λ) will be approximately $3 \leqslant \alpha \leqslant 80$ and $60 \leqslant \alpha \leqslant 170$ for polystyrene microspheres and MCF7 cells respectively. Mie scattering theory will thus be the best choice for describing light interaction with a single particle in our study because unlike the other light scattering theories, it does not require the condition of $1 >> \alpha >> 1$ to be fulfilled[64].

Mie scattering theory describes light interaction with a particle by solving Maxwell equations in spherical coordinates as described in details elsewhere [65]. Mie theory has no limitation to the size of the scattering particle and hence converges to the limit of geometric optics for both large and small particles. Combining Mie theory and an appropriate modelling tool such as Monte Carlo simulation offers a suitable method to describe light interaction with microsphere suspensions particularly for calibrating optical instruments [1]. In brief, the Mie solutions to the Maxwell

equations takes the form of an infinite series of multipole expansion of polarization in a medium with suspended spherical scatters due to an incident light [64]. Legendre polynomials are used to expand the incident light to a particle so that the solutions inside and outside a scattering spherical particle can be matched at the boundary. At far-field region, which is a distance much larger than the wavelength of the incident light wave, the solution can be expressed inform of two scattering functions S(θ) as shown below:

$$S_1(\theta) = \sum_{n=1}^{\infty} \frac{2n+1}{n(n+1)} \left[ a_n \pi_n(\cos\theta) + b_n \tau_n(\cos\theta) \right]$$
$$S_2(\theta) = \sum_{n=1}^{\infty} \frac{2n+1}{n(n+1)} \left[ (b_n \tau_n \cos\theta) + a_n \pi_n(\cos\theta) \right] \tag{3.6}$$

where θ is the scattering angle, $a_n$ and $b_n$ are respectively the coefficients for electric and magnetic multipole radiations, and *n* the order of the spherical Bessel function. The $\pi_n$ and $\tau_n$ are functions of scattering angle related to Legendre polynomials and expressed as follows

$$\pi_n = \frac{P_n^1(\cos\theta)}{(\sin\theta)}$$
$$\tau_n = \frac{dP_n^1(\cos\theta)}{(d\theta)} \tag{3.7}$$

The scattering functions can be used to express the scattered components of electric field in terms of the incident components as shown in the equation below

$$\begin{bmatrix} E_l^s \\ E_r^s \end{bmatrix} = \frac{e^{ik(z-r)}}{ikr} \begin{bmatrix} S_2(\theta) & 0 \\ 0 & S_1(\theta) \end{bmatrix} \begin{bmatrix} E_l^i \\ E_r^i \end{bmatrix} \tag{3.8}$$

where $E_l$ and $E_r$ are electric fields parallel and perpendicular to a reference plane. One physical quantity which can be obtained from the scattered fields is the cross-sections. Absorption cross-section $\sigma_a$ and scattering cross-section $\sigma_s$ are respectively the ratio of absorbed energy rate and scattered energy rate to incident irradiance. The extinction cross-section $\sigma_e$ is the superposition of the absorption and scattering cross-sections and is the total amount of incident field energy

removed by absorption and scattering by a particle. The three cross-section parameters as $\sigma_s$, $\sigma_a$, and $\sigma_e$ can thus be described using Mie theory as shown below

$$\begin{aligned}\sigma_s &= \frac{2\pi}{k^2}\sum_{n=1}^{\infty}(2n+1)(|a_n|^2+|b_n|^2)\\ \sigma_e &= \frac{2\pi}{k^2}\sum_{n=1}^{\infty}(2n+1)(a_n+b_n)\\ \sigma_a &= \sigma_e-\sigma_s\end{aligned} \tag{3.9}$$

The Mie scattering phase function can be derived from $\pi_n$ and $\tau_n$ functions defined in Eq.(3.7) and used to define the anisotropy factor g as follows

$$g=\frac{4\pi}{k^2\sigma_s}\left\{\sum_{n=1}^{\infty}\frac{2n+1}{n(n+1)}\mathrm{Re}(a_nb_n^*)+\sum_{n=1}^{\infty}\frac{n(n+1)}{n+1}\mathrm{Re}(a_na^*_{n+1}+b_nb^*_{n+1})\right\} \tag{3.10}$$

The other optical properties $\mu_a$ and $\mu_s$ of a sphere suspension sample can also be expressed in terms of particles' scattering and absorption cross-sections, and their concentrations as follows

$$\mu_a=\sigma_a\rho \tag{3.11}$$

$$\mu_s=\sigma_s\rho \tag{3.12}$$

where ρ is the number density of particles.

### 3.3 Modeling of light propagation in turbid media

As described in section 3.2, Mie scattering theory provides an exact solution for light scattering by homogenous absorbing or non-absorbing spheres by solving the wave equations for the wavefields of scattered light. However, this theory does not adequately address the case for turbid media like biological cells which is comprised of many and irregular shaped scattering particles where light undergoes multiple scattering. It is thus very difficult to solve light scattering problems in a turbid sample according to a framework based on the Maxwell equations. Instead, an energy approach can be used for such problems by characterizing the spatial distribution of light intensity

in a turbid media. This allows quantification of the optical response of the media to incident light by its optical properties of $\mu_a$, $\mu_s$ and g, which are discussed below.

The radiative transfer (RT) theory describes light propagation through media consisting of absorbing and scattering particles by factoring all light absorbing, emitting and scattering events [66]. The basic equation used to describe the RT theory is based on the conservation of energy and can be expressed as

$$\mathbf{s}\cdot\nabla L(\mathbf{r},\mathbf{s}) = -(\mu_a+\mu_s)L(\mathbf{r},\mathbf{s}) + \mu_s\int_{4\pi} p(\mathbf{s},\mathbf{s}')L(\mathbf{r},\mathbf{s}')d\omega' + S(\mathbf{r},\mathbf{s}) \tag{3.13}$$

where **s** is unit vector in the direction of light propagation, L(**r**, **s**) is the radiance ($W\cdot sr^{-1}\cdot m^{-2}$) describing the power flux propagating at **r** position and along the **s** direction per unit solid angle, the scattering phase function p(**s**, **s'**) describes the probability of light being scattered from **s**'to **s** direction, and the terms S(**r**, **s**) is the radiance from light sources. In general, we can ignore S if the medium is source-free. So Eq. (3.13) becomes

$$\mathbf{s}\cdot\nabla L(\mathbf{r},\mathbf{s}) = -\mu_a L(\mathbf{r},\mathbf{s}) - \mu_s L(\mathbf{r},\mathbf{s}) + \mu_s\int_{4\pi} p(\mathbf{s},\mathbf{s}')L(\mathbf{r},\mathbf{s}')d\omega' \tag{3.14}$$

Based on vector analysis, the gradient operator ∇ on a scalar function L produces a vector whose direction is along the maximum increase direction of L and its magnitude is equal to the increasing rate of L along unit pathlength. The left-hand-side of Eq. (3.14) has **s**·∇L(**r,s**), which provides the component of vector ∇L projected along the **s** direction. Therefore, this term describes the increase of radiance per unit pathlength along **s**. On the right-hand-side of Eq. (3.14) the first and second terms describe the attenuation rate of radiance per unit pathlength due to absorption and scattering loss. Each term is characterized by a coefficient of $\mu_a$ or $\mu_s$. Adding these two yields the attenuation coefficient $\mu_t = \mu_a + \mu_s$. The third term means the increase rate of L due to scattering of light from **s'** direction to **s**.

In order to clearly identify the meaning of each of the three parameters of $\mu_a$, $\mu_s$ and p (**s**, **s**') defined in Eq. (3.14) we may break the equation into three component equations as follows

$$\mathbf{s}\cdot\nabla L_{a-loss}(\mathbf{r},\mathbf{s}) = -\mu_a L_{a-loss}(\mathbf{r},\mathbf{s}) \tag{3.15}$$

$$\mathbf{s}\cdot\nabla L_{s-loss}(\mathbf{r},\mathbf{s}) = -\mu_s L_{s-loss}(\mathbf{r},\mathbf{s}) \tag{3.16}$$

$$\mathbf{s}\cdot\nabla L_{s-gain}(\mathbf{r},\mathbf{s}) = \mu_s \int_{4\pi} p(\mathbf{s},\mathbf{s}')L_{s-gain}(\mathbf{r},\mathbf{s}')d\omega' + G \tag{3.17}$$

where G is a term to ensure that the solutions of the above equations from (3.15) to (3.17) can be combined to yield the solution of Eq. (3.14) or

$$L(\mathbf{r},\mathbf{s}) \;=\; L_{a-loss}(\mathbf{r},\mathbf{s}) + L_{s-loss}(\mathbf{r},\mathbf{s}) + L_{s-gain}(\mathbf{r},\mathbf{s}). \tag{3.18}$$

The linear differential equations of Eq. (3.15) and Eq. (3.16) can be easily solved to obtain

$$L_{a-loss}(\mathbf{r},\mathbf{s}) = L_0(\mathbf{r}_0,\mathbf{s})e^{-\mu_a D} \tag{3.19}$$

$$L_{s-loss}(\mathbf{r},\mathbf{s}) = L_0(\mathbf{r}_0,\mathbf{s})e^{-\mu_s D} \tag{3.20}$$

where $L_0$ is some integral constant related to boundary condition and D is the pathlength measured from $\mathbf{r}_0$ to **r** along **s** direction. From Eq.(3.19) and Eq.(3.20), we can immediately recognize the meanings of the two coefficients as, $(\mu_a)^{-1}$ which is the pathlength over which light radiance is reduced by $(1\text{-}e^{-1})$=63.2% due to absorption attenuation only, and $(\mu_s)^{-1}$ which is the pathlength over which light radiance is reduced by $(1\text{-}e^{-1})$=63.2% due to scattering attenuation only without considering the scattering gain.

As defined by Eq. (3.17), the scattering phase function p (**s**, **s'**) is in general a function of polar and azimuthal angles of $\theta$ and $\phi$ measured from the **s** direction to **s'**. Even though a specific application may not possess axial symmetry in light scattering, we can still use the simplified phase function on the basis that it is averaged over multiple scattering events. A widely used axial

symmetric function to replace p(**s**, **s'**) is the Henyey-Greenstein (HG) function $p_{HG}(\cos\theta)$, which has the form of single-parameter function given below [67]

$$p_{HG}(\cos\theta) = \frac{1-g^2}{4\pi(1+g^2-2g\cos\theta)^{3/2}} \tag{3.21}$$

where the anisotropy factor *g* is equal to the angularly averaged value of cos (θ). The relation can thus be written as

$$g = \int_{4\pi} p(\mathbf{s},\mathbf{s}')\cos\theta d\omega' = 2\pi\int_0^{\pi} p_{HG}(\cos\theta)\cos\theta\sin\theta d\theta \tag{3.22}$$

From the above equation, one can see that $-1 \leqslant g \leqslant 1$ where g=1, 0 and -1 corresponds respectively to the completely forward scattering, isotropic scattering, and completely backward scattering of light.

Several computational techniques have been developed in the past to solve the RT equation analytically and numerically. However, closed-form solutions of RT equation and Fresnel's formula for complicated boundary value problems cannot be obtained using analytical methods. Analytical methods usually deploy approximations and quickly reaches their limits as problem complexity increases [68]. For instance, the diffuse approximation method has been shown to fail when the medium have void-like regions consisting of low scattering and absorption or when the condition of $\mu_a \leq\leq \mu_s$ is not met [69]. Instead, numerical methods such as multiflux, discrete ordinate, and adding-doubling methods are used to numerically solve the RT equation as described elsewhere [70-72]. Although these methods can offer closed-form forward solutions to RT equation, their limitations come from the need to develop a sophisticated algorithm to simulate the actual sample geometric configuration and minimize the inevitable numerical errors introduced by the solution schemes [73]. Instead of employing analytical or purely numerical methods as described, a statistical Monte Carlo method offers a different robust approach to solving RT

problem by "mimicking" the actual scenario by tracking photons through a medium until they are either absorbed or escapes the medium. This method which will be used in our study is described in detail in the next section.

## 3.4 Light signal calculation by Monte Carlo simulation

As described in section Sub-section 3.3, the problem of light propagation in turbid media can best be defined as a boundary value problem described by RT and supplemented by Fresnel equations [74]. Using this approach, the light propagation in a turbid media can be characterized by scattering $\mu_s$, $\mu_a$, and a single-scattering phase function, $p(\theta, \phi)$ which is usually approximated by a single parameter g [74]. A statistical individual Monte Carlo (iMC) method can be used to provide a simple and accurate method to obtain the exact solution to 3D problems of RT equation [10, 12, 19, 75, 76]. This method consists of two components where a forward model is used to obtain calculated signals of $R_d$, $T_d$, and $T_c$ or $T_f$. An inverse model is then used to inversely obtain the optical parameters $\mu_s$, $\mu_a$, and g using the calculated signals by use of a robust perturbation algorithm. The iMC code for tracking individual photons in a turbid media used in this study is a modification of existing algorithm developed before and described in details elsewhere [10, 26, 77]. The iMC code can be briefly described as follows. A sample-detector configuration consists of a turbid sample contained in a circular shim sandwiched by two glass slides and three photodetectors placed at set orientations and distances from the sample. We will label the photodetectors measuring the $R_d$, $T_d$ and $T_c$ or $T_f$ signals as $D_2$, $D_3$ and $D_4$ respectively. The incident beam at the sample holder's front surface is represented by incident photons as $N_0$. The total number of photons reaching $D_2$, $D_3$ and $D_4$ are respectively $N_2$, $N_3$ and $N_4$. Simulation starts by injecting photons to a turbid phantom sample whose optical parameters of $\mu_s$, $\mu_a$ , and g have been initialized. Before the photons are injected, the total travel distance $L_a$ inside the turbid sample

is calculated for each photon from $\mu_a$ and a random number RND uniformly distributed in [0, 1] as follows

$$L_a = \frac{-\ln(RND)}{\mu_a} \tag{3.23}$$

Each photon is tracked as it enters the air-glass and the glass-sample interfaces to determine if it is reflected or transmitted across the boundaries. The photon incident angle and refractive indices of the two media at a boundary are used to calculate the Fresnel reflectance which is compared to a random number uniformly distributed in [0, 1] to decide if the photon is transmitted or reflected. The same principle applies to photons crossing from media to glass and glass to air. The photon undergoes random steps inside the turbid sample with each step distance $L_{si}$ determined by $\mu_s$ and direction by g, using HG function as the scattering phase function

$$L_{si} = \frac{-\ln(RND)}{\mu_s} \tag{3.24}$$

where i=1,2…j is the sequence number of scattering events. After each event inside the turbid sample, the total pathlength for each photon is updated as $L_s$ as shown below.

$$L_s = \sum_{i=1}^{j} L_{si} \tag{3.25}$$

If $L_s > L_a$, the photon is terminated otherwise it undergoes another scattering step as shown in Eq. (3.24). For the photons exiting the sample holder configuration, they are determined if they hit any of the three photodetectors. After all of the $N_0$ photons have been tracked and those reaching the photodetectors registered, the simulated signals of $R_d$, $T_d$ and $T_c$ or $T_f$ are then calculated as follows

$$R_{ds} = \frac{N_2}{N_0}, \qquad T_{ds} = \frac{N_3}{N_0}, \qquad T_{cs} \text{ or } T_{fs} = \frac{N_4}{N_0}. \tag{3.26}$$

Although Monte Carlo simulations of photon transport through a turbid sample offer a simple and yet robust approach toward numerically solving the RT, its computationally intensive especially if large number of photons are to be tracked to through a high absorbing and scattering medium. However, recent exponential improvement of computer speeds particularly the shift from CPU to GPU computing platforms have significantly solved this problem. In addition, the Monte Carlo simulation can also be affected by the biasness introduced by the Pseudo-random number generator's initial seed and hence affecting the uniform distribution of the random numbers used in the simulation [78].

## 3.5 Optical parameters of apoptotic cell suspensions

A turbid sample with apoptotic induced cells contains a mixture of viable, early and late apoptotic, and cell debris. An untreated or control sample is expected to contain viable and cell debris only. When light is incident to a cell suspension sample, the sample cell constituents together with the suspending media affects the way the light is absorbed and scattered. Since the measured light signals from a cell suspension sample are used in the simulation of the optical properties of the turbid sample, the proportion of the contribution of each sample constituents need to be quantified. The proportion of each cell conditions in a sample at depends on the drug dose and post treatment time. Cell survival curve measurement from previous studies shows that the viability of MCF7 cells is inversely proportional to the dose of doxorubicin drug up to the 10 μM for post-treatment time >10 hours [79].

As described in Subsection 3.2, the optical properties $\mu_a$, $\mu_s$ and g of a turbid cell sample depend on the cells' effective scattering and absorption cross-section and the number density ρ of the sample as shown in Eqs. (3.11) and (3.12). The scattering and absorption cross-sections of cells at different stages are expected to vary. Apoptosis cell morphology studies in the past has shown

that viable MCF7 cells have an average cell size of 19.7±3.8 μm and that there is a significant apoptotic cell volume decrease as cells transition from viable to late stages of apoptosis [80, 81]. Moreover, from recent MCF7 cells morphology studies in our group, results shows that overall, the volume and diameter of cells reduce by ~38% and ~13% respectively after transiting from viable to apoptotic stage [82]. This notable change of cells morphology would greatly affect how they absorb and scatter light and hence their inherent optical properties of $\mu_a$, $\mu_s$ and g at each apoptosis stage. We can rewrite the above parameters as sums of the contributions from each condition of cells as

$$\mu_a = \sigma_{av}\rho_v + \sigma_{aEA}\rho_{EA} + \sigma_{aLA}\rho_{LA} + \sigma_{aDc}\rho_{Dc} \tag{3.27}$$

$$\mu_s = \sigma_{sv}\rho_v + \sigma_{sEA}\rho_{EA} + \sigma_{sLA}\rho_{LA} + \sigma_{sDc}\rho_{Dc} \tag{3.28}$$

$$g = \rho_v g_v + \rho_{EA} g_{EA} + \rho_{LA} g_{LA} + \rho_{Dc} g_{Dc} \tag{3.29}$$

where ρ's with different subscripts are the cell number density of different types or cellular debris as defined above, subscript *a* and *s* refers to absorption and scattering respectively.

In this study, the total number of cells per sample (cell density) among the samples to be compared is kept approximately the same at the beginning of treatment so that the relative optical properties will only be dependent on the scattering and absorption cross-section of different particles assuming no co-occurrence of aggregation. Each individual cell's geometrical cross-section depends on its size and morphology and thus the cross-sections in Eqs. (3.28) and (3.29) are their mean values per sample. Early stages of cell apoptosis process are associated with unique morphological cell changes such as cytoplasmic and nuclear condensation, and overall cell shrinkage [31]. The late stages of cell apoptosis likewise are accompanied by morphological changes such as cell membrane blebbing, nuclear fragmentation and formation of apoptotic bodies as shown in Fig. 3-1. This change of size and morphology can be used to stage apoptosis because

of the cross-sections are correlated to cells or particles' morphology and intracellular changes in refractive index distributions such as those of nucleus, lysosome and mitochondria [83]. Early apoptosis is accompanied by cell shrinking hence reducing the effective scattering and absorbing cross sections. Late apoptosis and cell debris phases of apoptosis are accompanied by disintegration of cell's organelles including the cell membrane and hence reducing the overall effective absorbing and scattering cross-sections. The cell membrane and suspension media interface present a refractive index mismatch so any slight changes in the cell membrane significantly affect light scattering. Cells in these last two phases of LA and $D_c$ are expected to scatter and absorb light less compared to those in early apoptosis and viable phases due to their significant loss of turbidity and thus the overall reduction of scattering and absorbing cross-sections.

The scattering and absorbing cross sections for cells at each apoptosis stage can be approximated using Eqs. (3.27), (3.28) and (3.29). To further simply the problem, we assume that the cross sections of early and late apoptotic cells are comparable and combined into one set of apoptotic cells, and the three equations can then be written as follows

$$\mu_a(D_i,\tau_j,\lambda_k) = \rho_v(D_i,\tau_j)\sigma_{av}(\lambda_k) + \rho_A(D_i,\tau_j)\sigma_{aA}(\lambda_k) + \rho_{Dc}(D_i,\tau_j)\sigma_{aDc}(\lambda_k) \tag{3.30}$$

$$\mu_s(D_i,\tau_j,\lambda_k) = \rho_v(D_i,\tau_j)\sigma_{sv}(\lambda_k) + \rho_A(D_i,\tau_j)\sigma_{sA}(\lambda_k) + \rho_{Dc}(D_i,\tau_j)\sigma_{sDc}(\lambda_k) \tag{3.31}$$

$$g(D_i,\tau_j,\lambda_k) = \rho_v(D_i,\tau_j)g_v(\lambda_k) + \rho_A(D_i,\tau_j)g_A(\lambda_k) + \rho_{Dc}(D_i,\tau_j)g_{Dc}(\lambda_k) \tag{3.32}$$

where $D_i$ is drug dose with i=0,1, 2, 3 representing dose of 0, 4, 8, 16 μM and $\tau_j$ is post treatment time with j=1, 2,3 representing time of 24, 48 and 72 hours and $\lambda_k$ with k=1, 2.., 28 for $460 \leqslant \lambda_k \leqslant 1000$. At each wavelength, the above 3 equations can be rewritten as follows

$$\mu_a(D_i,\tau_j) = \rho_v(D_i,\tau_j)\sigma_{av} + \rho_A(D_i,\tau_j)\sigma_{aA} + \rho_{Dc}(D_i,\tau_j)\sigma_{aDc} \tag{3.33}$$

$$\mu_s(D_i,\tau_j) = \rho_v(D_i,\tau_j)\sigma_{sv} + \rho_A(D_i,\tau_j)\sigma_{sA} + \rho_{Dc}(D_i,\tau_j)\sigma_{sDc} \tag{3.34}$$

$$g(D_i,\tau_j) = \rho_v(D_i,\tau_j)g_v + \rho_A(D_i,\tau_j)g_A + \rho_{Dc}(D_i,\tau_j)g_{Dc} \tag{3.35}$$

The Eq. (3.33) on $\mu_a$ can be written separately as 9 equations for different combinations of $D_i$ and $\tau_j$ as given below

$$\mu_a(D_1,\tau_1) = \rho_v(D_1,\tau_1)\sigma_{av} + \rho_A(D_1,\tau_1)\sigma_{aA} + \rho_{Dc}(D_1,\tau_1)\sigma_{aDc} \tag{3.36}$$

$$\mu_a(D_1,\tau_2) = \rho_v(D_1,\tau_2)\sigma_{av} + \rho_A(D_1,\tau_2)\sigma_{aA} + \rho_{Dc}(D_1,\tau_2)\sigma_{aDc} \tag{3.37}$$

$$\mu_a(D_1,\tau_3) = \rho_v(D_1,\tau_3)\sigma_{av} + \rho_A(D_1,\tau_3)\sigma_{aA} + \rho_{Dc}(D_1,\tau_3)\sigma_{aDc} \tag{3.38}$$

$$\mu_a(D_2,\tau_1) = \rho_v(D_2,\tau_1)\sigma_{av} + \rho_A(D_2,\tau_1)\sigma_{aA} + \rho_{Dc}(D_2,\tau_1)\sigma_{aDc} \tag{3.39}$$

$$\mu_a(D_2,\tau_2) = \rho_v(D_2,\tau_2)\sigma_{av} + \rho_A(D_2,\tau_2)\sigma_{aA} + \rho_{Dc}(D_2,\tau_2)\sigma_{aDc} \tag{3.40}$$

$$\mu_a(D_2,\tau_3) = \rho_v(D_2,\tau_3)\sigma_{av} + \rho_A(D_2,\tau_3)\sigma_{aA} + \rho_{Dc}(D_2,\tau_3)\sigma_{aDc} \tag{3.41}$$

$$\mu_a(D_3,\tau_1) = \rho_v(D_3,\tau_1)\sigma_{av} + \rho_A(D_3,\tau_1)\sigma_{aA} + \rho_{Dc}(D_3,\tau_1)\sigma_{aDc} \tag{3.42}$$

$$\mu_a(D_3,\tau_2) = \rho_v(D_3,\tau_2)\sigma_{av} + \rho_A(D_3,\tau_2)\sigma_{aA} + \rho_{Dc}(D_3,\tau_2)\sigma_{aDc} \tag{3.43}$$

$$\mu_a(D_3,\tau_3) = \rho_v(D_3,\tau_3)\sigma_{av} + \rho_A(D_3,\tau_3)\sigma_{aA} + \rho_{Dc}(D_3,\tau_3)\sigma_{aDc} \tag{3.44}$$

Similarly, the Eq. (3.34) on $\mu_s$ and Eq. (3.35) on g can be written likewise to become 9 equations for each cell set. Because the experiment was performed at 28 different wavelengths, we end up forming 252 total equations of $\mu_a$ for all wavelengths, and various combination of D and $\tau$ or 756 total equations inclusive of $\mu_s$ and g. These equations can be treated as a system of linear equations and expressed in matrix form at each $\lambda$ as

$$\begin{bmatrix} \mu_a(D_1,\tau_1) \\ \mu_a(D_1,\tau_2) \\ \mu_a(D_1,\tau_3) \end{bmatrix} = \begin{bmatrix} \rho_v(D_1,\tau_1) & \rho_A(D_1,\tau_1) & \rho_D(D_1,\tau_1) \\ \rho_v(D_1,\tau_2) & \rho_A(D_1,\tau_2) & \rho_D(D_1,\tau_2) \\ \rho_v(D_1,\tau_3) & \rho_A(D_1,\tau_3) & \rho_D(D_1,\tau_3) \end{bmatrix} \begin{bmatrix} \sigma_{av} \\ \sigma_{aA} \\ \sigma_{aDc} \end{bmatrix} \tag{3.45}$$

$$\begin{bmatrix} \mu_a(D_{2,}\tau_1) \\ \mu_a(D_{2,}\tau_2) \\ \mu_a(D_{2,}\tau_3) \end{bmatrix} = \begin{bmatrix} \rho_v(D_{2,}\tau_1) & \rho_A(D_{2,},\tau_1) & \rho_D(D_{2,}\tau_1) \\ \rho_v(D_{2,}\tau_2) & \rho_A(D_{2,}\tau_2) & \rho_D(D_{2,}\tau_2) \\ \rho_v(D_{2,}\tau_3) & \rho_A(D_{2,}\tau_3) & \rho_D(D_{2,}\tau_3) \end{bmatrix} \begin{bmatrix} \sigma_{av} \\ \sigma_{aA} \\ \sigma_{aDc} \end{bmatrix} \tag{3.46}$$

$$\begin{bmatrix} \mu_a(D_{3,}\tau_1) \\ \mu_a(D_{3,}\tau_2) \\ \mu_a(D_{3,}\tau_3) \end{bmatrix} = \begin{bmatrix} \rho_v(D_{3,}\tau_1) & \rho_A(D_{3,},\tau_1) & \rho_D(D_{3,}\tau_1) \\ \rho_v(D_{3,}\tau_2) & \rho_A(D_{3,}\tau_2) & \rho_D(D_{3,}\tau_2) \\ \rho_v(D_{3,}\tau_3) & \rho_A(D_{3,}\tau_3) & \rho_D(D_{3,},\tau_3) \end{bmatrix} \begin{bmatrix} \sigma_{av} \\ \sigma_{aA} \\ \sigma_{aDc} \end{bmatrix} \tag{3.47}$$

Eqs.(3.34) and (3.35) for $\mu_s$ and g can similarly be written in the above three matrix forms.

For each sample with the same treatment dose D and post-treatment time $\tau$, the total number of cells and the proportion of cells in a sample at each apoptosis stage is the same. In addition, the $\sigma_{aL}$, $\sigma_{sL}$ and $g_L$ for various cell type are the same at each wavelength where L= 1, 2,3 representing sets of viable, apoptotic cells and debris. In that case, we can form a system of 9 equations with 9 unknown variables using measured data from the same wavelength. Using this approach, the proportion of each cell type in the sample for different dose and $\tau$ can be obtained and compared with those obtained by MTT and fluorescent flow cytometry methods to validate this new spectrophotometric method in detection of apoptosis.

# CHAPTER 4 Experimental methods

In order to obtain the optical parameters of a turbid sample accurately, based on the RT theory, an experimental system has to be developed, calibrated and then validated against well established samples and models. In this chapter, we describe the experimental methods used in this dissertation study. A multiparameter spectrophotometric system has been constructed and validated for acquisition of three light signals in steps of 20 nm from 460 to 1000 nm in wavelength without integrating sphere. The optical parameters of different microsphere suspensions were inversely determined using the iMC code discussed in Chapter 3 and compared to the results of Mie theory for system validation.

## 4.1 System design and construction

The multiparameter spectrophotometer system consists of light source unit, monochromater and sample chamber as shown in Figs. 4-1 and 4-3 below. The light source unit contains a tunable xenon light source of 175 W (WavMed Technologies Corp, XL1-175-A) to produce a continuous-wave light beam of broad spectrum ranging from 300 nm to 2500 nm. The beam is collimated and focused by a set of spherical and plane mirrors to the entrance slit of an in-house built monochromator of Czerny-Turner design. The light source also includes a mechanical light chopper (SRS, SR540) placed in front of the input slit of the monochromator to modulate the light beam at a frequency $f_0$~390 Hz. A diffraction grating of 1200 grooves/mm (Thorlabs, GR1205) is used to disperse the incident beam for selection of a monochromatic beam with wavelengths tunable from 460 nm to 1000 nm by the output slit, which has an output half-maximum bandwidth of about 4.5 nm. The wavelengths are tuned by rotating the diffraction grating manually using a rotation stage. A long pass filter with a cut-on wavelength of 500 nm is used to block light of high

diffraction order with shorter wavelengths that may be present in the output beam from the monochromator for light of wavelengths greater than 800 nm. A spectrometer (Ocean Optics, USB4000A) was used to measure the center wavelength as well as the full-width-half-maximum (FWHM) width of the output beam from the monochromator. The schematic of the experimental system is as shown below.

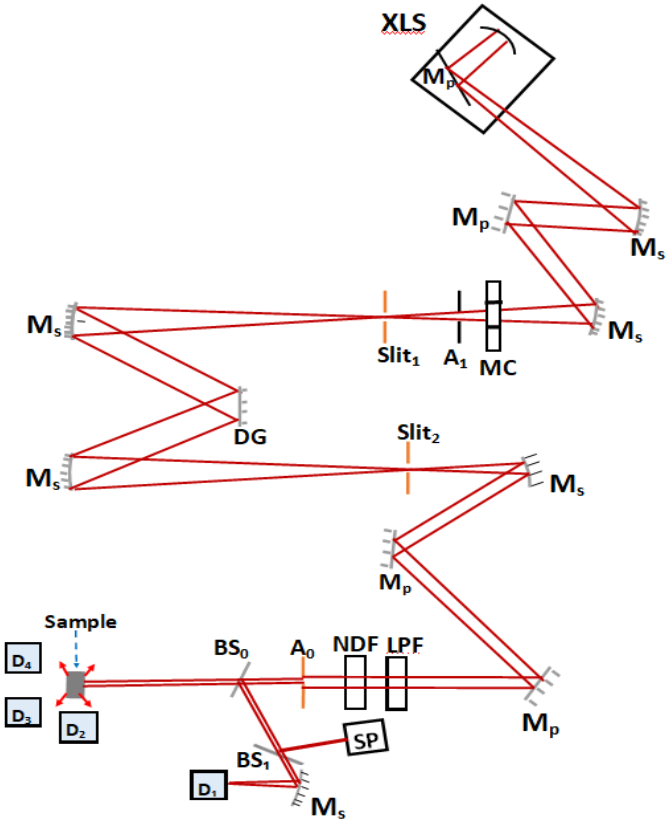


Fig. 4-1. Schematic of spectrophotometric experimental system (Top view). XLS: xenon light source; $M_p$: plane mirrors; $M_s$: spherical mirrors; $A_0$ & $A_1$, apertures; MC: mechanical chopper; DG: diffraction grating; LPF: long-pass filter; NDF: neutral density filter; SP: spectrometer; $BS_0$ & $BS_1$: beam splitters; and $D_1$, $D_2$, $D_3$ & $D_4$ photodetectors.

By using the spherical mirror $M_5$ as a collimating mirror, the divergence of the output beam was minimized to 1.3$^o$ and 0.21$^o$ half-angles along the major and minor axis of the beam profile

The size of the beam incident at the sample could be adjusted with an iris placed underneath the sample order along the beam path to be within the sample size. In this system, the beam was shaped into cylindrical profile with major and minor diameters of 10.4 mm and 4.2 mm respectively as shown below.

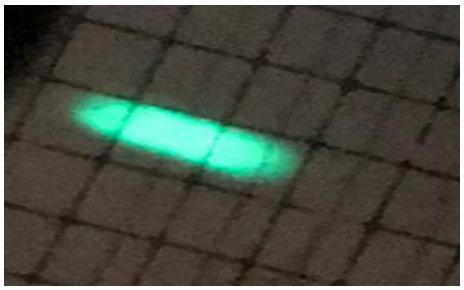

Fig. 4-2. Beam profile at the sample plane

A sample consisting of turbid liquid sandwiched between two glasses within a ring-shaped spacer and the sample assembly is placed horizontally against the incidence beam as shown in Fig. 4-3 above. Also shown in the figure are three photodiodes (Thorlabs, FDS 100) labelled as $D_2$, $D_3$ and $D_4$ which were used to measure the diffusely scattered light intensities from the sample. All four photodiodes have the same sensor area of 3.6 x 3.6 ($mm^2$). A fourth detector $D_1$ measured a fraction of the incidence beam diverted using beam splitter ($BS_0$). A lock-in board (LIB) was developed and used to amplify and demodulate the signals from the photodiodes before digitization and transmission a controlling computer as decribed in the next section.

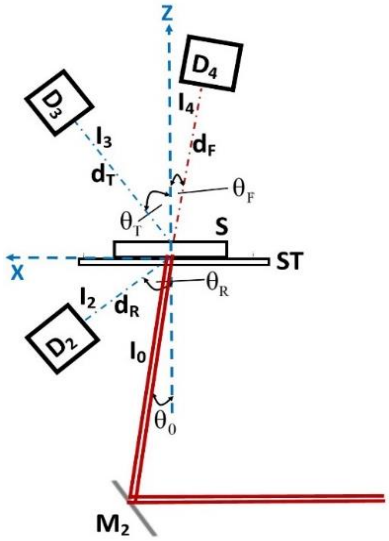


Fig. 4-3. Schematic (side view) of sample-detector configuration. ST: sample stage; S: sample; $D_2$, $D_3$ & $D_4$: photodiodes; $d_R$, $d_T$ and $d_F$ respective distances from sample to photodiode; $\theta_R$, $\theta_T$ and $\theta_F$: respective photodetectors orientation.

## 4.2 Detection of scattered light signals

The flow chart of the spectrophotometer experimental system used to detect light signals from a turbid sample is as shown below.

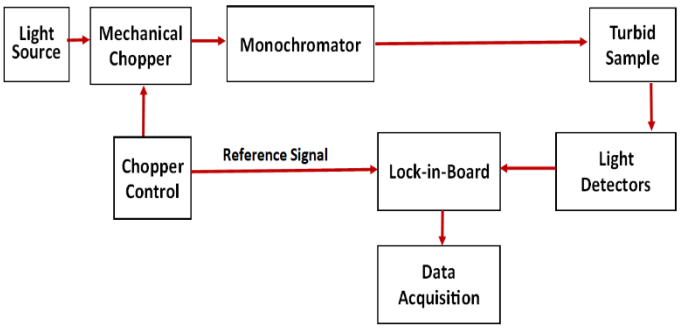


Fig. 4-4. Flow chart of light modulation, signal detection, amplification, and acquisition.

The light signals of interest include the one incidence to the turbid sample as monitored by the incidence light detector and those scattered from the sample measured by the diffuse light detectors shown in Fig. 4-3. The light intensity received by each of the photodetectors is measured in terms of voltage using a lock-in-board LIB. The LIB uses a phase-sensitive detection technique which measures signals at a specific reference frequency and phase [84] . The frequency is set using the chopper control. This lock-in amplification technique makes it possible to measure very weak light signals in the presence of strong ambient light signals. The LIB has four channels of to amplify and demodulate the electric signal from each of the four detectors. The photocurrent $I_p$ from each photodiode is proportional to the light irradiance I incident on its sensor area $A_s$ and written as:

$$I_p = I \times A_s \times R \tag{4.1}$$

where R is the responsivity of the photodiode.

Supplying the photodiode with a reverse bias voltage increases the depth of the depletion region of the photodiode's PN junction and thus reduces the junction capacitance. This improves the speed of response and linearity of the photodiode. All photodiodes were supplied with 5V reverse bias voltage. Since each LIB channel consists of one impedance R amplification stage and two voltage amplification stages, $G_1$ and $G_2$, output voltage $V_{out}$ of each channel is computed as:

$$V_{out} = I_p R G_1 G_2 \tag{4.2}$$

where $G_1$ and $G_2$ are the voltage gains. A computer program is set to read the output voltage from each LIB channel by acquiring 160 readings and averaging them. Averaging such many readings ensures that any noise signal fluctuation is filtered out. The light irradiance I incident to photodiode $D_i$ is proportional to channel i output voltage $V_i$ of the LIB as follows:

$$V_i - V_{bi} = f_i I + \beta_i \tag{4.3}$$

where b in the subscript is the ambient light contribution, β electronic noise bias, $f_i$ is channel gain-sensitivity factor, and i=1, 2, 3, 4 is the index for channel and detector number.

As described in Eq. (4.3), the measured voltage signals will have a component of ambient light and electronic noise signals. These signals are known to reduce the sensitivity of measured signals by decreasing the signal-to-noise ratio and hence the need to either eliminate them or accurately account them in the signal measurements. To minimize the ambient or unaccounted sample scattered light signals from reaching the photodetectors, we designed a black plastic cylindrical hollow tube to enclose each photodiode as shown in Fig. 4.5. This tube limits the field-of-view of the photodiode's sensor only to the surface of the sample and prevents any light scattered from reflecting surfaces from reaching it. Because the field of view of the photodetector's sensor is limited due to the tube length L in front of it, we calculated the minimum distance between the tube's end and the sample surface $L_3$ as shown in these two steps:

$$\tan(\theta) = \frac{(d_2 - d_1)}{2L_1} = \frac{(d - d_1)}{2L} \tag{4.4}$$

where $d_1$, sensor width; $L_1$, sample-sensor distance; $L_2$, sensor glass window thickness; d, tube internal diameter; $L_3$, sample-tube end distance; $d_2$, sample diameter and θ, sensor angle of view. Eq. (4.6) can be rearranged to $L_1$ and hence $L_3$ as defined in Fig. 4-5 to become:

$$L_3 = L_1 - L = \frac{(d_2 - d_1)}{(d - d_1)} L - L_2 \tag{4.5}$$

To control the electronic noise bias of the LIB, the four photodiodes were connected to their respective channels in the LIB and their tube entrance blocked. The output bias of each of the channel was then adjusted so that each channel output voltage was zero. The ambient light signal to $D_2$, $D_3$ and $D_4$ was measured by placing a water sample on sample stage then a dark shield placed in front of $D_4$ using a string to block the incident light from entering it as shown in Fig. 4-6.

Blocking $D_4$ also serves to prevent back reflection from $D_4$ sensor window to the water sample. Lastly, to measure the contribution of ambient light to $D_1$, beam was also blocked between $BS_1$ and $M_1$ on the set up shown on Fig. 4-1. The ambient light signals for each wavelength from the four photodetectors are then measured and recorded as $V_{1b}$, $V_{2b}$, $V_{3b}$ and $V_{4b}$ respectively.

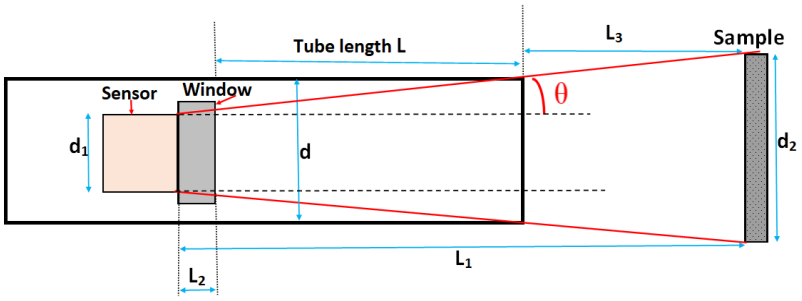


Fig. 4-5. Schematic for photodetector shielding tube length calculation parameters. $d_1$, sensor width; $L_1$, sample-sensor distance; $L_2$, sensor glass window thickness; d, tube internal diameter; $L_3$, sample-tube end distance; $d_2$, sample diameter; θ, sensor angle of view.

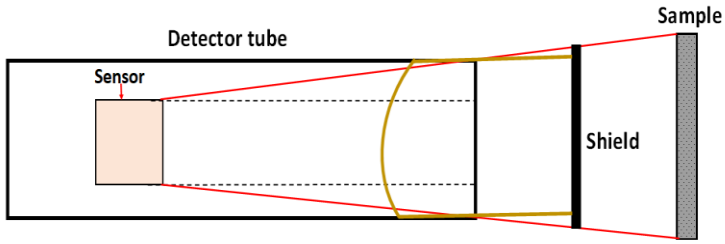


Fig. 4-6. Schematic set-up for light shield held in front of $D_4$ using a string during ambient light signals measurement.

## 4.3 Calibration of the experimental system

The main system calibration involves the determination of the light power incident to the sample surface in relation to that measured by the monitoring detector $D_1$. As earlier described, the monochromatic light incident to the sample is nearly collimated and of cylindrical shape. An aperture $A_0$ is used to control the beam size at the sample stage as shown in Fig. 4-7. A beam

splitter $BS_0$ diverts a fraction of the incident light travelling along the x-axis to detector $D_1$ for monitoring while beam splitter $BS_1$ provides the light needed for wavelength measurements by spectrometer sp. Mirror $M_2$ as shown in Fig. 4-3 is used to reflect the incident beam upward at an angle of θ from the z-axis to the center of sample holder placed on sample stage. A calibration factor c which is defined as the ratio of light power incident to the sample stage to that measured by detector $D_1$ is then determined. To obtain this factor, a calibrated BK7 lens of focal length f=50 mm and diameter $d_L$=25 mm is placed on sample stage to focus the entire incident beam to the surface of detector $D_4$. At each wavelength λ of interest, the light signals from $D_1$ and $D_4$ detectors are simultaneously measured using channel 1 and 4 of the LIB as $V_1$ and $V_4$ respectively. To prevent saturation of $D_4$ during the c-calibration measurements, appropriate Neutral Density Filters NDF was used to reduce the beam intensity. The c-factor is then calculated as

$$c = \frac{I_0 - I_{0b}}{I_1 - I_{1b}} = \frac{I_4 - I_{4b}}{T_r(I_1 - I_{1b})} = \frac{(V_4 - V_{4b})}{T_r G_4 S_4} / \frac{(V_1 - V_{1b})}{G_1 S_1} = \frac{G_{14} S_{14}(V_4 - V_{4b})}{T_r(V_1 - V_{1b})} \tag{4.6}$$

where $G_{14}=G_1/G_4$ is channel gain ratios, $S_{14}=S_1/S_4$ is detector sensitivity ratios, and $T_r$ = transmittance of the lens placed before $D_4$. Due to specular reflectance $I_R$ of the light incident to $D_4$ by its glass window (Borosilicate glass) during the measurements, $V_4$ voltage signal need to be corrected for this loss using the Borosilicate glass transmittance $T_{D4}$. Eq. (4.6) can thus be simplified as

$$c = \frac{G_{14} S_{14}(V_4 - V_{4b})}{T_{D4} T_r(V_1 - V_{1b})} \tag{4.7}$$

This equation can be rewritten as

$$c = \frac{f_{14}(V_4 - V_{4b})}{T_{D4} T_r(V_1 - V_{1b})} \tag{4.8}$$

where $f_{14}$ is a relative gain-sensitivity parameter between $D_1$, Ch.1 and $D_4$, Ch.2 which will be described later in this chapter. This calibration factor c measured at each wavelength can then be used to calculate the incident light power to the sample surface in relation to the power measured by detector $D_1$ while performing sample light signal measurements.

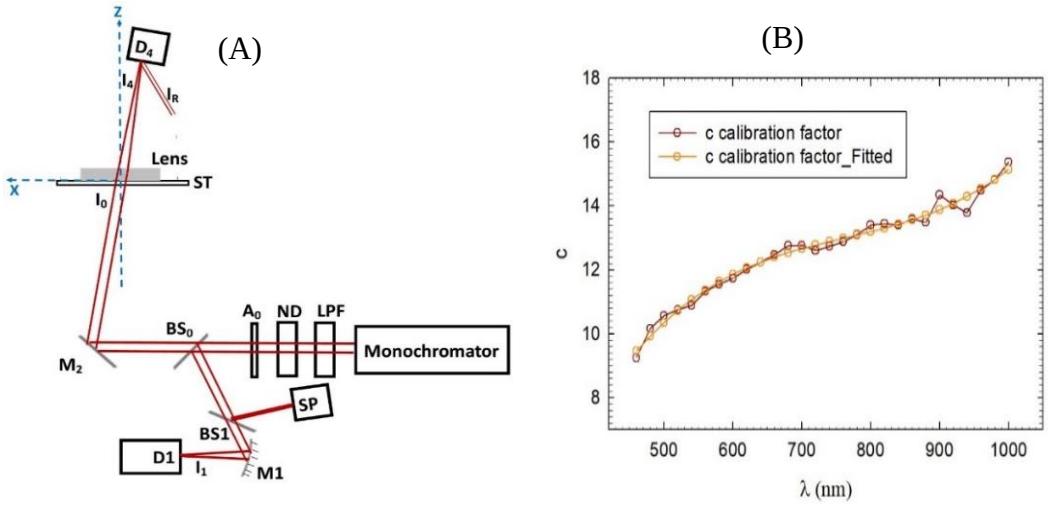


Fig. 4-7. (A) Schematic of spectrophotometer experimental system for c-calibration factor measurements. $I_R$, specular reflection from photodiode glass window. (B) c-calibration results. The fitted values are the measured c calibration results smoothened for minor fluctuations using cubic polynomial data fitting.

The LIB used in this study was manufactured by our collaborator and unlike other standard lock-in amplifiers from established vendors, this LIB had to be first accurately calibrated in our laboratory before its use. The LIB channel gain-sensitivity factor $f_i$ is always a product of channel i gain Gi and sensitivity $S_i$ of the connected photodiode and thus we define $f_i$ so that the light irradiance $I_i$ incident on a photodiode i can be linearly related to the output voltage $V_i$ of LIB channel i as follow:

$$V_i - V_{ib} = G_i S_i (I_i - I_{ib}) = f_i (I_i - I_{ib}) \tag{4.9}$$

or

$$I_i - I_{ib} = \frac{V_i - V_{ib}}{f_i} \tag{4.10}$$

To calibrate the LIB channels, the sensitivity-gain factor of detector $D_1$ connected to Ch.1 is calibrated against those of $D_2$ connected to Ch.$_2$, $D_3$ connected to Ch.3, and $D_4$ connected to Ch.4. To accomplish this, the same light intensity is measured using different combinations of gain settings between channel 1 as $V_1$ and the rest of the channels $V_i$. Calibrated neutral density filters NDF are used where necessary to reduce the light intensity and prevent LIB saturation. To minimize calibration measurements errors, all four detectors are identical with sensor area of 3 mm x 3 mm to ensure same beam area on the surface of each. For simplification, we can define the parameter $f_{1i}$ as the ratio of channel 1 sensitivity-gain factor $f_1$ to that of channel 2, 3 and 4 $f_i$ as follows:

$$f_{1i} = \frac{f_1}{f_i} = \frac{S_1 G_1}{S_i G_i} = \frac{V_1 - V_{1b}}{V_i - V_{ib}} \tag{4.11}$$

To test if the photocurrent response of the photodetectors connected to their corresponding LIB channels are linear, we performed the linearity test and results compared to those measured by a vendor calibrated lock-in amplifier LIA (SR 830). To achieve this, one photodetector is placed in $D_4$ position and neutral density filters of known transmittance used to control the incident light intensity as shown in Fig. 4-3 with no sample placed on sample holder. The four channels of the LIB are adjusted to have the same input gain and then each supplied with the same photocurrent from photodiode, one channel at a time and their corresponding output voltages recorded for each light intensity. LIA was then used to measure the voltage corresponding to the same photocurrents. From the results shown in Fig. 4-8 below, it is observed that the measured signals by LIB vary linearly with incident light intensity for output voltages less than 1.5 V as compared to the same

signals measured by LIA. It is also observed that the signal measured by channel 4 fails linearity tests for voltage signals less than 50 mV. Based on these findings, we adjusted the LIB gain settings and used the appropriate neutral density filters during sample data measurements to ensure the measured voltage $V_m$ signals are always in the range $50 \leq V_m \leq 1500$ mV.

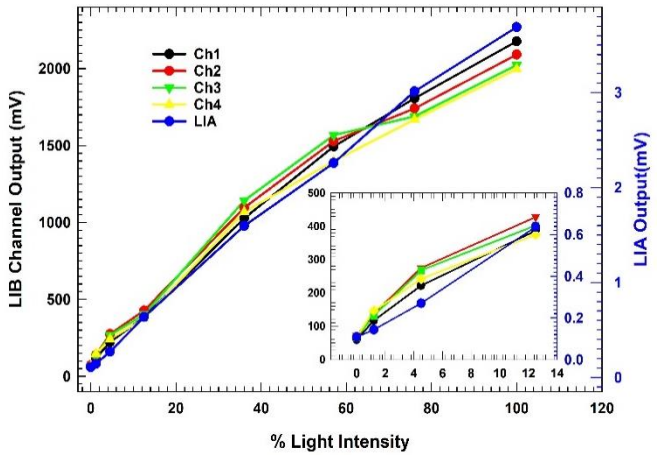


Fig. 4-8. LIB linearity test. Chi-Vi is channel i output voltage Vi; LIA is lock-in amplifier output voltage. Inset is the part of graph close to zero.

A xenon light lamp is preferred as the light source because on top of producing spectral energy distribution mimicking that of natural daylight, and its radiant intensity is much higher compared to that of incandescent sources [85] . However, it is reported that the lamp light output may fluctuate slightly based on the stability of the xenon arc. We thus tried to establish the extend of light fluctuation of the xenon lamp because large fluctuations could lead to significant variation of measured signals especially while performing repeat measurements. This could happen if the spectrophotometric optics do not respond linearly to sudden beam intensity variation. Photodetectors $D_1$ and $D_4$ were placed in respective positions in the spectrophotometer as shown in Fig. 4-1. The xenon light source was turned on and given enough time of approximately 5 mins to warm up and settle. Then afterwards, the light intensity was monitored

using the 2 photodetectors by collecting readings simultaneously every 15s for 5 minutes. From the results shown in Fig. 4-9 below, we can observe that despite presence of non-simultaneous fluctuation of the light intensities monitored by $D_1$ and $D_4$, their magnitudes are insignificant. Statistical analysis of the results gives relative standard deviations of 1.8 % and 0.5 % from the mean values for light intensities monitored respectively by $D_1$ and $D_4$.

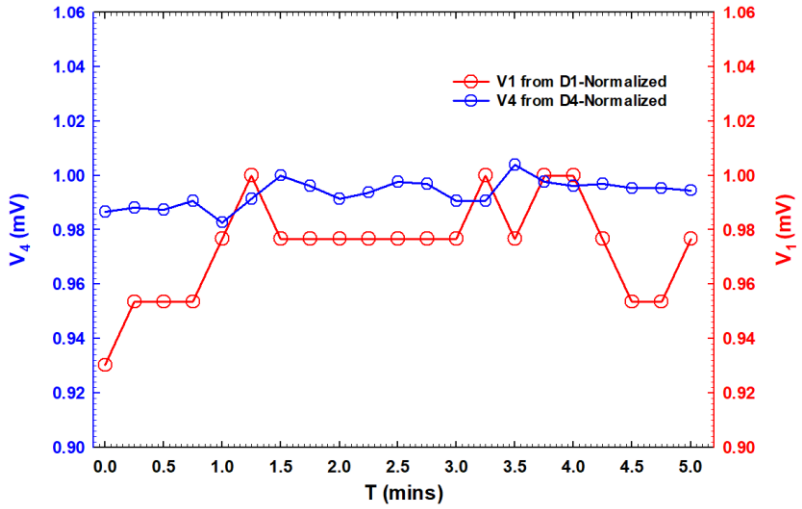


Fig. 4-9. Measurement of xenon light source output fluctuation as monitored simultaneously by photodiodes $D_1$ (as $V_4$) and $D_4$ (as $V_1$) for total time T of 5 mins. Each measurement was acquired with integration time of 10 s.

## 4.4 Microsphere sample preparation and measurements

### 4.4.1 Turbid sample preparation

Multiple spherical suspension samples were used for this study to validate the experimental system. The thickness d of a suspension sample is defined by that of the ring-shaped spacer with desired thickness. Two microscope glass slides of 1 mm thickness were used as the bottom (front facing the incident beam) and the top (back) holders to sandwich the sample as shown in Fig. 4-10 (B) below. A thin film of vaseline jelly is applied on each surface of the shim to bind the glass

covers to the shim. The volume created by the shim and the 2 covers is carefully filled with the suspension liquid and the 2 covers gently pressed against the shim to seal the suspension making sure no bubbles are formed. To determine the actual thickness of the suspension, the thicknesses of the glass covers were first measured using micrometer screw gauge before sample is assembled and then the total thickness of the shim and 2 glass covers measured after sample assembly. The thickness of the turbid suspension was calculated as the difference of the assembly thickness to that of both cover glasses. The sample assembly is then mounted on a sample holder which gently presses together the 2 glasses together to sealing it. The sample holder is then placed on the sample stage as shown in Fig. 4-3 for spectroscopic measurements.

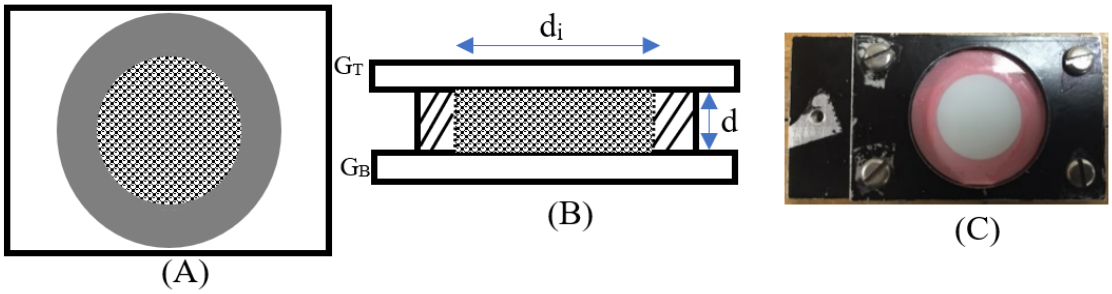


Fig. 4-10. Top view (A) and side view (B) schematic of the turbid sample holder. (C) Top view of the actual sample assembly containing microspheres suspension. The pink ring has inner diameter $d_i$ of 14.3 mm and thickness $d$ of 2.1 mm. $G_T$ and $G_B$ are top and bottom glass covers of thickness ~1 mm.

In this study, we used two samples of polystyrene microsphere suspensions of different sample thickness d and different nominal sphere diameters $d_s$ with coefficients of variation CV. The first sample was of d=0.91±0.01 mm, $d_s$=0.966 μm and concentration $\rho=(5.37\pm0.02)\times10^6$ mm$^{-3}$. The second sample was of d=2.10±0.01 mm, $d_s$ =11 μm and concentration $\rho=(3.05\pm0.02)\times10^4$ mm$^{-3}$. To determine the actual concentration of the microspheres reported above, we used the evaporation method as reported elsewhere [86] and used the protocol described in appendix A. To summarize this method, we used polystyrene microspheres (5095B, Duke Scientific Corporation, USA) of $d_s$

=0.966 μm and nominal concentration of 10% by weight suspended in deionized water. The stock solution nominal number density was calculated to be 2.008 x $10^8$ $mm^{-3}$. This solution was diluted with deionized water to obtain a microspheres suspension with nominal density of 5.05 x$10^6$ $mm^{-3}$. A 10 mL aliquot of this diluted microspheres suspension was weighed by an electronic balance with weighing accuracy of 0.1 mg. The flask containing the suspension was heated to a temperature of 60°C and the water completely evaporated to obtain dry microspheres and the mass re-measured. From the microspheres total mass $m_t$=0.0535 g, microspheres mass density $\rho$=1.055 $g/cm^3$, single microsphere volume v=4.720 x $10^{-13}cm^3$, and suspension volume $v_t$=10 mL, the measured number concentration was found to be 1.074 x $10^7$ $mm^{-3}$. The measured mass concentration was found to be higher (almost twice) than the nominal one and this can be attributed to water evaporation from the stock solution after a shelf life of about 18 years. The new suspension was diluted two-fold with deionized water to obtain a suspension of concentration c=5.369 x $10^6$ $mm^{-3}$. The same procedure was followed to obtain the actual concentration of the $d_s$ =11 μm suspensions reported at the beginning of this section. Note that both suspensions were diluted appropriately to make samples of lower turbidity to prevent nearly total attenuation of the incident beam by the sample which could significantly reduce signal-to-noise ratio especially for detectors $D_3$ and $D_4$.

In addition, we decided to determine the size distribution of the microspheres in each sample, using a software to measure the diameters of microsphere suspensions as described elsewhere [5]. The results are as shown in Fig. 4-11 below. In summary, the measured range of microsphere diameters were found to be $d_{11}$=11.5±1.0 μm and $d_{0.966}$=0.966±0.04 μm. It should be noted that there is a presence of lumps consisting of fused microspheres in the microscopy images of two samples. This range of measured microsphere diameters should be considered

while simulating the optical properties using the Mie code because the modelled parameters are sensitive to sizes of the scattering particles. The effect of the presence of aggregated microspheres in the samples on the measured optical signals should also be considered while comparing with those experimentally obtained because Mie simulation assumes the particles are of uniform single spheres.

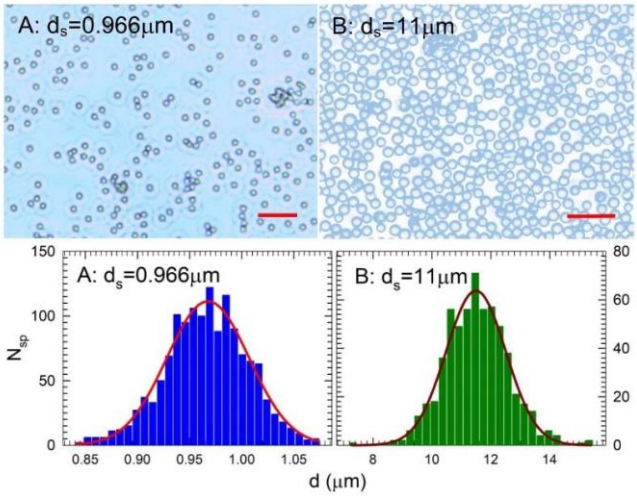


Fig. 4-11. Microscopy images and size distributions of the microspheres samples, with the bar=10 μm for sample A and bar=50 μm for B. Here $N_{sp}$ is the number of spheres, $d_s$ is the diameter of spheres of the corresponding samples. The solid lines on histograms are Gaussian distributions curves. Adapted from[1] .

### 4.4.2 Diffuse light signals measurement and calculation

To obtain the optical parameters of a turbid sample, measured signals are first calculated from the scattered light signals and then an inverse algorithm used to simulate the optical properties from the measured signals. To measure the light scattered signals, a turbid sample is prepared as described in Sub-section 4.4.1 and then placed on the sample stage. Four photodiodes are used to measure four light signals which include: (i) Incidence light intensity $I_0$ to the sample holder measured by detector $D_1$ as $V_{1s}$, (ii) Diffusely reflected light intensity $I_2$ from the turbid sample measured by detector $D_2$ as $V_{2s}$, (iii) Diffusely transmitted light $I_3$ from the turbid sample measured

by detector $D_3$ as $V_{3s}$, and (iv) Forwardly scattered light $I_4$ from the turbid sample measured by detector $D_4$ as $V_{4s}$. The ratios of incidence light intensity $I_0$ to each of the 3 light intensities define the measured signals of diffuse reflectance $R_d$, diffuse transmittance $T_d$ and forward transmittance $T_f$ as follows:

$$R_d = \frac{I_2 - I_{2b}}{I_0 - I_{0b}} = \frac{I_2 - I_{2b}}{c(I_1 - I_{1b})} \tag{4.12}$$

$$T_d = \frac{I_3 - I_{3b}}{I_0 - I_{0b}} = \frac{I_3 - I_{3b}}{c(I_1 - I_{1b})} \tag{4.13}$$

$$T_f = \frac{I_4 - I_{4b}}{I_0 - I_{0b}} = \frac{I_4 - I_{4b}}{c(I_1 - I_{1b})} \tag{4.14}$$

where the calibration factor c relates the light intensity $I_1$ measured by $D_1$ to that incident to the sample holder $I_0$ as described in section 4.3. $I_{xb}$ is the background intensity measured by each photodiode as described in section 4.2. The light intensity incident to each detector is proportional to the output voltage V from the LIB channel corresponding to it as described in Eqs. (4.9) and (4.10). The above equations for $R_d$, $T_d$ and $T_f$ can thus be written as:

$$R_d = \frac{G_{12}S_{12}(V_{2s} - V_{2b})}{c(V_{1s} - V_{1b})} = \frac{f_{12}(V_{2s} - V_{2b})}{c(V_{1s} - V_{1b})} \tag{4.15}$$

$$T_d = \frac{G_{13}S_{13}(V_{3s} - V_{3b})}{c(V_{1s} - V_{1b})} = \frac{f_{13}(V_{3s} - V_{3b})}{c(V_{1s} - V_{1b})} \tag{4.16}$$

$$T_f = \frac{G_{14}S_{14}(V_{4s} - V_{4b})}{c(V_{1s} - V_{1b})} = \frac{f_{14}(V_{4s} - V_{4b})}{c(V_{1s} - V_{1b})} \tag{4.17}$$

### 4.4.3 Microsphere data collection

To validate our new spectrophotometric method, we obtained the optical properties of polystyrene microsphere suspensions for wavelengths λ from 460 nm to 1000 nm in steps of 20 nm and compared with those approximated by Mie theory. We used two samples of polystyrene

microsphere suspensions of different sample thickness *d* and different nominal sphere diameters $d_s$ with coefficients of variation CV prepared as described in in sections 4.4.1.

The distances and orientations of $D_3$ and $D_4$ from the back glass center surface and $D_2$ from the front glass center surface of the sample holder with the z-axis as shown in Fig. 4-3 for two microsphere samples of $d_s$=(0.966 μm, 11 μm) were $d_R$=(31.7 mm, 21.5 mm), $d_T$=(44.1 mm, 35.7 mm), $d_F$=(49.3mm, 88.4 mm) and $\theta_R$=($45^0$, $45^0$), $\theta_T$=($43^0$, $48^0$) and $\theta_F$=($8^0$ , $9^0$ ). The incident beam orientation to the front glass surface normal was $\theta_0=8^0$. The inner diameter of the sample spacer for the 0.966 μm and 11 μm microsphere suspensions were respectively 16.3 mm and 14.3 mm. Measured light signals of $R_d$, $T_d$ and $T_f$ were obtained as described in section 4.4.2 for λ between 460 nm and 1000 nm in steps of 20 nm. The measured signals measurements were repeated three times to obtain mean values and standard deviation for each wavelength as shown in Fig. 4-12 below. This ensures that the results are reproducible. The sample was shaken in between the repeat measurements to ensure homogeneity by preventing settling down of the microsphere suspensions. The microsphere suspensions settling down effect is described later in this chapter.

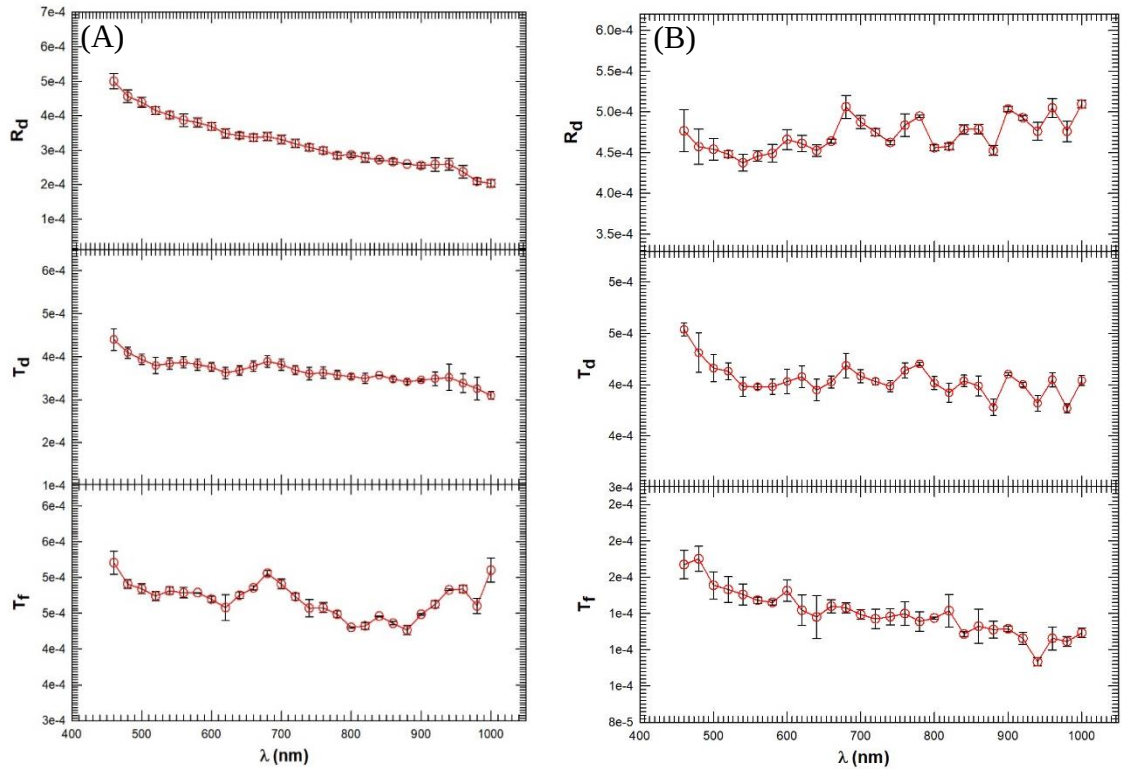


Fig. 4-12 Measured light signals of $R_d(\lambda)$, $T_d(\lambda)$, and $T_f(\lambda)$ from microsphere suspension samples of (A) $d_s$=0.966 μm and (B) $d_s$ =11μm. The symbols represent the mean values and error bars represent the standard deviation of three sets of measured data sets per λ for a sample of thickness d~2.1mm. Adapted from [1].

## 4.5 Inverse determination of optical parameters and validation

The Individual Monte Carlo (iMC) program described in chapter 3 was used to inversely deduct the optical parameters $\mu_a(\lambda)$, $\mu_s(\lambda)$ and $g(\lambda)$ from the measured signals $R_d(\lambda)$, $T_d(\lambda)$, and $T_f(\lambda)$ using the sample-detector configuration shown in Fig. 4-3. The sample parameters and sample-detectors configuration used in this study are the same as those described in Sub-section 4.4.3 for both microsphere samples of $d_s$=0.996 μm and 11 μm. For each wavelength, the iMC code described in chapter 3 was run with the corresponding input values of the measured signals,

refractive index n, photon numbers $N_o$ and the initial optical parameters. The minimum objective delta $\delta_{min}$ chosen for this simulation was 8 x $10^{-3}$ because the three measured signals at each wavelength were estimated to have a relative error of about 5% for this spectrophotometric system set-up. Each simulation was started with $N_0$=5 x $10^6$ for initial simulation search and then increased to $N_0$=5 x $10^7$ once δ started approaching $\delta_{min.}$ As a result of implementing the iMC code on GPU computer, the computing time per wavelength was below 5 mins after the initial optical parameters producing $\delta < \delta_{min}$ were determined.

The δ values were able to converge below $\delta_{min}$ for all wavelengths simulated for both samples with the exception of only three wavelengths for the 11 μm sample as shown in Fig. 4-13(B).

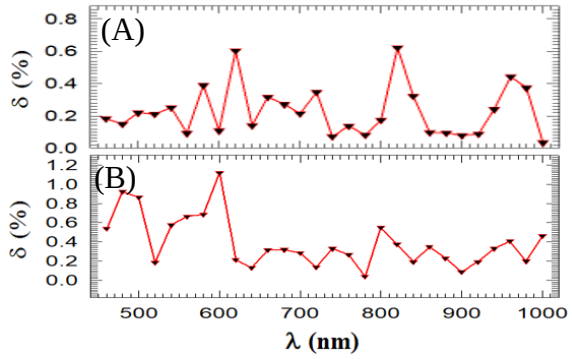


Fig. 4-13. The minimum achieved iMC simulated δ(λ) values for the two microsphere samples (A) $d_s$=0.966 μm and (B) $d_s$=11 μm. Adapted from [1].

To validate the results of our new system, a Matlab code of Mie theory was applied to calculate the optical parameters of the microsphere suspensions for the same wavelengths as the experiment. The Mie theory calculations used the nominal sphere diameters $d_s$ of the two samples and concentrations obtained as per the procedure described in Sub-section 3.2 with the assumption that the samples consist of independent spheres as it relates to light interaction. It should be noted that the Mie Theory results presented in this study for comparison with the iMC simulated results

have already been reported earlier as part of this project [5]. The optical parameters determined by iMC and those predicted by Mie theory for the two samples were plotted against wavelengths as shown in Fig.4-14.

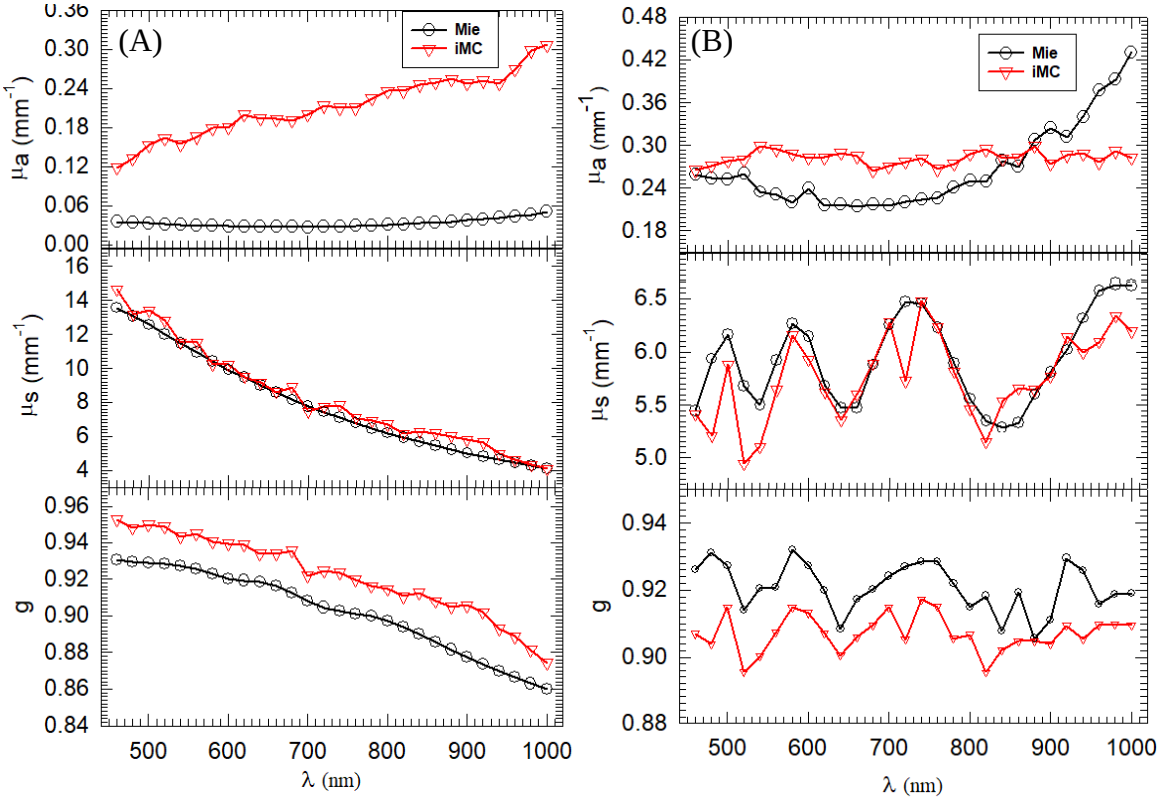


Fig.4-14. Comparison between the optical parameters $\mu_a(\lambda)$, $\mu_s(\lambda)$ and $g(\lambda)$ determined from measured light signals using iMC to those calculated by the Mie theory for samples of microsphere diameters (A) 0.966 μm and (B) 11 μm.

The results have also been described in detail elsewhere [1, 5]. In summary, the results show that the $\mu_s$ and g values inversely obtained from the suspension sample by the iMC code closely matches with those predicted by Mie theory. For the wavelength dependence of the $\mu_s$ and g of 11 μm spheres, the measured signals have an oscillatory pattern and can be closely related to biological cells such as MCF7 cells with d~20 μm which will be studied later on this dissertation. The signal curves of the 0.966 μm microsphere sample on the other hand display a power law

dependence of wavelength like that reported on a previous study of 1 μm microspheres [87]. In particular, in the previous study, it is reported that $\mu_s$ displays a power law dependence of $\mu_s = C.\ \lambda^{-1.507}$ while our results indicate $\mu_s = C.\ \lambda^{-1.515}$ power relationship. The power law relationship is typically for particles with scattering size of $x(\pi d/\lambda) \leq 7$ such as with the case of lipid emulsions like intralipid solution previously studied in our group [19]. As shown, the values as well as the λ dependency of experimental $\mu_s$ and g relatively match those obtained by the Mie theory for both microsphere sizes apart from few wavelengths.

In contrary, there is a significant disagreement between the experimental determined $\mu_a$ to that calculated by Mie theory with the 0.966 μm sphere sample curves showing a significant overestimation while the 11 μm spheres sample indicate a slightly better agreement. This discrepancy may be explained by the way Mie theory results are calculated. For a sphere of given diameter, the Mie theory values of $\mu_s$ and $\mu_a$ are mainly influenced by the real and imaginary parts of the complex refractive index of $n_r(\lambda)$ and $n_i(\lambda)$ respectively. Because the uncertainty in measuring $n_i(\lambda)$ is larger than those of $n_r(\lambda)$, it is expected that the difference in values obtained by the two methods be smaller for $\mu_s$ than that of $\mu_a$. It should also be noted that the 0.966 μm sphere sample has a high average turbidity, with albedo $a = \mu_s/(\mu_s + \mu_a)$ of 0.995 compared to the 11 μm sample which has 0.957, and this might also explain the discrepancy due to the difficultness in extracting the true $\mu_a$ values for the 0.966 μm sample. Lastly, the results for anisotropy factor g show a closely matched λ-dependency behavior between the experimental and Mie theory results but not the values. For the 0.966 μm sphere sample, the experimental g values are overestimated by ~ 2.2% while they are underestimated by ~1.5% for the 11 μm sphere sample. This discrepancy can be explained in two ways. The iMC simulation uses the HG function for the phase function $P_{HG}(\theta)$ given in Eq. (3.21) while the Mie theory employs the scattering matrix element $P_{11}(\theta)$ as

described in Sub-section 3.2. The angular dependences between these two functions is slightly different especially for ~0°, 90°, 180° scattering angles as shown in [5] Fig. 3. Thus, the g values obtained by the two methods are expected to deviate from each other at each wavelength. Another source of discrepancy between the iMC simulated and Mie theory values could be because of the settling effect and the agglomeration of the microsphere suspensions. Mie theory calculations of RT parameters is based on assumptions that the sample consist of independent single spheres of uniform suspensions. For each sample, we performed an experiment to understand the rate of microsphere settling to the bottom of glass sample holder if left undisturbed. A sample of each microsphere size was initially shaken at the beginning and then signals of $R_d$, $T_d$ and $T_f$ measured over 5 mins and 30 mins for 11μm and 0.966μm samples respectively as shown in Fig. 4-15.

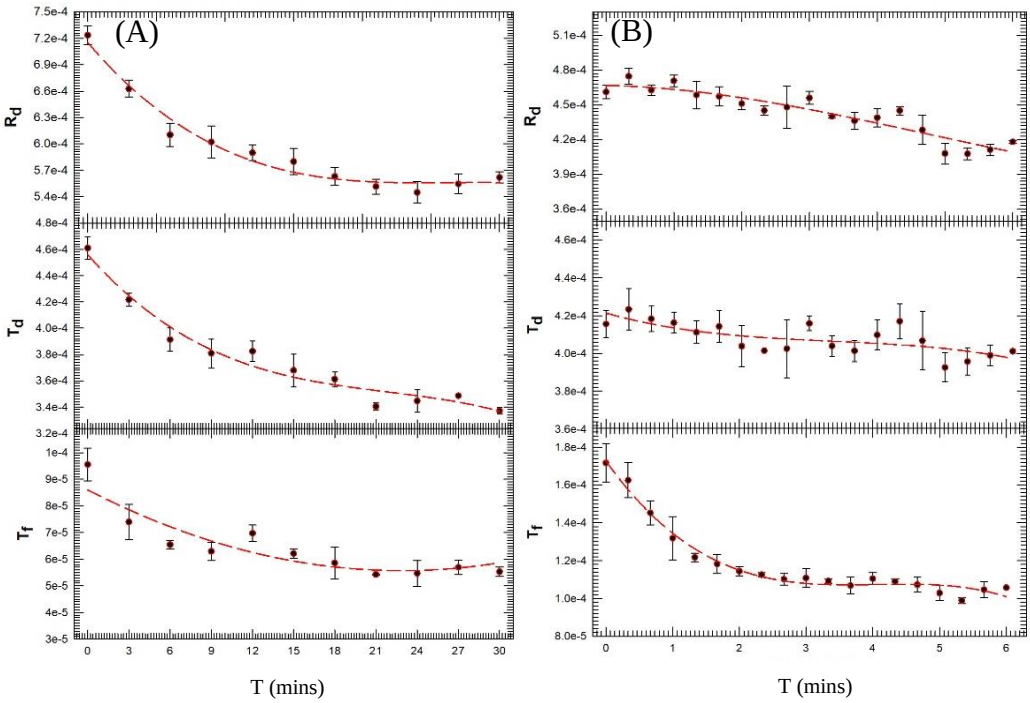


Fig. 4-15. Microsphere suspension settling down effect on measured signals of $R_d(t)$, $T_d(t)$, and $T_f(t)$ for two turbid samples of microsphere diameter (A) 0.966μm and (B) 11μm. Where T is the settling time (t) from when the sample is initially shaken to obtain uniform microsphere suspensions. The symbols and error bars are the mean and std values from three sets of measured signals. The red dashed line is a cubic polynomial data fitting of the measured signals to visualize the trend.

As seen in Fig. 4-15, the settling of the microsphere suspensions to the bottom slide of the turbid sample have a significant effect on the measured signals for both microsphere size samples and hence is expected to have strong impact on the deducted optical parameters. The impact on the measured signals seems to be more significant to the $T_f$ in both samples. For instance, within the first 3 minutes after shaking the sample, the $R_d$, $T_d$ and $T_f$ signals dropped by ~8%, 9% and 10% respectively for the 0.966 μm sample while it dropped by 1%, 10% and 36% for the 11 μm sample. The measurements were taken for large settling time until when the signals stabilized which was 30 and 6 mins for the 0.996 μm and 11 μm samples respectively. By this time, the $R_d$, $T_d$ and $T_f$ signals had dropped by ~22%, 27% and 42% and ~10%, 4% and 39% respectively for the two samples. To minimize this impact during the actual sample measurements, the sample was shaken between each wavelength measurements. However, three measurements were taken at each wavelength repeatedly with a total acquisition time of 30 seconds and according to Fig. 4-15 above, the $T_f$ signals in particular have a significant change within that duration. This might contribute towards the discrepancy between the inverse calculated and Mie theory approximated optical parameters. In addition, as described in subsection 4.4.1, the microscopy images of the 2 samples shows the presence of lumps consisting of fused microspheres. Because these anomalies are not accounted for in the Mie theory model, it can perhaps explain the discrepancy between the RT values obtained by both methods.

As an extra step in validation of this method, we investigated the uniqueness of the iMC inverse solutions for the two samples at select wavelengths. For the selected wavelengths, the objective function δ was calculated after the determination of $\mu_a$, $\mu_s$ and g parameters with $N_0=1 \times 10^8$ photons. A contour plot of δ in the corresponding $\mu_s$-g plane at a given $\mu_a$ was constructed as shown

in Fig. 4-16 below to visualize the delta variation on that plane. In the case of the 0.966 μm sample, comparing the values of δ's corresponding to the $\mu_a$=0.100 $mm^{-1}$ and $\mu_a$=0.166 $mm^{-1}$ in graphs (A) and (B) respectively show that there is a unique δ that exists, which is less than $\delta_{min}$. Similar patterns are observation in the 11μm sample results in graphs (C) and (D). More inverse solution uniqueness validations were also performed and documented elsewhere [88]. We can thus conclude that the inverse results calculated by the iMC simulation in this study are well-posed.

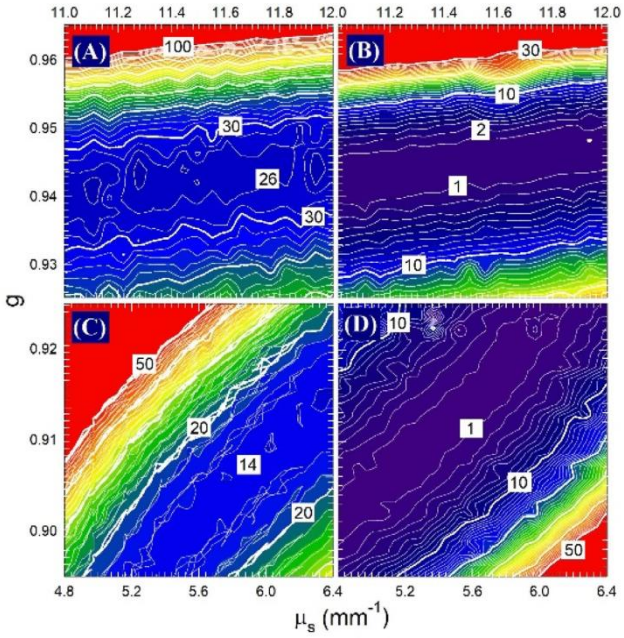


Fig. 4-16. Contour plots of δ(%) in the $\mu_s$-g plane of different $\mu_a$ and minimum value $\delta_m$: (A) $\mu_a$=0.100 $mm^{-1}$, $\delta_m$=24% and (B) $\mu_a$=0.166 $mm^{-1}$, $\delta_m$=0.05% for 0.966μm sample measured at λ=560 nm: (C) $\mu_a$=0.230 $mm^{-1}$, $\delta_m$=13.6% and (D) $\mu_a$=0.289 $mm^{-1}$, $\delta_m$=0.62% for 11 μm sample measured at λ=640 nm: Adapted from [5].

In conclusion, the validation results described above for this new spectrophotometric platform demonstrates its reliability and applicability in characterizing homogenous turbid samples including those of high optical thickness. It should be noted that this new method has a $\mu_a$ detection floor of ~0.2 $mm^{-1}$ and thus not ideal for turbid samples with scattering albedo *a* close to 1.

# CHAPTER 5 : Cell Measurements

In this chapter, we present the results of various cell measurements perfomed in this dissertation research. Cell sample preparations including treatment with the chemotherapy drug doxorubicin as well as viability measurements will be described. The parameters of $\mu_a(\lambda)$, $\mu_s(\lambda)$ and g ($\lambda$) were determined inversely from the measured signals of MCF7 cell samples treated by doxorubicin and the control samples for $\lambda$ between 460 nm and 1000 nm in steps of 20 nm. We will discuss the wavelength dependence of measured signals and the radiative transfer parameters based on the interaction between light and cells in viable and apoptotic conditions.

## 5.1 Cell sample preparation and survival curve measurement

The MCF7 cells used in this study were purchased from ATCC (Manassas, VA, USA) and have been cryopreserved in liquid nitrogen in our laboratory for over 3 years. As described in chapter 2, the base medium recommended by the vendor for optimum cell growth was a complete media consisting of minimum essential medium (MEM) supplemented with 10% fetal bovine serum (FBS) and 0.01 mg/ml human recombinant insulin [89]. A 500 mL of complete cell culture media was prepared by mixing 450 ml MEM (Thermofisher, 1109507) with 50 mL FBS (Thermofisher, 1043702) and 1.25 mL insulin (Thermofisher, 12585014). The media was then sterilized by filtering using a 0.22 μm pore size filter system and then stored at 4 $^{o}$C.

The cells were grown in culture flasks with growth surface area of either 25 $cm^2$ ($T_{25}$) or 75 $cm^2$ ($T_{75}$). To prevent cell contamination, all cell preparations and maintenance were carried in a sterile environment using proper aseptic technique. Steps taken to minimize contamination during cells maintenance and preparation are described in detail in appendix C. Because MCF7 are

adherent cells, they need to be carefully detached from the bottom of the culture flask before they can be counted and seeded for treatment with drug. To detach the cells from a $T_{75}$ flask, the culture media already in flask was first discarded and then 2 mL of 0.05% trypsin-EDTA solution added to wash and rinse the cells and then discarded. 1 mL of trypsin was added, and the flask incubated at 37 $^{o}$C until the cells round up in about 2 to 5 minutes. Once the cells detach, the trypsin is neutralized by adding at least double the volume of complete growth medium and then the cells suspension transferred to a centrifuge tube. The cells were then centrifuged for 10 mins at approximately 150g. The medium was carefully aspirated and discarded leaving the cell pellets on the bottom of the centrifuge tube. The pellets were then resuspended in appropriate volume of complete growth medium and counted to establish their viability.

### 5.1.1 Cell counting by a hemocytometer

This is a technique often used for direct cell counting and viability assessment using the trypan blue solution to stain cells and has been described in details elsewhere [90]. Using this method, cells which still have their membrane intact are not stained by the dye while cell debris are stained blue due to their membrane permeability. Briefly, 50 μL of the cells to be counted are transferred into 1.8 mL microtube and mixed with equal volume of 0.4% Trypan blue solution. 10 μL of Trypan blue-treated cell suspension is each applied to both chambers of glass hemocytometer, allowing the cell suspension to be drawn out by capillary action to the counting chamber. Using a microscope with 10x objective, live unstained cells and dead stained from each of the four corner squares of the hemocytometer grid are counted using a hand tally counter. The average count of cells per square corner is multiplied by a factor of $2x10^4$ to obtain the total concentration of viable and dead cells in the original cell suspension. Cell viability is obtained as the ratio of total viable cells to the total number of viable and dead cells.

### 5.1.2 Apoptosis detection by MTT assay

As earlier described in chapter 2, the MTT assay measures the cell metabolic activity and hence able to accurately distinguish between viable and non-viable cells. To use this method, a calibration to determine the relationship between absorbance and viable cells numbers using the MTT assay need to be established first to obtain a reasonably accurate survival curve. To perform this, maximum number of viable cells is decided based on the expected cell density of the control sample during survival ratio measurements which should be about $5x10^5$ cells/mL. A summary of the MTT assay for both calibration curve and survival ratios is as shown in Fig. 5-1. Briefly, 100 µL of $5x10^5$ cells/mL suspension is added on the first three wells in the 96-well plate. Then half of the original density suspension is added to the next 3 wells, then 1/4, 1/8, 1/16, 1/32, 1/64, 1/128 of original density suspensions to respective triplicate wells. Cells are then incubated at $37^0$C, 5% $CO_2$ for 24 hours to attach them and have them recover from the preparation process. MTT assay is performed using the protocol described in details elsewhere [42].

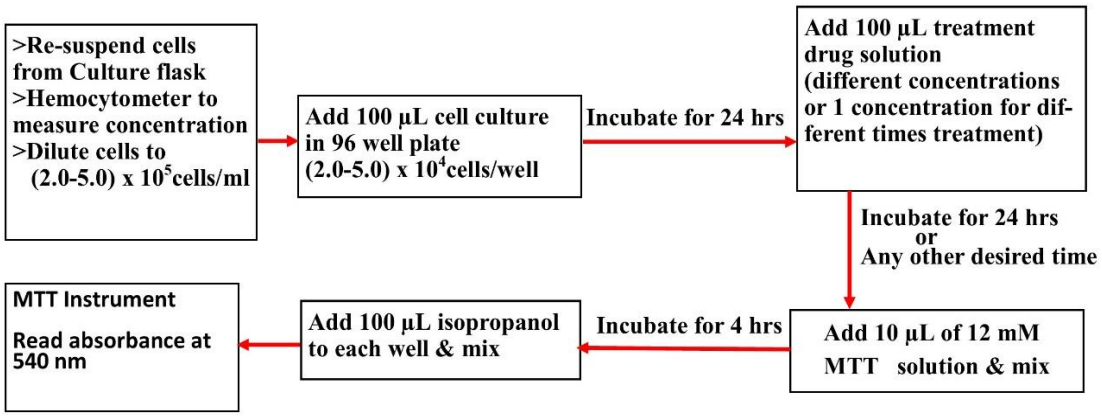


Fig. 5-1. The MTT Assay protocol for survival ratio measurement.

The cells survival ratios as a function of drug dose and treatment time obtained from MTT assay will provide a baseline quantitative characterization of cell apoptosis by the new method of turbidity spectrophotometry. To determine survival ratios as a function of dose, 100 µL of cell suspensions with density $5x10^5$ cells/mL or $5x10^4$ cells/well are seeded in triplicates into 24 wells of the 96 wells microtiter plate. The plate is then incubated for 24 hours to attach the cells to the bottom of the plate. After 24 hours, the medium in each well is replaced with 100 µL of freshly diluted drug with desired concentrations of 1, 2, 4, 8,16, and 32 µM and incubated for appropriate post-treatment time followed by the MTT assay. After the microtiter plate has been incubated for appropriate post treatment time, the media in each well is replaced with 100µL of fresh media. 10 µL of the 12 µM MTT stock solution is added to each well. A negative control of 10 µL of the MTT stock solution is added to 100 µL of medium alone wells also in triplicate. The plates are then incubated for 4 hours for cells' oxidoreductase enzyme to reduce the yellow MTT solution to a purple formazan pellet. The microtiter plates are then centrifuged at 200g and 10 mins to spin down the pellets and the supernatant carefully removed not to disturb the cell pellets. 100 µL of isopropanol solution is added to each well and mixed thoroughly using pipette to dissolve the pellet and obtain a purple color solution. The absorbance of the plates is then read using MTT instrument (Multiskan MCC340) at wavelength of 550 nm. The calibration curve and survival ratios were obtained by plotting the net absorbance from each of the wells against the number of cells in the respective wells and drug dose as shown in Fig. 5-2 below.

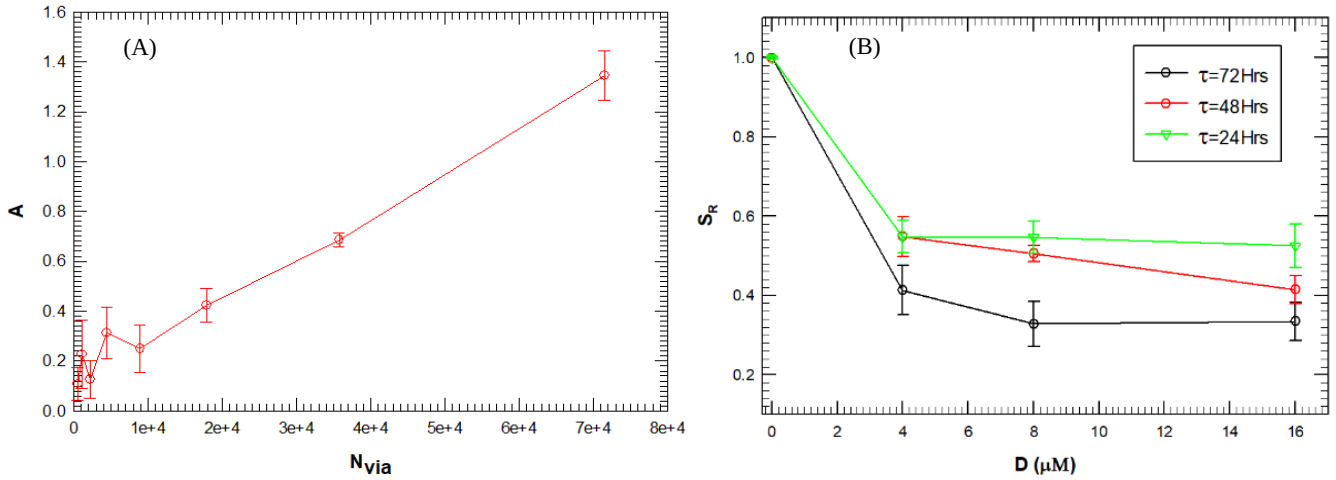


Fig. 5-2 (A) Relationship between absorbance A and number of viable cells per well $N_{via}$ for untreated MCF7 cells. (B) survival ratios $S_R$ vs doxorubicin drug dose D of 0, 4, 8 and 16 μM with post-treatment time τ of 24, 48 and 72 hours. Symbols and error bars represent the means and standard deviations obtained with samples from 3 wells of 96-well plate.

### 5.1.3 Apoptosis detection by fluorescent flow cytometry

As described in chapter 2, fluorescent-based assays can be used to offer more information about the state of cells undergoing apoptosis as compared to MTT and Trypan blue viability assays. The latter two assays only classify cells as either viable or non-viable while the fluorescent assay can quantitively classify cells into viable, early apoptotic, late apoptotic and debris. A fluorescence-activated cell sorting (FACS) flow cytometer can rapidly sort cells according to their respective apoptosis stages depending on their light scattering and fluorescent properties. This method uses two types of reagents to stain the cells and the stained cells quantified using a fluorescence flow cytometer or microscopy. Annexing V (FITC) reagent binds to phosphatidylserine, a marker of apoptosis when it is on the outer leaflet of the plasma membrane and hence only attaches to cells in early and late apoptosis stage as well cell debris. The second

reagent propidium iodide (PE-Cy5) is used as a cell viability agent as it only stain cells with compromised membranes. This reagent only stains cells in late apoptosis stage and cell debris. In addition to fluorescence measurements, the FACS method can be used to simultaneously measure the relative size and granularity of the cells based on their forward scattering (FSC) and side scattering (SSC) of incident laser light. To analyze cells by this method, we followed the following protocol. 3.5x $10^5$ cells were seeded in 13 $T_{25}$ flasks and incubated at $37^0$C, 5% $CO_2$ for 24 hours to attach them and have them recover from the preparation process. After 24 hours, cells in 3 flasks were treated with 3 different drug doses of 4, 8 and 16 μm and flasks returned in the incubator. The same treatment was applied to 3 other set of flasks after 48 and 72 hours. This protocol ensures that 96 hours after the cells were initially seeded to the flasks, we had 3 sets of 3 flasks with cells treated with 4, 8 and 16 μm drug doses with post-treatment times of 24, 48 and 72 hours. One flask contained untreated cells which was used as control. Once all the cells were incubated for appropriate post-treatment time τ, they were detached with trypsin, centrifuged, and then resuspended in a 15 mL conical tube with 1 mL complete cell culture media using a protocol described elsewhere. Cells in each conical tube were centrifuged and resuspended in 195 μL binding buffer. 5 mL of Annexin V-FITC dye was added to the cell suspension and then incubated for 10 min at room temperature while protected from light. 10 μL Propidium Iodine dye was mixed with the cell suspensions then FACS analysis performed using fluorescent flow cytometer (BD FACScan Cytometer) equipped with an excitation argon laser at 488 nm. Five thousand nuclei events were acquired with FASC per sample and data analysis performed using Flowjo_v10 software. Full flow cytometry results are as presented in Figs. 5-3 through 5-10 below.

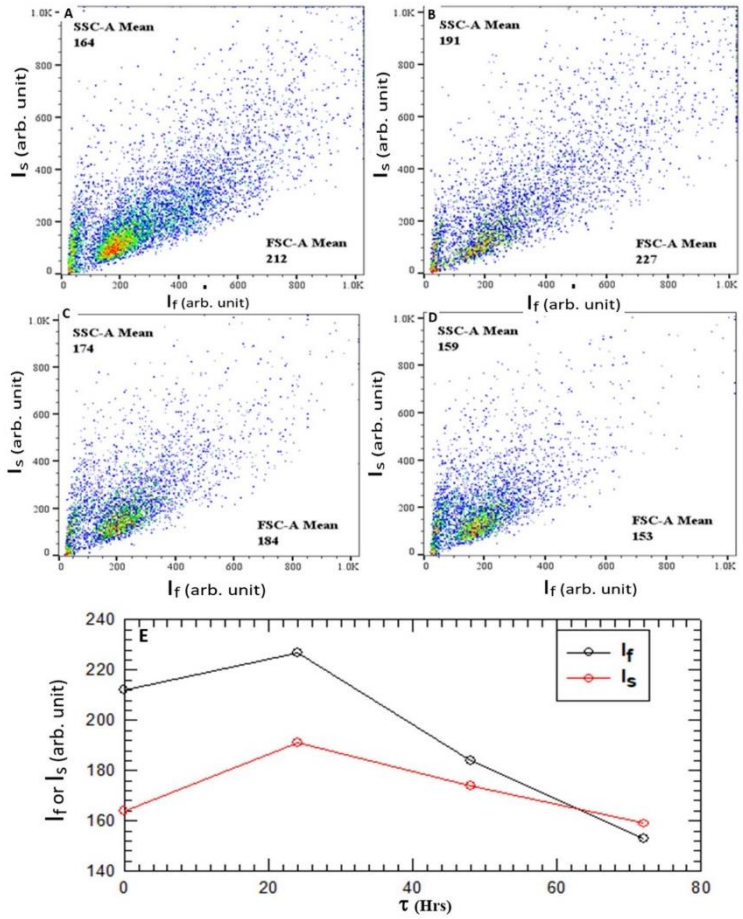


Fig. 5-3. Forward scatter intensity $I_f$ vs side scatter intensity $I_s$ density plot for MCF7 cell samples of (A) Control and those treated with doxorubicin drug of D = 4 μM and τ of (B) 24 hours, (C) 48 hours and (D) 72 hours. FSC-A and SSC-A means are the geometric means of forward and side scatter intensities. (E) Plot of the average scattered intensities vs τ. Excitation laser of λ=488 nm was used.

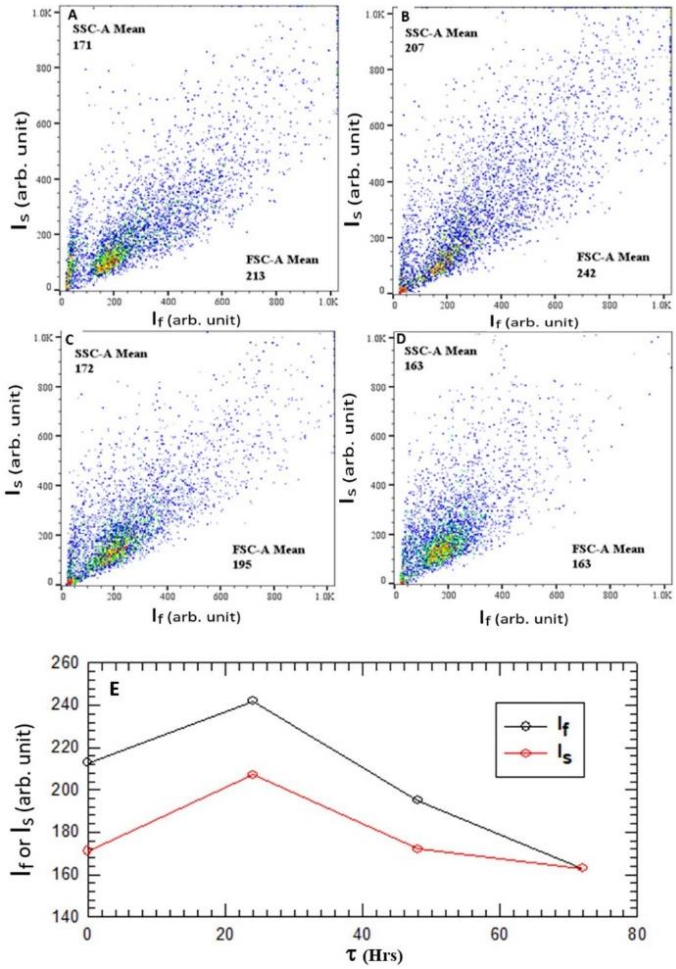


Fig 5-4. Forward scatter intensity $I_f$ vs side scatter intensity $I_s$ density plot for MCF7 cell samples of (A) Control and those treated with doxorubicin drug of D = 8 μM and τ of (B) 24 hours, (C) 48 hours and (D) 72 hours. FSC-A and SSC-A means are the geometric means of forward and side scatter intensities. (E) Plot of the average scattered intensities vs τ. Excitation laser of λ=488 nm was used.

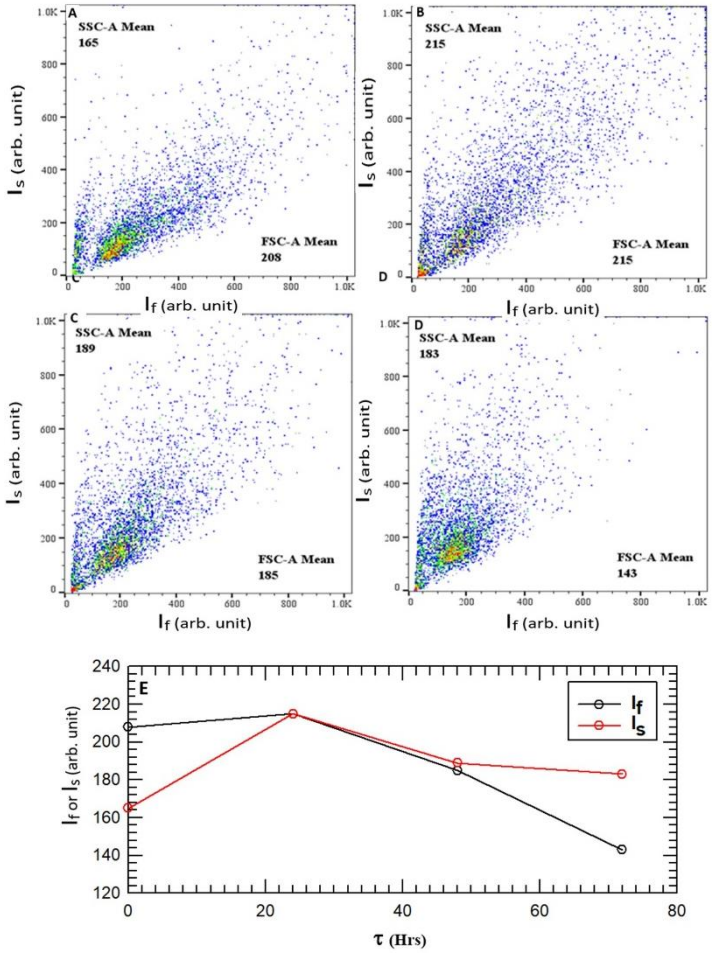


Fig 5-5. Forward scatter intensity $I_f$ vs side scatter intensity $I_s$ density plot for MCF7 cell samples of (A) Control and those treated with doxorubicin drug of D = 16 μM and τ of (B) 24 hours, (C) 48 hours and (D) 72 hours. FSC-A and SSC-A means are the geometric means of forward and side scatter intensities. (E) Plot of the average scattered intensities vs τ. Excitation laser of λ=488 nm was used.

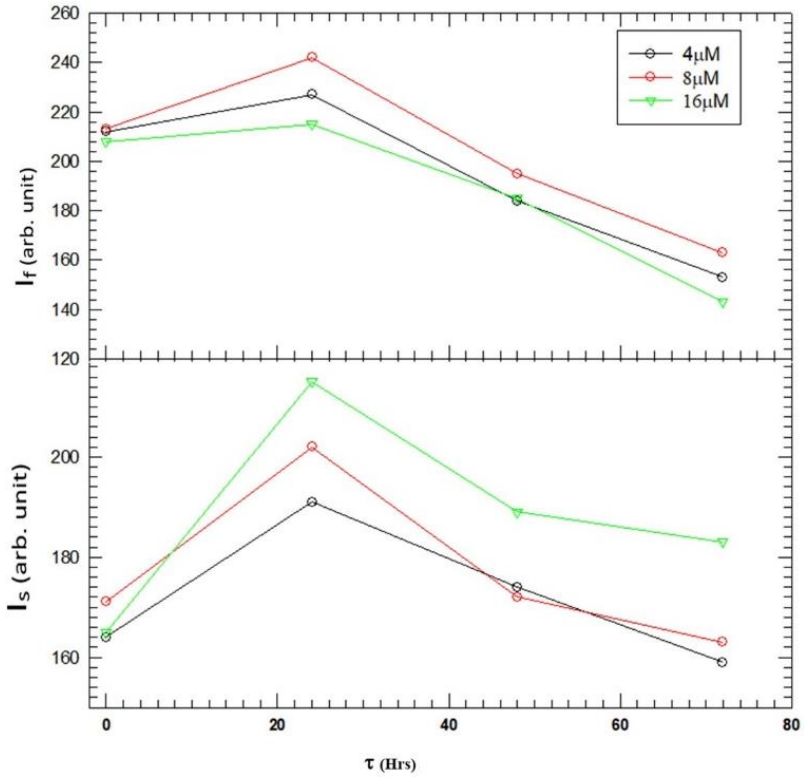


Fig 5-6. Summary of forward scatter intensity $I_f$ and side scatter intensity $I_s$ plots for MCF7 cells treated with D= 4, 8 and 16 μm and τ of 24, 48 and 72 hours. Control sample is represented by τ=0 hours. Excitation laser of λ=488 nm was used.

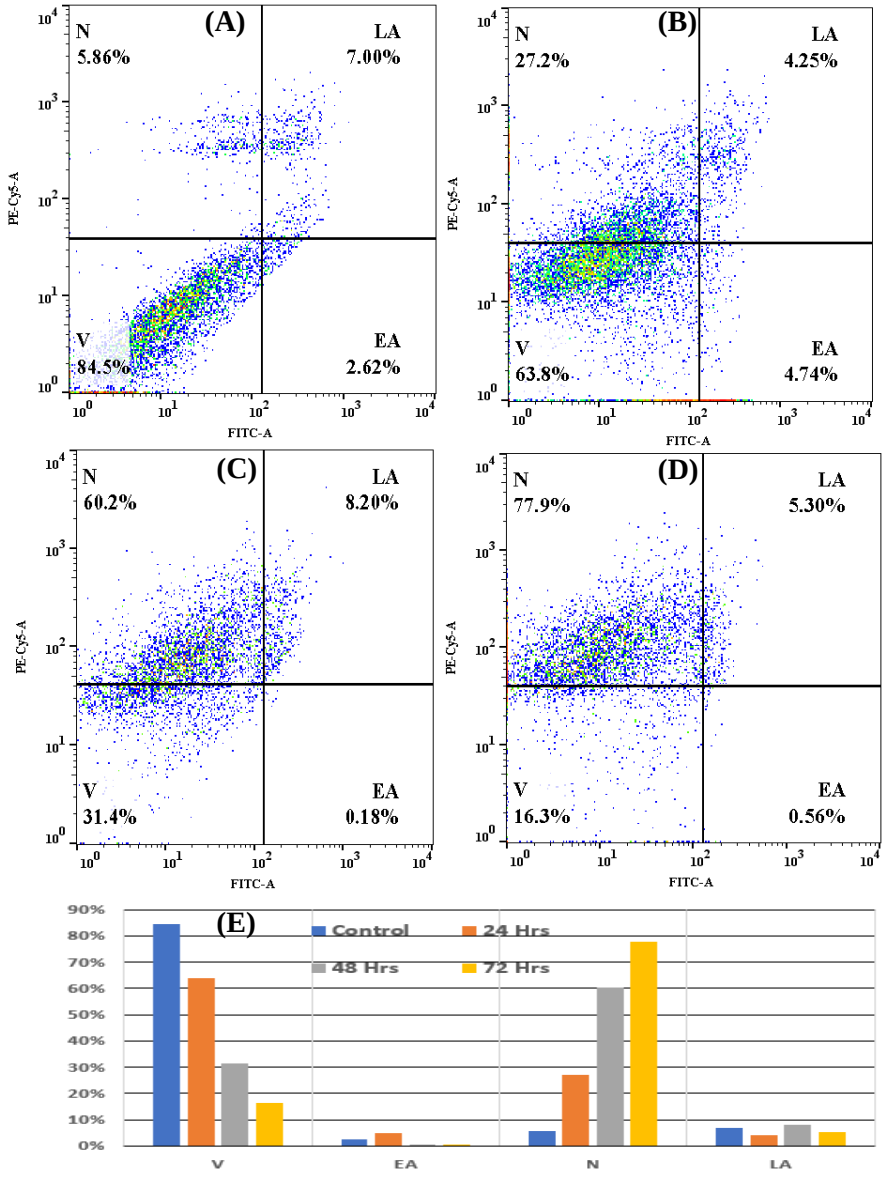


Fig 5-7. Flow cytometry plots of geometric mean flourescence intensity A of Annexin V (FITC) and propidium iodide (PE-Cy5) showing % of cells in Viable (V), Early Apoptosis (EA) , Necrotic (N) and Late apoptosis (LA) stages of MCF7 cell samples of (A) Control, and those treated with doxorubicin drug of D = 4 μM and τ of (B) 24 hours, (C) 48 hours and (D) 72 hours. (E) Summary of results. Excitation laser of λ=488 nm was used.

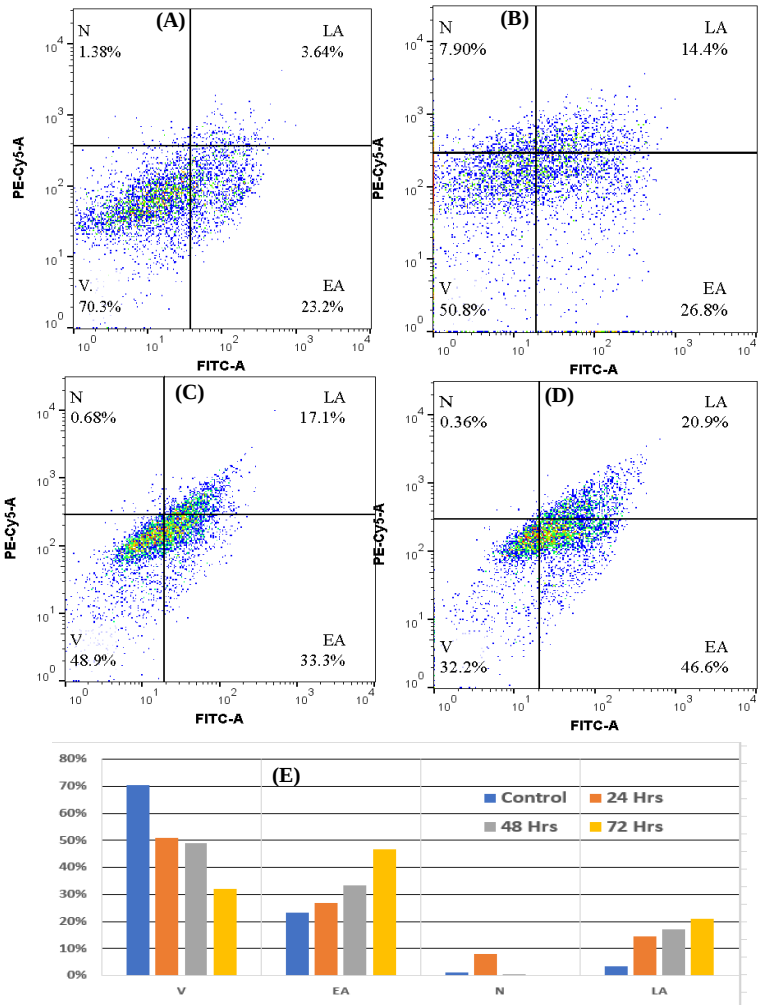


Fig. 5-8. Flow cytometry plots of geometric mean flourescence intensity A of Annexin V (FITC) and propidium iodide (PE-Cy5) showing % of cells in Viable (V),Early Apoptosis (EA) , Necrotic (N) and Late apoptosis (LA) stages of MCF7 cell samples of (A) Control, and those treated with drug of D = 8 μM and τ of (B) 24 hours, (C) 48 hours and (D) 72 hours.(E) Summary of results. Excitation laser of λ=488 nm was used.

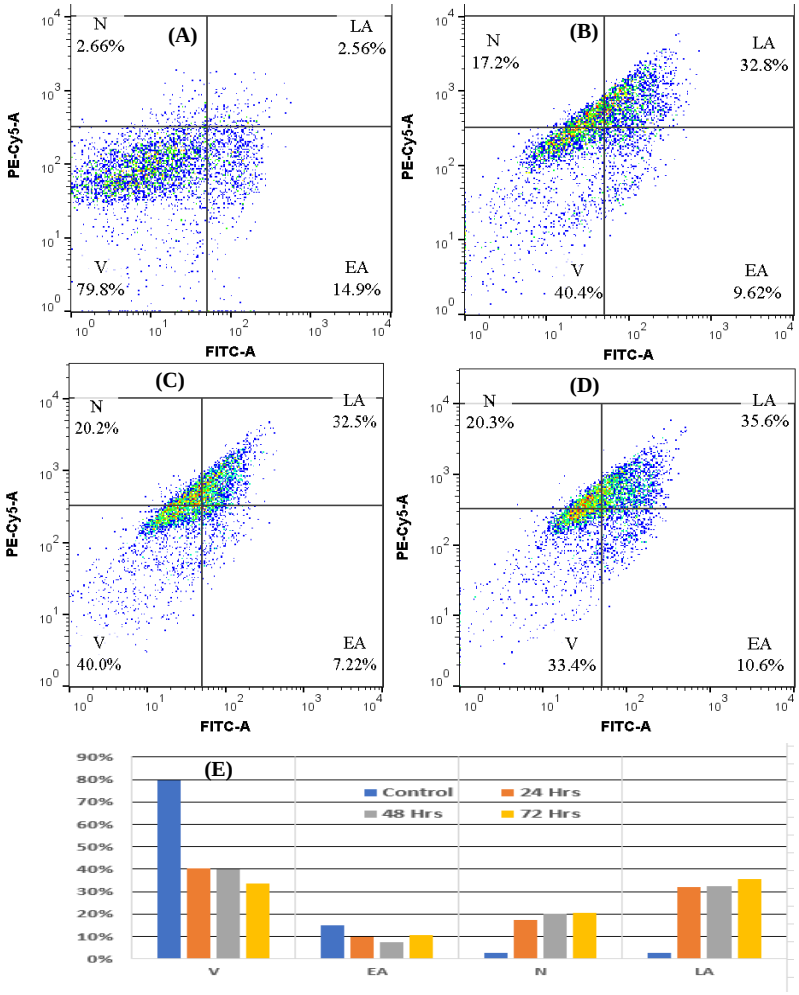


Fig. 5-9. Flow cytometry plots of geometric mean flourescence intensity A of Annexin V (FITC) and propidium iodide (PE-Cy5) showing % of cells in Viable(V),Early Apoptosis (EA), Necrotic (N) and Late apoptosis (LA) stages of MCF7 cell samples of (A) Control, and those treated with drug of D = 16 μM and τ of (B) 24 hours, (C) 48 hours and (D) 72 hours. (E) Summary of results. Excitation laser of λ=488 nm was used.

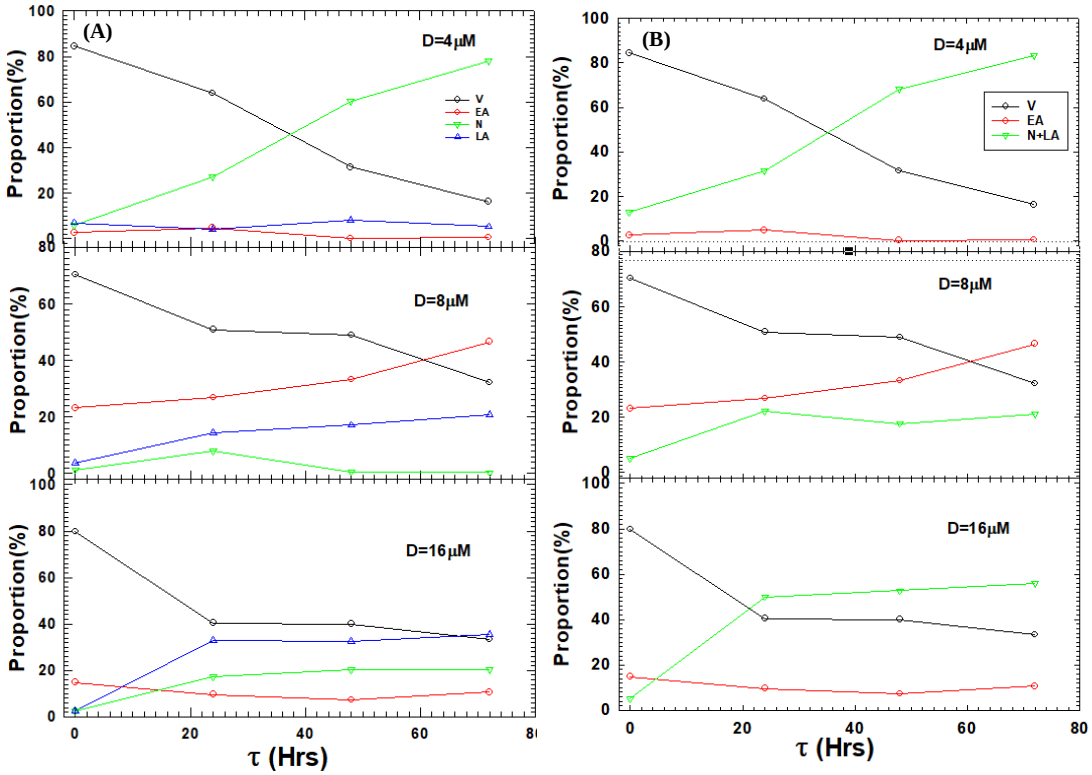


Fig 5-10. (A) Summary of Flow cytometry results showing % of cells in Viable (V), Early Apoptosis (EA) , Necrotic (N) and Debris (D) stages of MCF7 cells treated with drug of 4, 8,16 μM dose and τ of 24, 48, and 72 hours. (B) Proportion of cells in N and LA are grouped together. Cells were stained with both PI (PE-Cy5) and Annexin V (FITC) dyes and excitation laser of λ=488 nm was used.

The above results of flow cytometric measurement can be used to quantify cell apoptosis by analyzing their light scattering and fluorescence characteristics. To better understand the flow cytometry results presented above, one should consider how excitation and emission of other reagents in the cell sample interfere with the PI and FITC dyes signals as described in section 2.5.3. For instance, the excitation and emission spectra of the doxorubicin drug used to treat cells partially overlap with that of the PI fluorescent dye used in the flow cytometry experiment to quantify cells with compromised membrane. The excitation range of the doxorubicin drug is 400 to 540 nm with the peak excitation of 470 nm while that of the PI dye is 460 to 590 nm with a peak

of 535 nm. On the other side, the drug has a wide emission range of 530 to 650 nm and a peak of 560 nm while that of the PI dye is 550 to 680 nm with a peak emission at 625 nm. Because both their emission and excitation ranges overlap, the effect of the doxorubicin drug on fluorescent flow cytometry measurements should be understood. We performed an experiment to understand the effect of the drug's emission on cell measurements as follows. Four MCF7 cell samples to be used for the flow cytometry study measurements where prepared where sample A was the untreated control sample while samples B, C and D were treated with 4, 8 and 16 μm drug dose respectively for 3 hours. The treatment of 3 hours was to stain the cells with the drug without inducing apoptosis.  Flow cytometry results were then obtained and are as shown in Fig. 5-11 below.

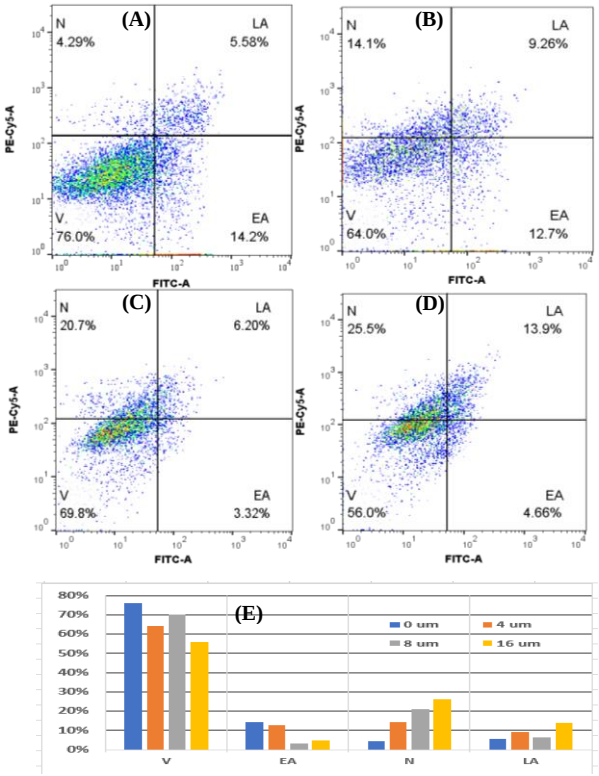


Fig. 5-11. Flow cytometry results showing percentage of cells in Viable(V), Early Apoptosis(EA),Late apoptosis(LA), and Necrotic(N) stages of MCF7 cells treated with doxorubicin  drug of (A)0μM, (B) 4 μM, (C) 8 μM and (D)16 μM  dose . Cells were stained with both PI (PE-Cy5-A) and Annexin V (FITC) dyes. (E)Bar chart summarizing the flow cytometry results.

From the set-up of this experiment, no cells were expected to be undergoing apoptosis from the drug treatment when the flow cytometry measurements were taken because of the short post treatment time. From the above results, it's evident that the samples treated with the drug shows a dose related increase of cells in neurotic phase which normally indicates cells stained with the PI reagent. However, in this case this can be regarded as false positive PI reagent signal with significant contribution assumed to be coming from the doxorubicin drug. From this finding, the control sample with untreated cells might not be a true control sample when comparing fluorescent flow cytometry results with the treated samples because it does not experience the drug interference effect. For flow cytometry measurements, its thus recommended to compare results of samples with the same drug dose and different post treatment time instead of those of same post treatment time and different drug dose.

From the flow cytometry results shown from Figs. 5-3 to 5-10 above for cells treated with 3 different doses and 3 post treatment times $\tau$, the FSC and SSC data can be used to give the overall information of the apoptosis process based on the cells' morphological characteristics. The FSC is related to the cell size while the SSC provides the cell granularity information. Viable cells have the largest sizes and favors FSC of light. Cell apoptosis is characterized by the initial cell condensation while with neurotic death, cells first swell before rupturing and releasing cellular contents. From Figs.5-7 and 5-9, the fluorescent flow cytometry results show presence of necrotic cells on treated cells. This can be used to explain why there is initial increase of FSC and SSC as shown in Figs. 5-3, 5-4 and 5-5 followed by rapid decrease of both signals with longer $\tau$ indicating presence of more cells with less granularity and decreased size which is associated with the late stages of apoptosis. It should be noted that the changes in light scattering alone cannot be used to exclusively stage apoptosis because reduced FSC and SSC values can be also as a result of

physically broken cells, cell debris and isolated nuclei[91]. For the fluorescent flow cytometry results, there is a clear trend between the proportion of cells at each apoptosis stage to the corresponding drug dose and τ. At smaller dose and shorter τ, viable cells form the majority of cells in the sample as shown in Fig. 5-10, and then decrease gradually with both higher dose and τ. In contrary and as expected, the total proportion of cells classified either as necrotic or debris in the samples increase with increasing dose and τ. It should however be noted that for drug dose of 4 and 16 μM, there is significant proportion necrotic cells in the samples which could not be fully determined if the signal was partially from the drug and PI fluorescent signal overlap as described earlier in this section or from mechanical death of the cells during cell preparation. From the results, it can also be observed that the EA phase for doses of 4 and 16 μM mainly consists of transient cells as their proportion remain unchanged with increasing τ apart from 8 μM dose which indicates a slight increase with increasing τ. These results will be useful later when correlating this cell apoptosis data to that obtained from the spectrophotometric measurements as described in the next section.

## 5.2 Spectrophotometric measurement of untreated MCF7 cells

### 5.2.1 Dependance of light signals on cell sample density

The measured light signals of suspended cells are proportional to the concentration of the cells used in the sample as described in chapter 3. Stronger light scattering sample increases the signal-to noise ratio of the measured light signals so the optimum sample cell concentration should be used, that is the minimum cell concentration required to produce scattered signals relatively higher than the background signals. To investigate the relationship between measured signals and cells concentration, we obtained the measured light signals of samples with known cell density.

Four turbid samples will cell densities of ~(2.0, 4.0, 6.0, 7.5)x$10^6$ cells/mL were used and the measured signals obtained using the spectrophotometric system. The measurements were performed at six wavelengths shown below.

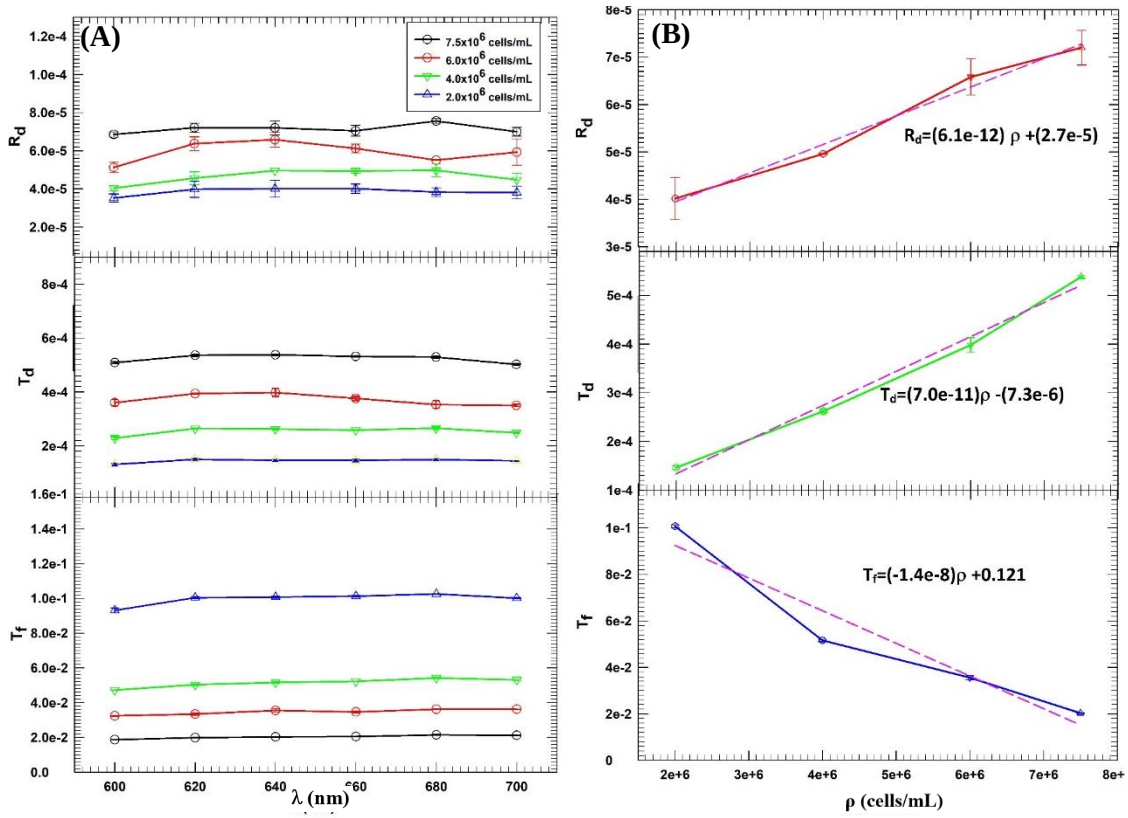


Fig 5-10. (A) Summary of Flow cytometry results showing % of cells in Viable(V), Early Apoptosis(EA) , Necrotic(N) and Debris(D) stages of MCF7 cells treated with DOX of 4, 8,16 μM dose and τ of 24, 48, and 72 hours. (B) Proportion of cells in N and LA are grouped together. Cells were stained with both PI(PE-Cy5) and Annexin V (FITC) dyes and excitation laser of λ=488 nm was used.

As can be predicted, the results indicate a linear proportionality between the measured signals and the concentration of the sample. A trendline of the measured signals at λ=640 nm is also added to give the numerical equations of $R_d$, $T_d$ and $T_f$ to the cell density ρ. These relationships will be useful for deciding the right number of cells to use per sample to produce measured signals in a particular range of interest.

### 5.2.2 Effect of cell suspension settling on light signals

The MCF7 cells suspended inside the sample holder were visually observed to settle down on the bottom glass holder within the first three minutes after sample preparation. This is due to cells mass density being higher than that of the suspending culture media [92]. To study the effect of cells settling to the measured scattering signals, we conducted two experiments as follows. A sample containing MCF7 cells of density ~$2x10^6$ cells/mL was prepared and spectrophotometric measurements performed to obtain measured signals at $\lambda$=640 nm. The sample was shaken once at the beginning of measurements to ensure uniform cell suspension and then light signals acquired every 10s for 3 minutes. Results show that the mean measured signals $R_d$, $T_d$ and $T_f$ had relative standard deviations of 11.1%, 2.0% and 2.1% respectively as shown in Fig. 5.13 below.

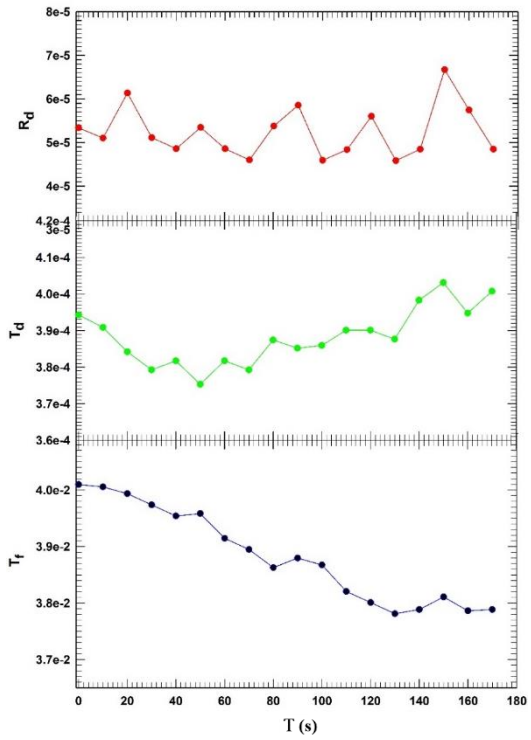


Fig.5-13. Cells suspension settling down effect on measured signals of $R_d(t)$, $T_d(t)$, and $T_f(t)$ for a turbid cell suspension sample. Where "t" is the settling time (seconds) from when the sample is initially shaken to obtain uniform cell suspensions.

From these findings, we concluded that cells settling inside a sample have a significant effect on measured light signals. It is thus recommended to shake the cell sample to keep the cells suspended during the signal acquisition at each wavelength.

### 5.2.3 Effect of Phenol red dye on light signals

Most in vitro tissue culture media contain phenol red dye typically in the concentration of 5-15 mg/mL. The dye is a pH indicator and has a red coloration at neutral pH media. When the culture media is contaminated by pathogens or there are excess mammalian cell waste products, the pH of the media slowly decreases causing the phenol red culture media to turn from red, orange and then yellow. To maintain pH for relatively long time, a continuous supply of 5% $C0_2$ like the one in the incubator is needed. However, it was observed that when cell media with phenol red dye was used to suspend the cells in the sample used for spectrophotometric measurements, its color significantly changed within the first 1 hour and caused a significant change in the measured light signals between $\lambda$=460 nm and 600 nm. To study the effect of this color change to the spectrophotometric measurements, we prepared two turbid samples each with ~$5.0x10^5$ cells/mL but suspended them in either (A) phenol red or (B) phenol red free media. The measured signals were obtained for each sample at post-sample preparation time of 0 and 1 hour as shown in Fig. 5-14 below.

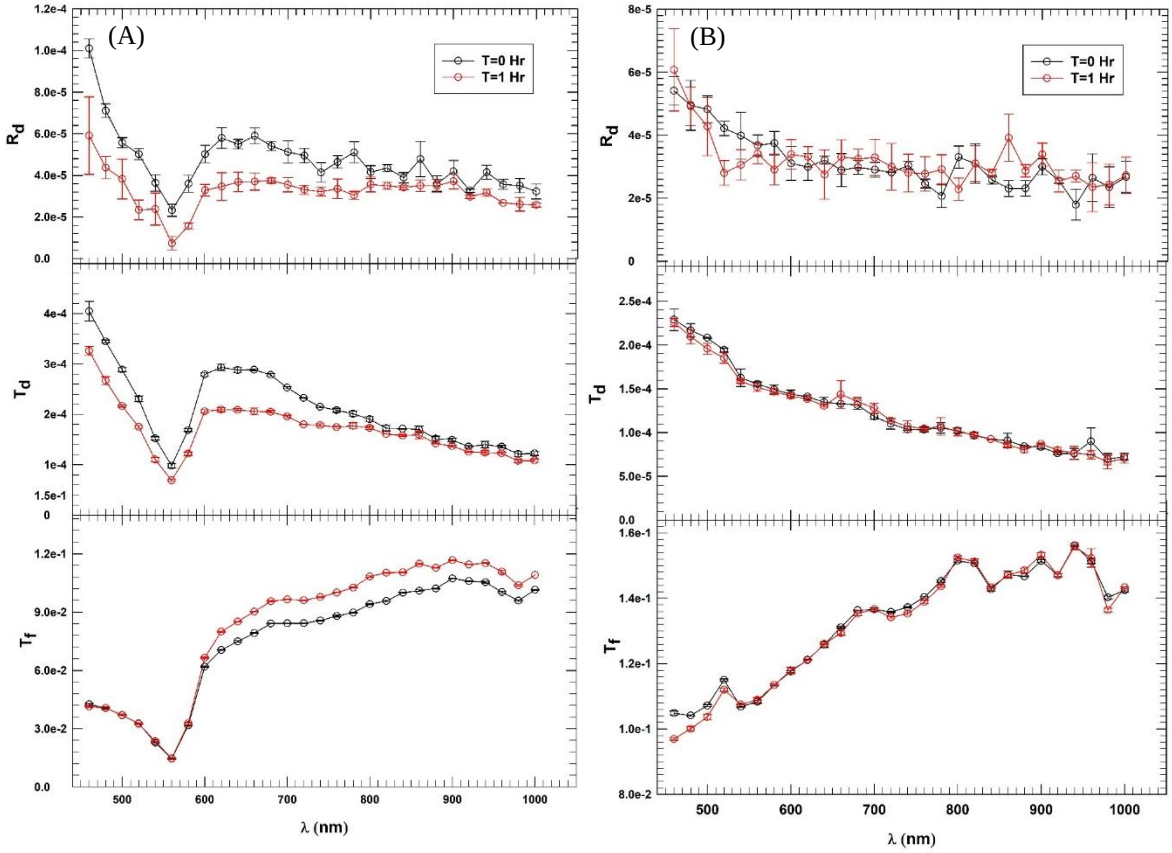


Fig. 5-14. Comparison of measured signals of $R_d(\lambda)$, $T_d(\lambda)$ and $T_f(\lambda)$ from cells suspended in (A)phenol red and (B)phenol red free culture media at post-sample preparation time of 0 and 1 hr to study the impact of phenol red dye in spectrophotometric measurements.

Results shows that the measured light signals obtained from phenol red sample had a significant change between 0 and 1 hour for signals between λ=460 nm and 700 nm. In addition, the signals had a sharp drop at λ=560 which corresponds to the known peak absorbance of phenol red dye [93]. This peak absorbance value changes with pH change and this could explain why the measured signals changed within 1 hour as the sample was not kept in carbonated environment during measurements. The sample prepared using phenol free media did not indicate any change of measured signals within 1 hour or show any presence of any peaks across the range of spectrum measured. We thus concluded that phenol red media do affect spectroscopic measurements in the

range of λ=460 nm and 700 nm unlike the phenol red free media. The phenol red media was thus used to grow the cells only, then phenol red free media was used to suspend the cells in the turbid spectrophotometric sample to address this concern.

## 5.3 Spectrophotometric measurements of treated MCF7 cells

To study the effect of cells treatment with doxorubicin drug to the measured light signals, we set to obtain the optical signals of cells treated with different drug dose for different post treatment time for wavelengths λ from 460 nm to 1000 nm in steps of 20 nm. We prepared triplicate cells samples with three different drug doses of 4, 8 and 16 μM each with three post treatment time of 24, 48 and 72 hours. A control or untreated sample was also prepared. As described in the chapter 3, the optical properties of cells depend on the cell concentration and cross sections. Since in this experiment we want to study how the optical properties vary with the cross sections of cells undergoing apoptotic process, its critical to ensure each cell turbid sample contains approximately the same number of cells or concentration. The cells preparation and treatment with the doxorubicin drug were performed as follows. First, we prepared a stock solution of the doxorubicin drug (Sigma-Aldrich, 25316-40-9) of concentration 128 μM in deionized water as described in appendix B. We then followed the protocol summarized in Fig. 5-15 below or appendix C to ensure that each spectrophotometric sample had the same total solid mass consisting of a mixture of viable, apoptotic and debris cells.

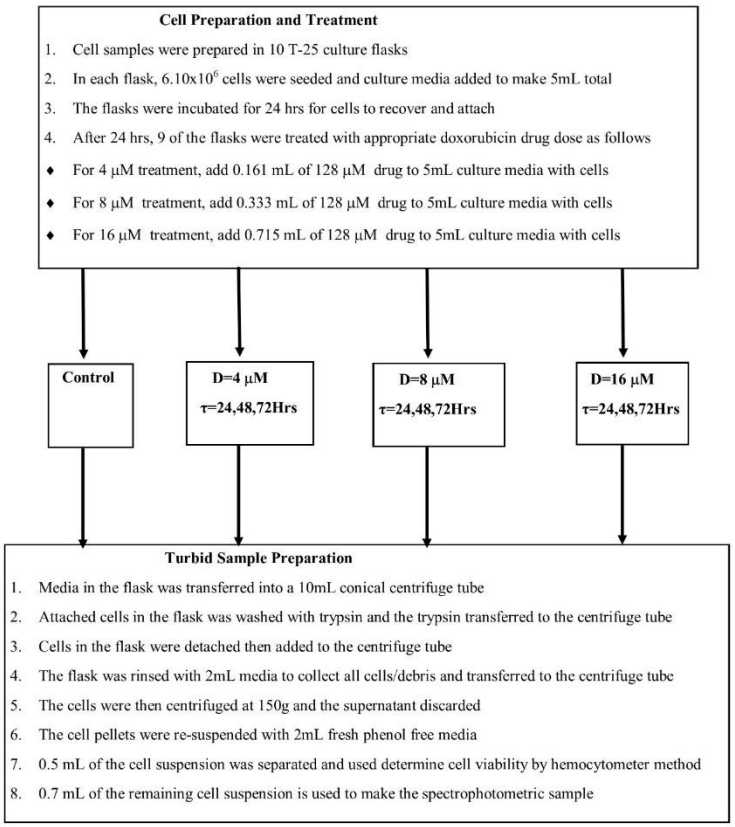


Fig 5-15. Protocol for cell preparation and treatment for making 10 turbid spectrophotometric samples of different drug dose and post treatment time τ, including control sample. Procedure ensures all samples have the same cell mixture density.

The turbid cell spectrophotometric samples were prepared using the same procedure as for microsphere samples as described in the experiment chapter. Each sample was prepared using the same sample holder with thickness D=4.06±0.01mm to ensure uniformity. The distances and orientations of photodetectors $D_3$ and $D_4$ from the back glass center surface and $D_2$ from the front glass center surface of the sample holder with the z-axis as shown in Fig. 4.3 were $d_R$=21.5 mm, $d_T$=35.8mm, $d_F$=110.9 mm and $\theta_R=45^0$, $\theta_T=48^0$ and $\theta_F=9^0$. The incident beam orientation to the front glass center surface normal was $\theta_0=9^0$ and the beam size along x and y direction was 10.5mm and 4.5mm respectively. The inner diameter of the sample spacer was 14.25 mm. Measured light

signals of $R_d$, $T_d$ and $T_f$ were obtained as described in section chapter 4 for $\lambda$ between 460 nm and 1000 nm in steps of 20 nm. Three light signals were acquired at each wavelength to obtain mean values and standard deviation for each wavelength. The sample was shaken after each wavelength measurement to prevent cell settling effect on measured lights signals described in section 5.3.2. Then iMC code was used to fit the light signals as described in the in the experiment chapter and the results are presented below.

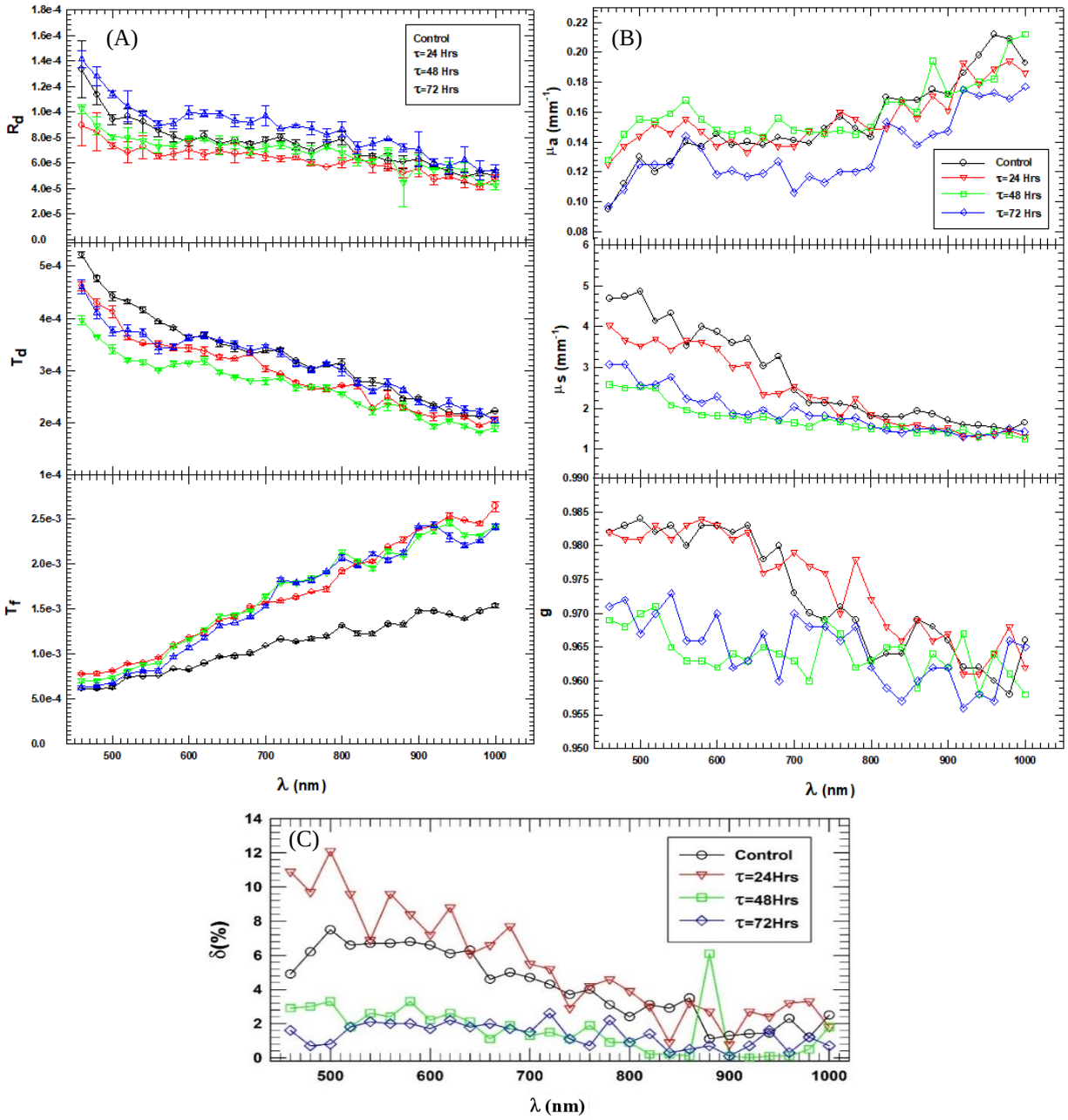


Fig. 5-16 (A) Measured light signals $R_d(\lambda)$, $T_d(\lambda)$, and $T_f(\lambda)$ and (B) simulated optical signals of $\mu_a(\lambda)$, $\mu_s(\lambda)$, and $g(\lambda)$ for MCF7 cells treated with doxorubicin drug dose of 4 μM with post treatment time τ of 24, 48 and 72 hours. (C) The iMC delta δ values representing the squared error between measured and calculated signals. Control sample is the untreated sample measured at τ =0. The symbols represent the mean values and error bars represent the standard deviation of three sets of measured data sets per λ for a sample of thickness d=4.06 mm.

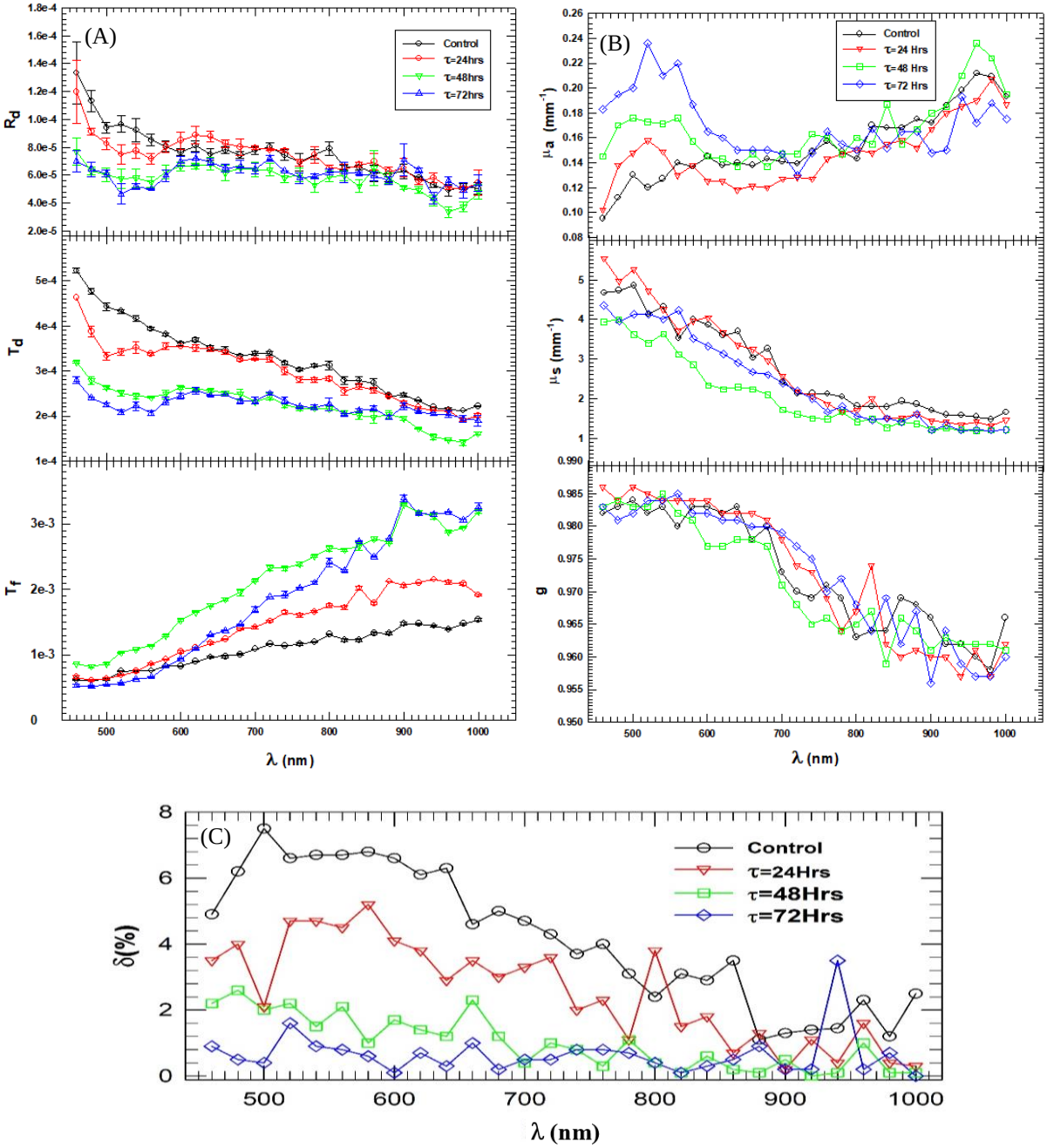


Fig. 5-17(A) Measured light signals $R_d(\lambda)$, $T_d(\lambda)$, and $T_f(\lambda)$ and (B) simulated optical signals of $\mu_a(\lambda)$, $\mu_s(\lambda)$, and $g(\lambda)$ for MCF7 cells treated with doxorubicin drug dose of 8 μM with post treatment time τ of 24, 48 and 72 hours. (C) The iMC delta δ values representing the squared error between measured and calculated signals. Control sample is the untreated sample measured at τ =0. The symbols represent the mean values and error bars represent the standard deviation of three sets of measured data sets per λ for a sample of thickness d~4.06 mm.

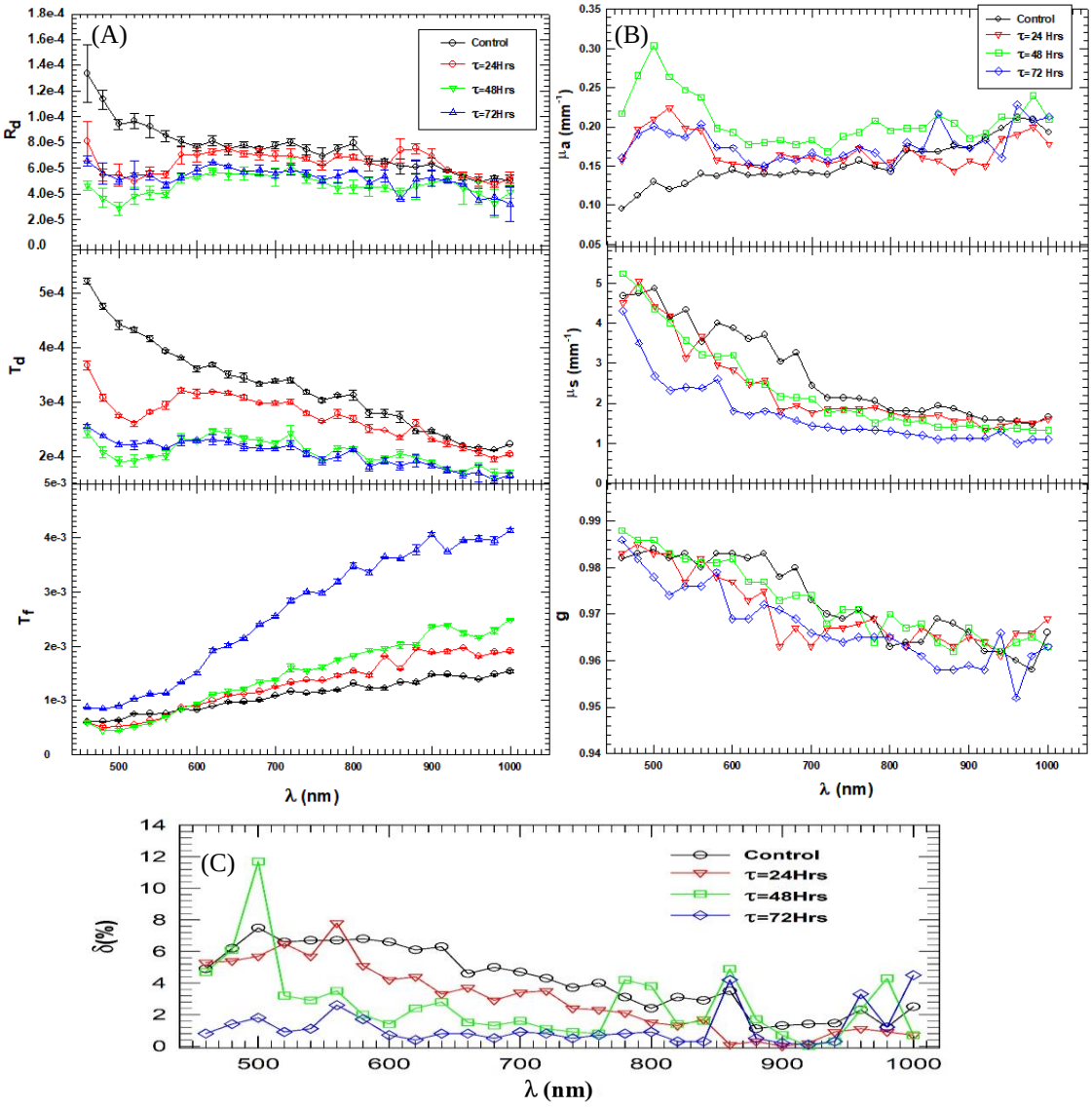


Fig 5-18 (A) Measured light signals $R_d(\lambda)$, $T_d(\lambda)$, and $T_f(\lambda)$ and (B) simulated optical signals of $\mu_a(\lambda)$, $\mu_s(\lambda)$, and $g(\lambda)$ for MCF7 cells treated with doxorubicin drug dose of 16 μM with post treatment time τ of 24, 48 and 72 hours. (C) The iMC delta δ values representing the squared error between measured and calculated signals. Control sample is the untreated sample measured at τ =0. The symbols represent the mean values and error bars represent the standard deviation of three sets of measured data sets per λ for a sample of thickness d=4.06 mm.

From the above results of spectrophotometric measurements shown in Figs. 5-16, 5-17 and 5-18, we can identify a weak trend of measured optical signals $\mu_a(\lambda)$, $\mu_s(\lambda)$, and $g(\lambda)$ with drug dose D and post-treatment time $\tau$. For the treated samples with D = 4 $\mu$M, the measured optical signals seem to have an inverse relationship with $\tau$. For the samples of D = 8 $\mu$M, the measured signals do not show a clear trend with the post treatment times. In comparison, the untreated samples have the highest values of absorption and scattering coefficients and tend to favor forward scattering of light than the treated cell samples. Lastly, the 16 $\mu$M sample likewise does not indicate a clear trend but overall, the sample with $\tau$ = 24 hrs seems to have the highest values of absorption and scattering coefficients and scattering in the forward direction compared to the other samples. By looking at the overall results, $\mu_s$ seems to follow the clearest trend where it has inversely proportional relationship with $\tau$ for all sample doses. This is an indication that viable cells are scattering light more compared to the less viable cells and at the same time favoring scattering in the forward direction. From both the measured light signals and optical parameters curves as shown in Figs. 5-16, 5-17 and 5-18, all treated samples show a characteristic light absorption between $\lambda$=460 nm and 600 nm which is direct proportional to the drug dose. This can be attributed to the characteristic absorbance of doxorubicin drug at 480 nm and that of phenol red dye used in the cell culture media with absorbance peak of 560 nm [93, 94] as earlier described in Sub-section 5.2.3. This extra absorbance by these two reagents should be considered while studying the absorption of cells in that spectrum segment. With this consideration, when we compared the measured signals at higher wavelengths >800 nm, where we could easily identify a correlation of optical parameters with D and $\tau$. This comparison was done by averaging each optical parameter across all wavelengths for $\lambda$>800 nm and comparing with those from the same D but different $\tau$. For $\lambda$>800 nm and for each drug dose, the control sample have the largest values of $\mu_a$, $\mu_s$ and g

while those of $\tau$ =72 hours have the smallest values. This can be described by the fact that viable cells are the most turbid, largest in size and more granular than apoptotic or cell debris which have overall reduction of scattering and absorbing cross-sections due to their loss of turbidity. As a result, viable and EA cells absorb and scatter light more as indicated by $\mu_a$ and $\mu_s$ plots while favoring forward scattering of light as demonstrated by the highest values of g as shown in Figs. 5-16, 5-17 and 5-18 above.

It should also be noted that iMC delta $\delta$ values for some wavelengths across the samples measured were not able to converge to under 3%. The $\delta$ values ranged from 0% to 12% across all wavelengths of the simulated measurement data. This can be attributed to several factors. From the three measured light signals acquired per wavelength and averaged, they had relative experimental errors ranging from 1.3% to 6% with an average value of 3%. Experimental errors in sample preparation or cell settling effect could have led to these large $\delta$ values at some wavelengths due to the fluctuation of the three acquired light signals. In addition, the iMC code used to simulate the measured light signals in this study did not employ the inverse algorithm which is still in development. Instead, we ran multiple loops of the iMC code to obtain the distribution of objective function $\delta$ in the radiative transfer parameter space for manually searching for the minimum values of $\delta$. This could have contributed to the inability to find the smallest possible $\delta$ for each wavelength. Once the final iMC code with improved inverse algorithm is fully developed, we believe even smaller $\delta$ values can be achieved by optimized search algorithm.

# CHAPTER 6 : Summary and Conclusion

In this dissertation research, we have developed and validated a new spectrophotometric method with potential applications in various fields such as material characterization and life science. Label-free detection of apoptosis in different cell samples treated with a chemotherapy drug has been investigated based on the morphological changes of cells undergoing apoptosis. This new method was used to measure three light signals of $R_d(\lambda)$, $T_d(\lambda)$ and $T_f(\lambda)$ from each cell sample over a spectral range of $460 \leq \lambda \leq 1000$ nm. And in-house developed iMC code was applied to obtain the optical parameters of $\mu_a(\lambda)$, $\mu_s(\lambda)$ and $g(\lambda)$ based on the RT theory. By comparing the optical parameters of treated cells obtained by the new method to the results obtained by other apoptosis assays, we have demonstrated that a strong correlation exists between them.

Most conventional spectrophotometric methods for turbid characterization use integrating spheres to measure light signals and even the recent developed ones which do not use integrating spheres still requires one to use multiple samples of small optical thickness to obtain $\mu_t$ from $T_c$ light signal. This poses several challenges in obtaining optical properties of cell samples as discussed in detail in chapter 2. The development of new method presented in this dissertation research addresses the existing challenges as it requires only one cell suspension sample and three single photodetectors to obtain three light signals from the sample. To validate this new system, we obtained the optical properties of two polystyrene microsphere samples with microsphere size of 0.966 and 11 μm in a spectral range of 460 to 1000 nm as described in chapter 4. For comparison, we also calculated the optical parameters of the same microsphere suspensions using the already established Mie theory based on Matlab code at the same wavelengths and sample conditions as the experiment. As shown in Fig. 4-14, the microsphere optical parameters obtained by our new spectrophotometric system closely matches those predicted by the Mie theory for both

microsphere size suspensions particularly for $\mu_s$ and g where in average they were matched within 3%. However, the $\mu_a$ values experimentally obtained significantly disagreed to those calculated by Mie theory for both microsphere size samples. For 0.996 μm sample, the experimental $\mu_a$ values were overestimated by ~140% while those of the 11 μm sample were overestimated by ~20%. The discrepancy can be explained by the model used to calculate results using Mie theory. Using the complex refractive index function $n(\lambda)=n_r(\lambda)+in_i(\lambda)$, the $\mu_s(\lambda)$ and $\mu_a(\lambda)$ are mainly affected by $n_r(\lambda)$ and $in_i(\lambda)$ components respectively. But the measurement uncertainty in measured values of $in_i(\lambda)$ is larger than those of $n_r(\lambda)$ and thus the $\mu_a(\lambda)$ values obtained by the two methods is expected to have a larger discrepancy than that of $\mu_s(\lambda)$. The small discrepancy on values of $\mu_s(\lambda)$ and $g(\lambda)$ obtained by the two methods can be related to the microsphere suspensions settling effect, and aggregation/size distributions of microspheres as described in Figs. 4-11 and 4-15 in chapter 4. From these validation results, we can demonstrate that this new spectrophotometric method can be applied in characterizing turbid samples including those of high optical thickness unlike other existing methods. However, this method suffers one limitation as its not ideal for turbid samples with scattering albeldo *a* close to 1 as it seems to have $\mu_a$ detection floor of ~0.2 $mm^{-1}$ as shown in Fig. 4-14 (A).

As one of the aims for this dissertation research, the validated spectrophotometry system was tested for its applicability in the oncological field by establishing the dependence of the optical properties of the treated cells to the various morphological features associated with cells at each stage of apoptosis namely viable, EA, LA and cell debris. For this study, we obtained the optical parameters of cells treated with three different drug doses of D= 4, 8, and 16 μM for three post treatment times of $\tau$=24, 48 and 72 hours. First, it should be noted both the phenol red dye used in the cell media and doxorubicin drug in the cell samples both have a characteristic absorption in

the range $480 \leq \lambda \leq 600$ nm as shown in Fig. 5-14. For comparison of optical parameters particularly $\mu_a$, it is advisable to avoid this spectral window due to the interference caused by the extra absorption directly related to the doxorubicin drug dose and phenol red dye concentration in the sample. Although we used phenol red free media to prepare the spectroscopic cell suspension sample, it was observed that the cells had some reddish coloration which can be attributed to staining by the phenol red media which the cells are normally cultured in. As shown in Figs. 5-16, 5-17 and 5-18, we established that overall, the control sample with untreated cells has the highest values of $\mu_a$, $\mu_s$ and g followed in order by those of $\tau$ =24, 48 and 72 hours for each set of D=4, 8 and 16 μM. This can be related to the cell morphological changes during apoptosis as described in Fig. 2-4. Viable and EA cells are expected to be large in size, more turbid and granular than cells in LA and debris phase. Turbid cells absorb more light hence higher $\mu_a$ values while granularity increases light scattering by the cell which directly affects $\mu_s$. Larger cell size favors forward scattering of light which can related to higher values of g. Cells in later stages of apoptosis have diminished scattering and absorbing cross-sections due to their significant loss of turbidity and granularity and this leads to lower values of $\mu_a$, $\mu_s$ and g. Although at some wavelengths the optical parameters might not be statistically different due to overlap, their overall trend can be used to qualitatively identify a general trend needed for comparison with the existing apoptosis assays. Generally, at $\lambda \geq 800$ nm, we were able to correlate the optical parameters of apoptotic cells to the cell conditions at each apoptosis stage.

In order to evaluate the accuracy and reliability of our new spectrophotometric method in staging apoptosis, we needed baseline data for comparison, and this was obtained using existing apoptosis assays. First, we used the MTT assay to obtain the survival ratios $S_R$ of cells treated with same D for the same $\tau$ as showed in Fig. 5-2. As expected, the $S_R$ for each cell sample is inversely

related to D and τ. It should be noted that apart from τ=48 hours, no explicit $S_R$ dependence on D was observed for samples treated with drug dose of D≥8 μM. Secondly, we also used the flow cytometry FCM to stage apoptosis of cells treated with the same D for the same τ as the MTT and spectrophotometric samples by analyzing the cells light scattering and fluorescence properties. Unlike the MTT assay which only classify viable cells, the FCM is able to classify treated cells into four categories of viable, EA, N and LA or debris as shown in section 5.1.3. In addition, the FCM method provided the overall information on cell size and granularity based on FSC and SSC data respectively. Based on the summary of fluorescence results as shown in Fig. 5-10, this method was able to provide the baseline data needed to compare with our new spectrophotometric assay by relating the proportion of cells at each apoptosis stage to the corresponding D and τ. With smaller D and shorter τ, viable cells dominate the samples but then decrease gradually with both higher dose and τ. As can be predicted, the total proportion of cells classified either as necrotic or LA in the samples increase with increasing D and τ apart from the samples treated with D=8 μM. Samples treated by this dose shows unusually high presence of cells in EA phase compared to the rest. This is an indication that majority of the treated cells are still transiting from viable to LA phase. As described in Fig. 5-11, it should be noted that doxorubicin drug used to treat the cells may affect fluorescent measurements because the drug and the PI fluorescent dye used to stain cells with compromised membrane have a partially overlapping excitation and emission spectra.

By qualitatively comparing the optical parameters of treated cells obtained by the new spectrophotometric method to MTT and FCM results, we were able to demonstrate the potential of using the new method as an alternative for staging cell apoptosis. For instance, if we compare the spectrophotometric and FCM results of cell samples of the same dose D with τ=24, 48 and 72 hours as shown in Figs.5-9 and 5-18(B), we can identify samples with high proportion of viable

cells as those with the largest values of $\mu_a$, $\mu_s$ and g. Moreover, the information contained in the measured light signals as shown in Fig. 5-19(A), can also be used to compliment the optical parameters in characterization of apoptotic cells. The magnitude of $R_d$ and $T_d$ scattering light signals dominate for samples with the highest proportion of viable cells while it is reverse for $T_f$ light signals. This can be attributed to cell samples with large $\mu_t$ which is characteristic of cells in viable or EA phases of apoptosis. The vice versa can also be explained for cell samples with the least proportion of viable cells.

Based on the results of this dissertation research, we have demonstrated that this novel spectrophotometric system for characterizing turbid materials has a high potential of being applied to quickly and accurately stage apoptosis. However, this method needs significant improvement before it can become an effective technique for analyzing cellular apoptosis and other applications. For example, one may determine the proportion of apoptotic cells in each sample in a similar way to that of FCM. This can be achieved by first solving the system of linear equations for absorbing and scattering cross-sections $\sigma$ and number density $\rho$ of cells at each apoptosis phase using the optical parameters obtained at each $\lambda$ as discussed in Subsection 3.5. Another improvement can be done on the modeling program we used in this research. The iMC code used to obtain the optical parameters from measured light signals in this study is a modification of an existing code developed in our research group. Although in current form it is still a robust program in numerically solving the RT, it can further be improved by optimizing the inverse algorithm portion of the code. For the cell samples study, the optical parameters were obtained by performing non optimized manual fitting which was time consuming and could not obtain the minimized $\delta$ values for some wavelengths. This could be one of the reasons why $\delta$ values for some wavelengths across

the samples measured were not able to converge to under 3% as shown in Figs. 5-16, 5-17 and 5-18.

The experimental system used in this research as shown in Figs. 4-1 and 4-3 could also be modified to improve scattered light signal detection. This can be achieved by optimizing the placement of the three photodetectors around the sample to prevent one signal from dominating the objective function δ which makes data fitting and inverse calculations difficult. One challenge we faced in the measurement of optical parameters for both microsphere and cell samples is the time-based settling down of the suspensions within a sample which according to our studies significantly affect the measured light signals as shown in Figs. 4-15 and 5-13. The current experimental design involves manually tuning the wavelength for each measurement and also shaking the sample at each wavelength. Constantly moving the sample from the sample stage during measurements can add errors due to possible sample position placement variations. To address this issue in future studies, we recommend modifying the spectrophotometric system to enable automatic light signal measurements which involves less alignment and manual intervention. By tuning the wavelengths and acquiring the light signal automatically, experimental errors can be significantly reduced while shortening the time needed to acquire the light signals hence reducing the suspension settling down effect.

Finally, additional studies might be needed to explore alternative reagents used in the cell preparations and treatment. For instance, the average mass density of MCF7 cells is ~1.11g/mL while that of the DMEM culture media used to prepare the suspension sample is ~1.01 g/mL [95]. Research needs to be done on if the density of the DMEM can be slightly modified to match that of the MCF7 cells. This will significantly reduce the settling speed of cell suspension samples. Previous studies have shown that the density of the cell culture media can be altered by modifying

the composition of the supplement solutes used in the media such as FBS [96]. Another reagent which might need to studied is the apoptosis inducing drug. As earlier reported, the excitation and emission spectra of the doxorubicin drug partially overlaps that of the PI staining dye used in FCM measurements. In addition, the drug absorption range falls within the spectral range of the spectrophotometric measurements of this dissertation research thus interfering with $\mu_a$ comparison studies among cell samples treated with different dose. We thus recommend looking into the possibility of replacing the choice of drug in future studies. Other anticancer drugs such as Docetaxel and Aripiprazole have been reported to have similar effect as doxorubicin drug in inducing apoptosis on MCF7 cells [97]. However, these drugs have their characteristic absorption in the ultraviolet range ~250 nm which is outside the spectral range used in this dissertation research of 460-1000 nm and thus a better alternative.

# References


[1] P. Tian, Y. Qin, S. M. Mutisya, J. Q. Lu, and X. H. Hu, "Multiparameter Spectrophotometry Platform for Turbid Sample Measurement by Robust Solutions of Radiative Transfer Problems," *IEEE Transactions on Instrumentation and Measurement,* vol. 70, pp. 1-10, 2021, doi: 10.1109/TIM.2020.3032184.

[2] J. Bleloch. "Clonogenic assay: what, why and how." CytoSMART. (accessed 01/18/21).

[3] *Thawing, Propagating and Cryopreserving of NCI-PBCF-HTB22 (MCF7)*. Manassas, VA: ATCC, 2012.

[4] M. Szymanek, G. Chodorowska, A. Pietrzak, and D. Krasowska, "Apoptosis of T Lymphocytes in Systemic Sclerosis," 2012, doi: 10.5772/28493.

[5] P. Tian, S. M. Mutisya, J. Jin, S. Zheng, J. Q. Lu, and X.-H. Hu, "Spectral determination of μa, μs and g from single and multiple scattering signals with one optically thick sample," *Journal of Quantitative Spectroscopy and Radiative Transfer,* vol. 245, p. 106868, 2020/04/01/ 2020.

[6] C. S. Mulvey, K. Zhang, W.-H. B. Liu, D. J. Waxman, and I. J. Bigio, "Wavelength-dependent backscattering measurements for quantitative monitoring of apoptosis, part 1: early and late spectral changes are indicative of the presence of apoptosis in cell cultures," (in eng), *Journal of biomedical optics,* vol. 16, no. 11, pp. 117001-117001, 2011, doi: 10.1117/1.3644389.

[7] S. L. Jacques, "Optical properties of biological tissues: a review," *Physics in medicine and biology,* vol. 58, no. 11, pp. R37-R61, 2013, doi: 10.1088/0031-9155/58/11/R37.

[8] J. Qin and R. Lu, "Hyperspectral diffuse reflectance imaging for rapid, noncontact measurement of the optical properties of turbid materials," *Appl. Opt.,* vol. 45, no. 32, p. 8366, 2006.

[9] H. C. v. d. Hulst, *Multiple light scattering: tables, formulas, and applications* (no. Book, Whole). New York: Academic Press, 1980.

[10] X. Liang *et al.*, "Spectrophotometric determination of turbid optical parameters without using an integrating sphere," *Appl. Opt.*, vol. 55, no. 8, p. 2079, 2016.

[11] R. Michels, F. Foschum, and A. Kienle, "Optical properties of fat emulsions," *Optics express,* vol. 16, no. 8, p. 5907, 2008, doi: 10.1364/OE.16.005907.

[12] V. G. Peters, D. R. Wyman, M. S. Patterson, and G. L. Frank, "Optical properties of normal and diseased human breast tissues in the visible and near infrared," *Physics in Medicine and Biology*, vol. 35, no. 9, pp. 1317-1334, 1990, doi: 10.1088/0031-9155/35/9/010.

[13] I. V. Yaroslavsky, A. N. Yaroslavsky, T. Goldbach, and H. J. Schwarzmaier, "Inverse hybrid technique for determining the optical properties of turbid media from integrating-sphere measurements," *Appl. Opt.,* vol. 35, no. 34, p. 6797, 1996, doi: 10.1364/AO.35.006797.

[14] D. Zhu, W. Lu, S. Zeng, and Q. Luo, "Effect of light losses of sample between two integrating spheres on optical properties estimation," *Journal of Biomedical Optics,* vol. 12, no. 6, pp. 064004-064008, 2007, doi: 10.1117/1.2815691.

[15] X. Liang *et al.*, "Spectrophotometric determination of turbid optical parameters without using an integrating sphere," *Appl. Opt.*, vol. 55, no. 8, pp. 2079-2085, 2016/03/10 2016, doi: 10.1364/AO.55.002079.

[16] M. Archana, B. , T. Yogesh, and K. Kumaraswamy, "Various methods available for detection of apoptotic cells- A review," *Indian Journal of Cancer*, Review Article vol. 50, no. 3, pp. 274-283, July 1, 2013 2013, doi: 10.4103/0019-509x.118720.

[17] P. Latimer, "Light Scattering and Absorption as Methods of Studying Cell Population Parameters," *Annual Review of Biophysics and Bioengineering*, vol. 11, no. 1, pp. 129-150, 1982, doi: 10.1146/annurev.bb.11.060182.001021.

[18] R. Drezek, A. Dunn, and R. Richards-Kortum, "Light scattering from cells: finite-difference time-domain simulations and goniometric measurements," *Appl. Opt.*, vol. 38, no. 16, p. 3651, 1999, doi: 10.1364/AO.38.003651.

[19] C. Chen, J. Q. Lu, H. Ding, K. M. Jacobs, Y. Du, and X.-H. Hu, "A primary method for determination of optical parameters of turbid samples and application to intralipid between 550 and 1630nm," *Optics Express*, vol. 14, no. 16, p. 7420, 2006, doi: 10.1364/OE.14.007420.

[20] M. A. N. Keppy, "Understanding Spectral Bandwidth and Resolution in the Regulated Laboratory."

[21] Y. Cheng, B. Xie, Y. Ma, W. Shu, and X. Luo, "Silica doped quantum dots film with enhanced light conversion efficiency for white light emitting diodes," 2017: IEEE, pp. 394-397, doi: 10.1109/ICEPT.2017.8046479.

[22] Y. Du, X. H. Hu, M. Cariveau, X. Ma, G. W. Kalmus, and J. Q. Lu, "Optical properties of porcine skin dermis between 900 nm and 1500 nm," *Physics in Medicine and Biology*, vol. 46, no. 1, pp. 167-181, 2001, doi: 10.1088/0031-9155/46/1/312.

[23] J. F. Beek *et al.*, "In vitro double-integrating-sphere optical properties of tissues between 630 and 1064 nm," *Physics in Medicine and Biology*, vol. 42, no. 11, pp. 2255-2261, 1997, doi: 10.1088/0031-9155/42/11/017.

[24] J. W. Pickering, S. A. Prahl, N. van Wieringen, J. F. Beek, H. J. C. M. Sterenborg, and M. J. C. van Gemert, "Double-integrating-sphere system for measuring the optical properties of tissue," *Appl. Opt.*, vol. 32, no. 4, pp. 399-410, 1993/02/01 1993, doi: 10.1364/AO.32.000399.

[25] H. J. van Staveren, C. J. M. Moes, J. van Marie, S. A. Prahl, and M. J. C. van Gemert, "Light scattering in lntralipid-10% in the wavelength range of 400–1100 nm," *Appl. Opt.*, vol. 30, no. 31, pp. 4507-4514, 1991/11/01 1991, doi: 10.1364/AO.30.004507.

[26] X. Chen *et al.*, "Fast method for inverse determination of optical parameters from two measured signals," *Optics letters*, vol. 38, no. 12, p. 2095, 2013, doi: 10.1364/OL.38.002095.

[27] G. E. Davis, "Scattering of Light by an Air Bubble in Water," *Journal of the Optical Society of America*, vol. 45, no. 7, p. 572, 1955, doi: 10.1364/JOSA.45.000572.

[28] H. D. Soule, J. Vazguez, A. Long, S. Albert, and M. Brennan, "A human cell line from a pleural effusion derived from a breast carcinoma," (in eng), *J Natl Cancer Inst*, vol. 51, no. 5, pp. 1409-16, Nov 1973.

[29] K. B. Horwitz, M. E. Costlow, and W. L. McGuire, "MCF7; a human breast cancer cell line with estrogen, androgen, progesterone, and glucocorticoid receptors," (in eng), *Steroids*, vol. 26, no. 6, pp. 785-95, Dec 1975.

[30] M. Harris, "Cells and Tissues in Culture. Methods, Biology and Physiology. Volume 3. E. N. Willmer," *The Quarterly Review of Biology*, vol. 42, no. 4, pp. 540-540, 1967, doi: 10.1086/405539.

[31] S. Elmore, "Apoptosis: A Review of Programmed Cell Death," vol. 35, ed. United States: SAGE Publications, 2007, pp. 495-516.
[32] B. Alberts, *Molecular biology of the cell*, Sixth ed. (no. Book, Whole). New York, NY: Garland Science, Taylor and Francis Group, 2015.
[33] A. Saraste and K. Pulkki, "Morphologic and biochemical hallmarks of apoptosis," *Cardiovascular research,* vol. 45, no. 3, pp. 528-537, 2000, doi: 10.1016/S0008-6363(99)00384-3.
[34] R. Lüpertz, W. Wätjen, R. Kahl, and Y. Chovolou, "Dose- and time-dependent effects of doxorubicin on cytotoxicity, cell cycle and apoptotic cell death in human colon cancer cells," *Toxicology,* vol. 271, no. 3, pp. 115-121, 2010, doi: 10.1016/j.tox.2010.03.012.
[35] G. Banfalvi, "Methods to detect apoptotic cell death," *Apoptosis,* vol. 22, no. 2, pp. 306-323, 2017/02/01 2017, doi: 10.1007/s10495-016-1333-3.
[36] J. E. Till and E. A. McCulloch, "A direct measurement of the radiation sensitivity of normal mouse bone marrow cells. 1961," (in eng), *Radiat Res,* vol. 178, no. 2, pp. Av3-7, Aug 2012, doi: 10.1667/rrav01.1.
[37] J. M. Brown and L. D. Attardi, "The role of apoptosis in cancer development and treatment response," (in eng), *Nat Rev Cancer,* vol. 5, no. 3, pp. 231-7, Mar 2005, doi: 10.1038/nrc1560.
[38] N. A. P. Franken, H. M. Rodermond, J. Stap, J. Haveman, and C. van Bree, "Clonogenic assay of cells in vitro," *Nature Protocols,* vol. 1, no. 5, pp. 2315-2319, 2006/12/01 2006, doi: 10.1038/nprot.2006.339.
[39] H. Rafehi, C. Orlowski, G. T. Georgiadis, K. Ververis, A. El-Osta, and T. C. Karagiannis, "Clonogenic assay: adherent cells," (in eng), *Journal of visualized experiments : JoVE,* no. 49, p. 2573, 2011, doi: 10.3791/2573.
[40] T. Yonei *et al.*, "Antitumor activity of platinum analogs against human lung cancer cell lines and tumor specimens," (in eng), *Acta Med Okayama,* vol. 47, no. 4, pp. 233-41, Aug 1993, doi: 10.18926/amo/31552.
[41] T. L. Riss *et al.*, "Cell Viability Assays," in *Assay Guidance Manual*, G. S. Sittampalam *et al.* Eds. Bethesda (MD): Eli Lilly & Company and the National Center for Advancing Translational Sciences, 2004.
[42] J. van Meerloo, G. J. Kaspers, and J. Cloos, "Cell sensitivity assays: the MTT assay," (in eng), *Methods Mol Biol,* vol. 731, pp. 237-45, 2011, doi: 10.1007/978-1-61779-080-5_20.
[43] Y. Kanemura *et al.*, "Evaluation of in vitro proliferative activity of human fetal neural stem/progenitor cells using indirect measurements of viable cells based on cellular metabolic activity," *Journal of neuroscience research,* vol. 69, no. 6, pp. 869-879, 2002, doi: 10.1002/jnr.10377.
[44] J. A. Plumb, R. Milroy, and S. B. Kaye, "Effects of the pH dependence of 3-(4,5-dimethylthiazol-2-yl)-2,5-diphenyl-tetrazolium bromide-formazan absorption on chemosensitivity determined by a novel tetrazolium-based assay," *Cancer research,* vol. 49, no. 16, p. 4435, 1989.
[45] H. Lecoeur, M. Février, S. Garcia, Y. Rivière, and M. L. Gougeon, "A novel flow cytometric assay for quantitation and multiparametric characterization of cell-mediated cytotoxicity," (in eng), *J Immunol Methods,* vol. 253, no. 1-2, pp. 177-87, Jul 1 2001, doi: 10.1016/s0022-1759(01)00359-3.

[46] D. Wlodkowic, J. Skommer, and Z. Darzynkiewicz, "Flow cytometry-based apoptosis detection," (in eng), *Methods Mol Biol,* vol. 559, pp. 19-32, 2009, doi: 10.1007/978-1-60327-017-5_2.

[47] P. Nánási, Jr. *et al.*, "Doxorubicin induces large-scale and differential H2A and H2B redistribution in live cells," (in eng), *PLoS One,* vol. 15, no. 4, p. e0231223, 2020, doi: 10.1371/journal.pone.0231223.

[48] I. Itzkan *et al.*, "Confocal light absorption and scattering spectroscopic microscopy monitors organelles in live cells with no exogenous labels," *Proceedings of the National Academy of Sciences,* vol. 104, no. 44, pp. 17255-17260, 2007, doi: 10.1073/pnas.0708669104.

[49] N. N. Boustany, S. C. Kuo, and N. V. Thakor, "Optical scatter imaging: subcellular morphometry in situ with Fourier filtering," *Optics Letters,* vol. 26, no. 14, pp. 1063-1065, 2001/07/15 2001, doi: 10.1364/OL.26.001063.

[50] K. J. Chalut, J. H. Ostrander, M. G. Giacomelli, and A. Wax, "Light scattering measurements of subcellular structure provide noninvasive early detection of chemotherapy-induced apoptosis," (in eng), *Cancer Res,* vol. 69, no. 3, pp. 1199-204, Feb 1 2009, doi: 10.1158/0008-5472.Can-08-3079.

[51] C. S. Mulvey, A. Curtis, S. Singh, and I. Bigio, "Elastic Scattering Spectroscopy as a Diagnostic Tool for Apoptosis in Cell Cultures," *IEEE Journal of Selected Topics in Quantum Electronics,* vol. 13, pp. 1663-1670, 2007.

[52] J. A. Izatt *et al.*, "MICRON~RESOLUTION BIOMEDICAL IMAGING WITH OPTICAL COHERENCE TOMOGRAPHY," *Optics and Photonics News,* vol. 4, no. 10, pp. 14-19, 1993/10/01 1993, doi: 10.1364/OPN.4.10.000014.

[53] M. Rajadhyaksha, M. Grossman, D. Esterowitz, R. H. Webb, and R. R. Anderson, "In vivo confocal scanning laser microscopy of human skin: melanin provides strong contrast," (in eng), *J Invest Dermatol,* vol. 104, no. 6, pp. 946-52, Jun 1995, doi: 10.1111/1523-1747.ep12606215.

[54] V. Turzhitsky *et al.*, "Spectroscopy of scattered light for the characterization of micro and nanoscale objects in biology and medicine," (in eng), *Appl Spectrosc,* vol. 68, no. 2, pp. 133-54, 2014, doi: 10.1366/13-07395.

[55] C. S. Mulvey, C. A. Sherwood, and I. J. Bigio, "Wavelength-dependent backscattering measurements for quantitative real-time monitoring of apoptosis in living cells," (in eng), *J Biomed Opt,* vol. 14, no. 6, p. 064013, Nov-Dec 2009, doi: 10.1117/1.3259363.

[56] I. Georgakoudi, W. L. Rice, M. Hronik-Tupaj, and D. L. Kaplan, "Optical spectroscopy and imaging for the noninvasive evaluation of engineered tissues," (in eng), *Tissue Eng Part B Rev,* vol. 14, no. 4, pp. 321-40, Dec 2008, doi: 10.1089/ten.teb.2008.0248.

[57] M. M. Martinez, R. D. Reif, and D. Pappas, "Detection of apoptosis: A review of conventional and novel techniques," *Analytical methods,* Article vol. 2010 v.2 no.8, no. no. 8, pp. 996-1004, 2010-07-03 2010, doi: 10.1039/c0ay00247j.

[58] J. R. Mourant *et al.*, "Light scattering from cells: the contribution of the nucleus and the effects of proliferative status," (in eng), *J Biomed Opt,* vol. 5, no. 2, pp. 131-7, Apr 2000, doi: 10.1117/1.429979.

[59] M. F. Modest, *Radiative heat transfer,* Third;Third; ed. (no. Book, Whole). New York: Academic Press, 2013.

[60] D. Hahn, "Light Scattering Theory," ed. Department of Mechanical and Aerospace Engineering, University of Florida, 2004.

[61] C. F. Bohren and D. R. Huffman, *Absorption and scattering of light by small particles* (no. Book, Whole). New York: Wiley, 1983.
[62] Acharya and Rajat, *Satellite Signal Propagation, Impairments and Mitigation* (no. Book, Whole). GB: Academic Press, 2017.
[63] A. J. Cox, A. J. DeWeerd, and J. Linden, "An experiment to measure Mie and Rayleigh total scattering cross sections," *American Journal of Physics,* vol. 70, no. 6, pp. 620-625, 2002, doi: 10.1119/1.1466815.
[64] R. Acharya, "Chapter 3 - Interaction of waves with medium," in *Satellite Signal Propagation, Impairments and Mitigation*, R. Acharya Ed.: Academic Press, 2017, pp. 57-86.
[65] J. E. Hansen and L. D. Travis, "Light scattering in planetary atmospheres," *Space Science Reviews,* vol. 16, no. 4, pp. 527-610, 1974, doi: 10.1007/BF00168069.
[66] S. Chandrasekhar, *Radiative transfer* (no. Book, Whole). New York: Dover Publications, 1960.
[67] L. G. a. G. Henyey, J.L. , "Diffuse Radiation in the Galaxy," *Astrophysical,* vol. 93, pp. 70-83, 1941.
[68] A. P. Gibson, J. C. Hebden, and S. R. Arridge, "Recent advances in diffuse optical imaging," *Physics in Medicine and Biology,* vol. 50, no. 4, pp. R1-R43, 2005, doi: 10.1088/0031-9155/50/4/R01.
[69] A. H. Hielscher, R. E. Alcouffe, and R. L. Barbour, "Comparison of finite-difference transport and diffusion calculations for photon migration in homogeneous and heterogeneous tissues," (in eng), *Phys Med Biol,* vol. 43, no. 5, pp. 1285-302, May 1998, doi: 10.1088/0031-9155/43/5/017.
[70] S. A. Prahl, M. J. C. van Gemert, and A. J. Welch, "Determining the optical properties of turbid media by using the adding–doubling method," *Appl. Opt.,* vol. 32, no. 4, pp. 559-568, 1993/02/01 1993, doi: 10.1364/AO.32.000559.
[71] C. Sandoval and A. D. Kim, "Deriving Kubelka–Munk theory from radiative transport," *J. Opt. Soc. Am. A,* vol. 31, no. 3, pp. 628-636, 2014/03/01 2014, doi: 10.1364/JOSAA.31.000628.
[72] A. D. Klose, U. Netz, J. Beuthan, and A. H. Hielscher, "Optical tomography using the time-independent equation of radiative transfer — Part 1: forward model," *Journal of Quantitative Spectroscopy and Radiative Transfer,* vol. 72, no. 5, pp. 691-713, 2002, doi: 10.1016/S0022-4073(01)00150-9.
[73] U. M. Noebauer and S. A. Sim, "Monte Carlo radiative transfer," *Living Reviews in Computational Astrophysics,* vol. 5, no. 1, p. 1, 2019/06/11 2019, doi: 10.1007/s41115-019-0004-9.
[74] R. C. Haskell, L. O. Svaasand, T. T. Tsay, T. C. Feng, M. S. McAdams, and B. J. Tromberg, "Boundary conditions for the diffusion equation in radiative transfer," *Journal of the Optical Society of America. A, Optics, image science, and vision,* vol. 11, no. 10, p. 2727, 1994, doi: 10.1364/JOSAA.11.002727.
[75] L. Wang, S. L. Jacques, and L. Zheng, "MCML--Monte Carlo modeling of light transport in multi-layered tissues," (in eng), *Comput Methods Programs Biomed,* vol. 47, no. 2, pp. 131-46, Jul 1995.
[76] Z. Song, K. Dong, X. H. Hu, and J. Q. Lu, "Monte Carlo simulation of converging laser beams propagating in biological materials," *Applied Optics,* vol. 38, no. 13, pp. 2944-2949, 1999/05/01 1999, doi: 10.1364/AO.38.002944.

[77] P. Tian, C. Chen, J. Jin, H. Hong, J. Q. Lu, and X.-H. Hu, "Quantitative characterization of turbidity by radiative transfer based reflectance imaging," *Biomedical Optics Express,* vol. 9, no. 5, pp. 2081-2094, 2018/05/01 2018, doi: 10.1364/BOE.9.002081.

[78] J. Hill and S. S. Sawilowsky, "Bias in Monte Carlo simulations due to pseudo-random number generator initial seed selection," *Journal of Modern Applied Statistical Methods,* vol. 10, pp. 29-50, 2011.

[79] Y. Wen *et al.*, "Quantitative analysis and comparison of 3D morphology between viable and apoptotic MCF7 breast cancer cells and characterization of nuclear fragmentation," (in eng), *PLoS One,* vol. 12, no. 9, p. e0184726, 2017, doi: 10.1371/journal.pone.0184726.

[80] H. S. Moon *et al.*, "Continual collection and re-separation of circulating tumor cells from blood using multi-stage multi-orifice flow fractionation," (in eng), *Biomicrofluidics,* vol. 7, no. 1, p. 14105, 2013, doi: 10.1063/1.4788914.

[81] F. J. López-Hernández, "Cell Surface Area to Volume Relationship During Apoptosis and Apoptotic Body Formation," (in eng), *Cell Physiol Biochem,* vol. 55, no. S1, pp. 161-170, May 8 2021, doi: 10.33594/000000369.

[82] A. M. Pinaire, "Morphology Analysis and Diffraction Imaging Study of Apoptosis in MCF7 Cells," Doctoral Dissertation (in preparation), East Carolina University.

[83] O. C. Marina, C. K. Sanders, and J. R. Mourant, "Correlating light scattering with internal cellular structures," *Biomedical optics express,* vol. 3, no. 2, p. 296, 2012, doi: 10.1364/BOE.3.000296.

[84] S. R. Systems. *User's Manual for DSP Lock-In Amplifier, SR830*, Sunnyvale, California, 1993.

[85] W. Budde, "Stability of High-Pressure Xenon Lamps," *Journal of the Optical Society of America,* vol. 52, no. 3, p. 343, 1962, doi: 10.1364/JOSA.52.000343.

[86] X. Ma, J. Q. Lu, R. S. Brock, K. M. Jacobs, P. Yang, and X.-H. Hu, "Determination of complex refractive index of polystyrene microspheres from 370 to 1610 nm," *Physics in Medicine and Biology,* vol. 48, no. 24, pp. 4165-4172, 2003, doi: 10.1088/0031-9155/48/24/013.

[87] A. Shahin, W. Bachir, and M. Sayem El-Daher, "Polystyrene Microsphere Optical Properties by Kubelka–Munk and Diffusion Approximation with a Single Integrating Sphere System: A Comparative Study," *Journal of Spectroscopy,* vol. 2019, p. 3406319, 2019/12/01 2019, doi: 10.1155/2019/3406319.

[88] Y. Qin *et al.*, "Robustness of inverse solutions for radiative transfer parameters from light signals measured with different detection configurations," *Journal of Quantitative Spectroscopy and Radiative Transfer,* vol. 274, p. 107883, 2021/11/01/ 2021.

[89] ATCC, *MCF7* (User Manual). Manassas, VA, USA.

[90] K. S. Louis and A. C. Siegel, "Cell viability analysis using trypan blue: manual and automated methods," (in eng), *Methods Mol Biol,* vol. 740, pp. 7-12, 2011, doi: 10.1007/978-1-61779-108-6_2.

[91] D. Wlodkowic, W. Telford, J. Skommer, and Z. Darzynkiewicz, "Apoptosis and beyond: cytometry in studies of programmed cell death," (in eng), *Methods Cell Biol,* vol. 103, pp. 55-98, 2011, doi: 10.1016/b978-0-12-385493-3.00004-8.

[92] E. A. Corbin, O. O. Adeniba, O. V. Cangellaris, W. P. King, and R. Bashir, "Evidence of differential mass change rates between human breast cancer cell lines in culture," (in eng), *Biomedical microdevices,* vol. 19, no. 1, p. 10, Mar 2017, doi: 10.1007/s10544-017-0151-x.

[93] G. Pizarro and E. Ríos, "How source content determines intracellular Ca2+ release kinetics. Simultaneous measurement of [Ca2+] transients and [H+] displacement in skeletal muscle," *The Journal of general physiology,* vol. 124, no. 3, pp. 239-258, 2004, doi: 10.1085/jgp.200409071.

[94] T. N. Nguyen *et al.*, "Optical Properties of Doxorubicin Hydrochloride Load and Release on Silica Nanoparticle Platform," *Molecules,* vol. 26, no. 13, p. 3968, 2021.

[95] A. Martín-Pérez *et al.*, "Hydrodynamic assisted multiparametric particle spectrometry," (in eng), *Sci Rep,* vol. 11, no. 1, p. 3535, Feb 11 2021, doi: 10.1038/s41598-021-82708-0.

[96] C. Poon, "Measuring the density and viscosity of culture media for optimized computational fluid dynamics analysis of in vitro devices," *bioRxiv,* p. 2020.08.25.266221, 2020, doi: 10.1101/2020.08.25.266221.

[97] M. TREBUNOVA, G. LAPUTKOVA, E. SLABA, K. LACJAKOVA, and A. VEREBOVA, "Effects of Docetaxel, Doxorubicin and Cyclophosphamide on Human Breast Cancer Cell Line MCF7," *Anticancer Research,* vol. 32, no. 7, pp. 2849-2854, 2012.

# Appendix A. Polysterene microsphere sample preparation

(1) 0.966 mm microspheres Nominal values (5095B, Duke Scientific Corporation)

W/V = weight of solute (g) in volume of solution (100mL=100$cm^3$)
W/V = 10% → solution mass-to-volume concentration=$\rho_m$=10g/100$cm^3$=0.1(g/$cm^3$)

Sphere diameter $d_s$=0.966 μm

Sphere mass density $\rho_s$=1.055 (g/$cm^3$) at 20° C.

Sphere volume $v_s$=4.720 x $10^{-13}$ $cm^3$

Sphere mass $m_s=\rho_s v_s$= 4.980 x $10^{-13}$ g

10% W/V microsphere solution:
nominal number concentration =$\rho_{n0}=\rho_m/m_s$=2.008x$10^{11}$ (spheres/$cm^3$)

(2) Steps to determine actual number concentration of sphere suspension $\rho_n$

(i) Nominal concentration of the original suspension is calculated from nominal W/V and spheres' volume, mass, and density. It is found to be 2.008x$10^{11}$ $cm^{-3}$.

(ii) Aliquot exactly 1.006 mL of the original suspension (2.008x$10^{11}$ $cm^{-3}$) and dilute it with 19. 497 mL of deionized water to obtain a 20 mL stock solution of nominal number concentration $\rho_{ns}$ =5.05 x $10^9$ $cm^{-3}$
Link to online calculator: https://www.sigmaaldrich.com/chemistry/stockroom-reagents/learning-center/technical-library/solution-dilution-calculator.html

(iii) 10 mL of the stock microsphere suspension ($v_t$) is weighed by an electronic balance with weighing accuracy of 0.1 mg

(iv) The water in the suspension is evaporated completely at a temperature of 60 ◦C to obtain dry microspheres and the mass is re-measured.
-Expected total spheres mass $m_{se}$ after evaporation can be estimated as:
$m_{se}=m_s\rho_{ns}v_t$=(4.980 x $10^{-13}$ g)( 5.05 x $10^9$$cm^{-3}$)(5 $cm^3$)=0.0252g or 25.2 mg

(v) The measured number concentration $\rho_{nm}$ of the polystyrene suspensions is calculated from the total mass of the microspheres $m_{st}$ (=0.061g per this measurement) , microspheres volume $v_s$, microspheres mass density $\rho_s$ and total suspensions volume before evaporation $v_t$ as ;

$\rho_{nm} = m_{st} / (\rho_s v_s v_t)$

$\rho_{nm} = 0.061g/(1.055\ g/cm^3 * 4.720 \times 10^{-13} cm^3 * 5 cm^3) = 2.450 \times 10^{10}\ cm^{-3}$

Make 1 dilution as follows.

(vi) To obtain a 3 mL solution of nominal number concentration $\rho_{ns} = 1.954 \times 10^9\ cm^{-3}$,

mix 2.761 mL of deionized water with 0.239 mL of $2.450 \times 10^{10}\ cm^{-3}$ suspension

# Appendix B. Doxorubicin drug preparation

Doxorubicin hydrochloride drug (Thermofisher, D1515).

Stock solution of the drug is prepared by dissolving a specific drug mass in a specific volume (V) of deionized water to make a stock solution with concentration (C) of 128 μM using the formula below.

$$Mass(g) = C(mol/L) \times V(L)$$

Formula Weight (g/mol) or the mass molarity calculator is provided by Sigma-Aldrich for faster and accurate calculations. Link https://www.sigmaaldrich.com/chemistry/stockroom-reagents/learning-center/technical-library/mass-molarity-calculator.html.

For instance, to make a 40 mL of 128 μM drug stock solution, measure ~2.97 mg of the drug powder with a 0.1 mg accuracy weighing scale and mix with 40 mL deionized water and mix thoroughly until the drug powder completely dissolves. Then split the stock solution into 4 conical tubes each 10 mL and freeze them. The drug solution is sensitive to light and thus the storage conical tubes should be wrapped with a dark paper. Previous studies have shown that the drug remains effective for several months if stored frozen at -20 $^0$C. Its thus advisable to split the stock solution into several smaller storage tubes to prevent thawing and freezing of the entire drug solution each time it is used. Stock solution drug preparation should be done in sterile environment to prevent contamination.

To treat cells with an appropriate drug dose, first establish the final volume ($V_f$) of the cell culture media the cells will be cultured in during the post treatment period. Then calculate the volume ($V_d$) of drug stock solution needed to be mixed with the volume ($V_m$)of cell culture media to obtain the desired final concentration ($C_f$) as

$$C_f V_f = C_d (V_m + V_d)$$

Solution dilution calculator provided by Sigma-Aldrich can be easily used to perform this calculation.https://www.sigmaaldrich.com/chemistry/stockroom-reagents/learning-center/technical-library/solution-dilution-calculator.html.

For instance, cells growing in a 6 mL media, add 2 mL of 128 μM stock solution to obtain a total volume of 8 mL for 32 μM drug concentration treatment.

# Appendix C. Cells maintenance and sample preparations

Part of this protocol is adapted from [3].

**1. Changing culture Media**

Required Materials

Complete growth medium (EMEM+10% FBS+0.01 mg/ml insulin), pre-warmed to $37^0$ C in water bath

Procedure

(i) Sterilize the laminar flow hood as required including the flask for putting the used media

(ii) Go through the checklist to ensure all required materials are placed in the flow hood.

(iii) Observe cells under microscope to check their growth and if they are adherent or suspended

(iv) In laminar hood, pipette the spent cell culture media to a waste media flask.

(v) Using a new pipette, add 6.0 to 8.0 mL of complete growth medium

(vi) Observe the cultured cells under microscope

(vii) Incubate cultures at 37°C.

**2. Subculturing cells**

Required Materials

a) Complete growth medium, pre-warmed to $37^0$ C in water bath.

b) Tissue-culture treated flasks, plates or dishes

c) Disposable, sterile 15-mL tubes

d) Dissociation reagent, 0.05% trypsin

Procedure

(i) Observe cells under microscope to check their growth and if they are adherent or suspended

(ii) Inside the laminar hood, pipette the spent cell culture media to a waste media flask.

(iii) Wash cells using a 2 mL Trypsin-EDTA solution. Gently add wash solution to the side of the vessel opposite the attached cell layer to avoid disturbing the cell layer, and rock the vessel back and forth several times.

(iv) Remove and discard the wash solution from the culture vessel

(v) Add the pre-warmed dissociation reagent Trypsin-EDTA solution to the side of

the flask; use enough reagent to cover the cell layer (0.5 mL and gently rock the container to get complete coverage of the cell layer)

(vi) Incubate the culture vessel at room temperature for approximately 1-2 minutes.

(vii) Observe the cells under the microscope for detachment. When ≥ 90% of the cells have detached, tilt the vessel for a minimal length of time to allow the cells to drain. Add the equivalent of 2 volumes (twice the volume used for the dissociation reagent) of pre-warmed complete growth medium. Disperse the medium by pipetting over the cell layer surface several times.

(viii) Transfer the cells to a 15-mL conical tube and centrifuge then at $150g$ $4^0C$ for 10 minutes

(ix) Drain the supernatant and re-suspend the cell pellet in a desired volume of pre-warmed complete growth medium.

(x) 50 µL of cell suspension taken out for counting using hemocytometer.

(xi) Dilute cell suspension to the density needed for each use (sub-culturing, sample preparation or seeding to plate wells)

**3 Counting cells using a hemocytometer**

Required Materials

a) Complete growth medium, pre-warmed to $37^0$ C in water bath, 1.5 ml microfuge tube (x2)

b) 0.05% Trypsin (dissociation reagent), pre-warmed to $37^0$ C

c) 0.4% trypan blue

Procedure

(i) Follow steps i-ix in #2 above

(ii) Mix well then take 0.5 ml of the cell suspension to 1.5 ml microfuge tube

(iii) Take 50 µL cell suspension from 1.5 ml to another microfuge tube, then add 50 µL of 0.4% trypan blue to the tube and mix it

(iv) Take 10 µL Trypan Blue-treated cell suspension and apply to the hemocytometer chamber.

(v) Using a microscope, focus on the grid lines of the hemocytometer with a 10X objective.

(vi) Using a hand tally counter, count the live, unstained cells (live cells do not take up Trypan Blue) in one set of square and repeat for 3 more squares. When counting, employ a system whereby cells are only counted when they are set within a square or on the right-hand or bottom boundary line.

**4. MTT Cell Proliferation Assay**

Reagent Preparation

Prepare a 12 mM MTT stock solution by adding 1 mL of sterile PBS to one 5 mg vial of MTT. Mix by vortexing or sonication until dissolved. Occasionally there may be some particulate material that will not dissolve; this can be removed by filtration or centrifugation. Each 5 mg vial of MTT provides sufficient reagent for 100 tests, using 10 µL of the stock solution per well. Once prepared, the MTT solution can be stored for four weeks at 4°C protected from light.

Steps

(i) Dilute the suspended cells to be assayed (in concentrations higher than $5x10^4$ cells/ml) by MTT to 5,000-50,000 cells/ml and plate 100 µL per well (96-well plate) and incubate for 24 hours for the cells to attach. Make sure the cells are seeded on the plate wells in triplicates.

(ii) Remove the medium by pipet (set to 90 µl and leave some medium in to protect cells) and replace it with 100 µL of fresh culture medium.

(iii) Add 10 µL of the 12 µM MTT stock solution to each well. Include a negative control of 10 µL of the MTT stock solution added to 100 µL of medium alone.

(iv) Incubate at 37°C in a humidified chamber for 4 hours for cells' oxidoreductase enzyme to reduce the yellow MTT solution to a purple formazan pellets.

(v) The microtiter plate is centrifuged at 200g and 10 mins to spin down the pellets. The supernatant is removed.

(vi) Add 100 µL of isopropanol solution (solubilization reagent) to each well and mix thoroughly using the pipette to get a purple color solution

(vii) Read absorbance at 540 nm.

Equation for calculating survival ratio from OD.

Survival ratio = (OD reading – blank well OD)/(OD reading of untreated wells – blank well OD)

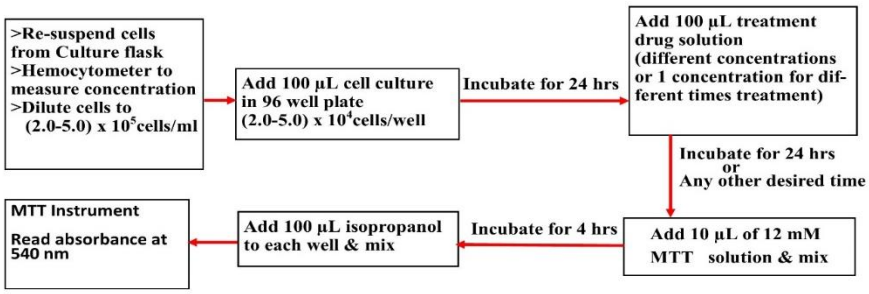

**5. Spectrophotometric samples cell treatment: Same post-treatment time and different drug dose**

(i) The protocol described below ensures that each spectrophotometric sample have the same solid mass (mixture of viable, apoptotic and debris cells). The % of each cell type in each sample will depend on drug dose. Hemocytometer will be used to approximate the concentration of each cell type in a turbid sample (see protocol below).

(ii) Hemocytometer will be used to approximate the concentration of each cell type in a turbid

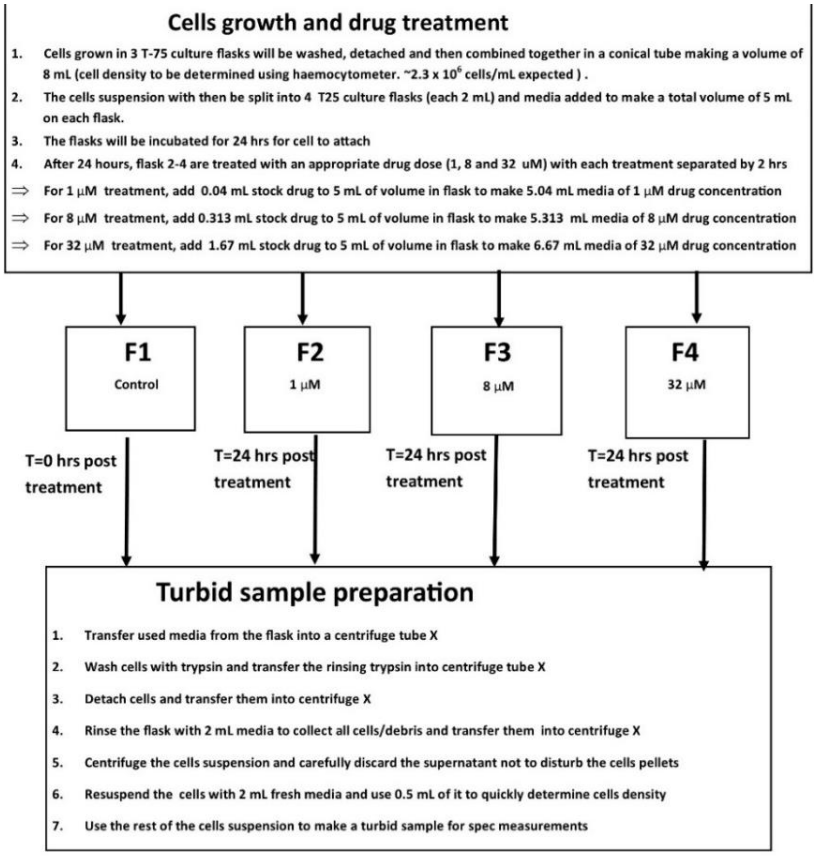

**6. Spectrophotometric samples cell treatment: Same drug dose and different post-treatment time**

(i) The protocol described below ensures that each spectrophotometric sample have the same solid mass (mixture of viable, apoptotic and debris cells). The % of each cell type in each sample will depend on post treatment times.

(ii) Hemocytometer will be used to approximate the concentration of each cell type in a turbid sample (see protocol below)

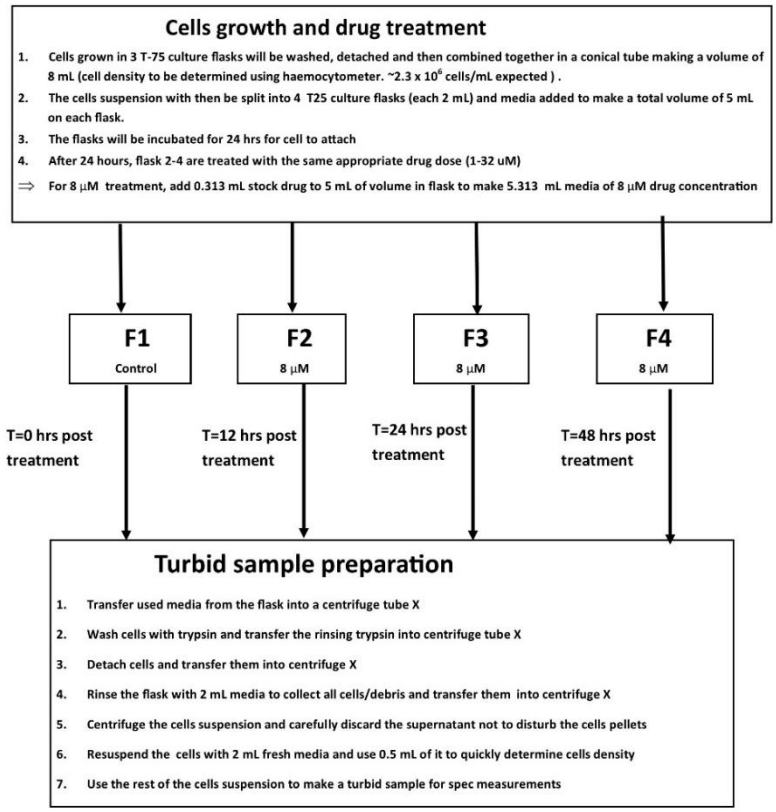

**7. Measurement time consideration for different assays**

MTT assay

24 hr for reattach=>30 mins drug treatment=>24 hr (variable) post treatment=> 30 mins MTT chemical treatment=>4 hr incubation=> 30 mins isopropanol treatment & absorbance readings (total minimum time =53.5 hrs)

FCM assay

24 hr for reattach=>30 mins drug treatment=>24 hr (variable) post treatment=> 30 mins cell staining with fluorophores=>30 mins incubation=> 30 to prepare FCM samples and acquire signals (total minimum time =50 hrs)

Spectroscopy measurement

24 hr for reattach=>30 mins drug treatment=>24 hr (variable) post treatment=> 30 min turbid sample preparation=>30 Spectroscopy measurement (total minimum time=49.5 hrs).

**8. Aseptic technique for preventing cell culture contamination**

According to suggestions given by Thermofisher scientific, the simplest and most economical way to reduce contamination from airborne particles and aerosols like dust, spores, shed skin, sneezing is to use a cell culture hood while ensuring the following:

(i) The work surface should be uncluttered and contain only items required for a particular procedure; it should not be used as a storage area.

(ii) Before and after use, the work surface should be disinfected thoroughly, and the surrounding areas and equipment should be cleaned routinely.

(iii) For routine cleaning, wipe the work surface with 70% ethanol before and during work, especially after any spillage.

(iv) Use ultraviolet light to sterilize the air and exposed work surfaces in the cell culture hood between uses.

(v) Leave the cell culture hood running at all times, turning it off only when they will not be used for extended periods of time.

In addition, sterile handling of cell culture components is the second aspect which ensures all possible contaminants are eliminated and they include.

(i) Always wipe hands and your work area with 70% ethanol.

(ii) Wipe the outside of the containers, flasks, plates, and dishes with 70% ethanol before placing them in the cell culture hood.

(iii) Avoid pouring media and reagents directly from bottles or flasks.

(iv) Use sterile glass or disposable plastic pipettes and a pipettor to work with liquids and use each pipette only once to avoid cross contamination. Do not unwrap sterile pipettes until they are to be used.

(v) Always cap the bottles and flasks after use and seal multi-well plates with tape or place them in resealable bags to prevent microorganisms and airborn contaminants from gaining entry.

(vi) Never uncover a sterile flask, bottle, petri dish, etc. until the instant you are ready to use it and never leave it open to the environment. Return the cover as soon as you are finished.

(vii) If you remove a cap or cover, and have to put it down on the work surface, place the cap with opening facing down.

(viii) Use only sterile glassware and other equipment.